9-1-2016 12:00 AM

Dicke's Superradiance in Astrophysics

Fereshteh Rajabi
The University of Western Ontario

Supervisor
Prof. Martin Houde
The University of Western Ontario

Graduate Program in Physics
A thesis submitted in partial fulfillment of the requirements for the degree in Doctor of Philosophy

Abstract

It is generally assumed that in the interstellar medium much of the emission emanating from atomic and molecular transitions within a radiating gas happen independently for each atom or molecule, but as was pointed out by R. H. Dicke in a seminal paper several decades ago this assumption does not apply in all conditions. As will be discussed in this thesis, and following Dicke's original analysis, closely packed atoms/molecules can interact with their common electromagnetic field and radiate coherently through an effect he named superradiance. Superradiance is a cooperative quantum mechanical phenomenon characterized by high intensity, spatially compact, burst-like features taking place over a wide range of timescales, depending on the size and physical conditions present in the regions harbouring such sources of radiation. I will discuss the potential for superradiance in the atomic hydrogen 21-cm line for which we extended Dicke's analysis to the magnetic dipole interaction characterizing this line. Then, the application of superradiance to the OH 1612-MHz, CH_3OH 6.7-GHz and H_2O 22-GHz maser lines will be discussed, and it will be shown that superradiance provides a valid explanation for previous observations of intensity flares detected in these spectral lines for some astronomical sources. An interesting result is that superradiance provides a natural mechanism for the recent observations of periodic and seemingly "alternating" methanol and water flares in G107.298+5.639 that cannot be easily explained within the context of maser theory.

Keywords: Atomic/Molecular Processes, Interstellar Medium, Coherent Interactions, Superradiance, Maser

Co-Authorship

This thesis is comprised of three papers among which two are already accepted for publication in The Astrophysical Journal, and one is submitted to Science Advances and still undergoing the review process. All three papers were co-authored with Dr. Martin Houde who has supervised the three projects.

The work described in Chapter 2 is concerned with the first ever published paper on superradiance within the context of astrophysics, and provides a thorough theoretical and numerical investigation of superradiance for magnetic dipolar transitions (i.e., for the hydrogen 21 cm line). The analyses in Section 2.3.1 describing the interaction of two atoms separated by small and large interatomic distances, were conducted with Dr. Houde. Similarly, parts of the Introduction and Discussion were also written with Dr. Houde.

In Chapter 3 we extend the scope of our work by comparing the existing superradiance theoretical model for electric dipolar transitions to data of the OH 1612-MHz line obtained for the U Orionis Mira star and the IRAS 18276-1431 pre-planetary nebula. Our numerical analysis closely follows the formalism of superradiance presented in Gross and Haroche [1982]. The data for U Orionis were taken from Jewell et al. [1981] while the data for the IRAS 18276-1431 pre-planetary nebula were kindly made available to us by Wolak et al. [2014]. Both data sets were analyzed by myself, while the discussion of the results presented in Sections 3.4.1 to 3.4.3 was written with Dr. Houde.

In Chapter 4 the superradiance model discussed in Chapter 3 was augmented and further used to explain the existence of intensity flares detected in the G33.64-0.21, Cep A, and G107.298+5.639 star-forming regions. The data for G33.64-0.21 were first published by Fujisawa et al. [2014] and made available to us by the (first) author. The Cep A data were taken from Mattila et al. [1985], while Szymczak et al. [2016] conducted the observations for G107.298+5.639 and kindly shared their data with us. All the analyses were mainly carried out by myself, while the discussion of the results for G107.298+5.639 was written with Dr. Houde.

Bibliography

K. Fujisawa, G. Takase, S. Kimura, N. Aoki, Y. Nagadomi, T. Shimomura, K. Sugiyama, K. Motogi, K. Niinuma, T. Hirota, and Y. Yonekura. Periodic flare of the 6.7-GHz methanol maser in IRAS 22198+6336. *Publications of the Astronomical Society of Japan*, 66:78, July 2014.

M. Gross and S. Haroche. Superradiance: An essay on the theory of collective spontaneous emission. *Physics Reports*, 93:301–396, December 1982.

P. R. Jewell, J. C. Webber, and L. E. Snyder. Evolution of the OH maser emission from U Orionis. *The Astrophysical Journal*, 249:118–123, October 1981.

K. Mattila, N. Holsti, M. Toriseva, R. Anttila, and L. Malkamaki. Rapid outbursts in the water maser Cepheus A. *Astronomy & Astrophysics*, 145:192–200, April 1985.

M. Szymczak, M. Olech, P. Wolak, A. Bartkiewicz, and M. Gawroński. Discovery of periodic and alternating flares of the methanol and water masers in G107.298+5.639. *Monthly Notices of the Royal Astronomical Society*, 459:L56–L60, June 2016.

P. Wolak, M. Szymczak, A. Bartkiewicz, and E. Gerard. Violent maser events in the cirumstellar envelope of the pre-planetary nebula IRAS18276-1431. In *Proceedings of the 12th European VLBI Network Symposium and Users Meeting (EVN 2014). 7-10 October 2014. Cagliari, Italy*, page 116, 2014.

Acknowledgements

First of all, I would like to thank Dr. Martin Houde for his extraordinary mentorship and patience during my graduate studies. Over the last few years, I have learned more physics from him than any other person in my life. He is definitely the most knowledgable, understanding and dedicated supervisor I had the fortune of working with. I would also like to thank Dr. Pauline Barmby and Dr. John de Bruyn for serving on my Advisory Committee during these years and sharing their experiences with me. That definitely kept me focused and reminded me of the importance of having carrier plans.

I should also thank Mitacs Globalink, Dr. Martin Houde, and Dr. Jean-Michel Raimond, from the Collège de France (Paris), for providing me with the opportunity to spend twelve weeks in the Laboratoire Kastler Brossel, in Paris, during the last year of my Ph.D. Although it is not reflected in my thesis, this internship allowed me to interact with world-renown researchers in the field of quantum optics and familiarized myself with the cutting-edge experimental techniques, which I hope to use in my future scientific adventures.

The last few years in the Department of Physics and Astronomy at Western were among the best years of my life. I could always reach out to Faculty and Staff members whenever I needed help and had their full support throughout my entire studies.

While being away from my home country was not always easy, I had the great support of my true friends, whom I am grateful to and will always remember. I would especially like to thank Ali, Maryam, Shannon, Sahar and Els for being so great and cheerful.

I am definitely indebted to my family, especially my mom, for believing in me and allowing me to have the most amazing dreams for my life. I could never be who I am without their support and would have stopped pursuing my dreams a long time ago, if it was not for their love.

Finally, I should thank my husband, Javad, for his true love and friendship. He always reminded me of my goals and showed me how persistent one should be through the long journey of learning.

Dedication

To my supervisor, Dr. Martin Houde, for his extraordinary mentorship.

List of Figures

Contents

Chapter 1

Introduction

The electromagnetic spectrum is a key tool to explore the Universe, and its precise interpretation is essential to getting an accurate picture and models of regions within, and distant from, our solar system. A vastly studied region that has drawn the attention of scientists practically from the beginning of astronomical research is the interstellar medium (ISM). The ISM, which consists of gas and dust over a wide range of densities distributed between the stars, emits radiation and interacts with the background radiation passing through it. The spectra of the ISM reveal information about the physical and chemical properties of its building blocks through their interactions with the ambient radiation. The intensity of the radiation measured directly from the obtained spectra, for example, is used to determine important parameters such as temperature and the density of particles [Emerson, 1996]. It should be noted that our prior knowledge and understanding of the physics of interactions between radiation and matter plays a crucial role in the interpretation of the spectra. It also directly impacts the accuracy with which we estimate fundamental physical and chemical quantities.

In studies of the ISM, it is generally assumed that each particle interacts independently with the ambient radiation field. This assumption, when applied to an ensemble of radiating particles, results in an intensity relation which is a linear function of the number of particles (for radiation that is optically thin). Based on this approach, the density of particles in the ISM is calculated and later used in further calculations, e.g., estimates of the strength of magnetic fields in the ISM.

In 1954, R. H. Dicke introduced a coherence theory, which describes a non-linear interaction and dependence between the intensity of the radiation and the number of particles [Dicke, 1954]. More precisely, he showed that the coherent interaction of particles via their radiation field can result in an enhancement of the radiation intensity, a phenomenon he named *superradiance*. In the 1970s and 80s, the theory was extensively studied and tested in different laboratories, and superradiance was observed in several cases [Skribanowitz et al., 1973, Vrehen et al., 1977, Cahuzac et al., 1979, Gounand et al., 1979, Gross et al., 1979, Rosenberger and DeTemple, 1981, Raimond et al., 1982, Kaluzny et al., 1983]. After the experimental confirmation of superradiance these coherent interactions were further studied in many different environments, but they were never investigated in the ISM.

The ISM is permeated with many different types of atoms and molecules which exist in a diverse range of physical conditions. It is possible that in some regions of the ISM, and under specific conditions, a given population of identical particles acts coherently and the intensity of the radiation emitted by those groups deviates from a simple linear relation. Therefore using this linear intensity relation in the analyses of spectra obtained from such regions could result in inaccurate estimates of physical quantities, and lead to an incorrect interpretation of those areas within the ISM.

In this thesis we investigated the possibility of coherent interactions between radiation and matter, i.e., superradiance, within the context of the ISM.

1.1 Superradiance

When a two-level atom/molecule interacts with a radiation field whose wavelength corresponds to the energy difference between its energy levels, the atom/molecule becomes excited and eventually decays to its ground state, spontaneously emitting a photon. Suppose that the two-level atom/molecule is placed in an ensemble consisting of N initially excited atoms/molecules identical to it. The photon spontaneously emitted by the initial atom/molecule can then be seen as phase-coherent to its neighbour in the ensemble if the two atoms/molecules are close enough. This phase coherent photon can stimulate the emission of a second photon with the same mode, the same phase and in the same direction by

the neighbouring atom/molecule. This process can continue through the whole ensemble if the atoms/molecules are spaced closely enough. As a result, the spontaneous emission is enhanced throughout the medium and the intensity of the radiation becomes proportional to N^2. This is to be contrasted with the non-coherent interaction of an ensemble with the radiation field, where the intensity depends linearly on N, the number of atoms/molecules in the ensemble. The coherence that is built up in this way is called cooperative, and the enhancement of spontaneous emission throughout the medium in such a manner is the essence of superradiance [Lin and Yelin, 2012].

1.1.1 Dicke's Model

As mentioned earlier, superradiance was discussed initially in the pioneering paper of Dicke "Coherence in Spontaneous Radiation Processes" published in 1954 [Dicke, 1954]. In this paper, Dicke studied an ensemble of initially excited N two-level identical molecules located within a spatial volume smaller than λ^3 (the so-called *small-sample*), where λ is the wavelength of the radiation interacting with the molecules. He considered the ensemble as a single quantum mechanical system and developed his formalism using the fact that the problem of N two-level molecules interacting with a classical radiation field is mathematically equivalent to the problem of N spin one-half particles subjected to a classical magnetic field. In Dicke's model, the energy levels corresponding to certain correlations between individual molecules are described and the time evolution of the system caused by the coupling of the molecules with the radiation field is discussed (it must be noted that all other factors affecting its evolution, such as collisional transitions, are neglected in his model). Dicke then showed that the decay time-scale for such a system is much shorter than the natural lifetime of the excited level of an individual molecule in the ensemble and that the intensity of the radiation is proportional to N^2, indicating a sudden peak of radiation on a short time-scale.

The key assumption in Dicke's model that allows the build-up of strong coherence through the ensemble is the molecules' permutation symmetry. In order to generate Dicke's perfect superradiance, the coupling of the molecules to the radiation field must be symmetrical with respect to exchange of any two molecules in the ensemble. In an actual situation, it seems difficult to satisfy this symmetry condition while maintaining a perfect coherence

through the ensemble. Effects such as the van der Waals interaction between molecules, neglected in Dicke's original work, compete with the build-up of coherence and introduce decoherence throughout the sample. van der Waals interactions become important when the interparticle distance, r, is smaller than λ. In a sample where some particles have different close-neighbour environments, van der Waals interactions break the permutation symmetry resulting in weakened correlations and a subsequent deviation from a perfectly symmetrical superradiance behaviour. However, coherence is preserved among those with a similar close-neighbourhood resulting in an overall radiation intensity larger than that of a fully non-coherent system [Gross and Haroche, 1982].

Dicke further extended his discussion to a *large-sample*, where the constituent molecules are distributed over a finite volume larger than λ^3. He showed that in a large-sample the coherent radiation can only be achieved in a particular direction $\mathbf{k}$ along which the radiation from different molecules interfere constructively [Dicke, 1954, 1964]. He pointed out that the intensity of radiation from such a sample can be orders of magnitude larger than the non-coherent intensity but smaller than the intensity of a perfectly symmetrical superradiant system. In fact, in a large-sample propagation effects that are negligible in a small-sample become important and break the symmetry of interaction between the molecules and the radiation. As a result, coherent interactions only build up among groups of molecules that experience a similar radiation field [Gross and Haroche, 1982].

Following Dicke's original idea, the theory of superradiance was studied by several groups [Arecchi and Courtens, 1970, Bonifacio and Preparata, 1970, Bonifacio et al., 1971a,b, Lehmberg, 1970, Rehler and Eberly, 1971, De Martini and Preparata, 1974, MacGillivray and Feld, 1981, Gross and Haroche, 1982, Schuurmans et al., 1982, Moi et al., 1983], and the initial model was augmented to incorporate symmetry-breaking effects found in actual systems. These studies were mainly inspired by the observations of superradiance in different laboratory systems.

1.1.2 Experimental Verification of Superradiance

Superradiance was observed for the first time in some infrared transitions of an HF gas in 1973 by Skribanowitz et al. [1973]. In their experiment a cylindrical large-sample of HF molecules

was optically pumped into a particular rotational level, which after some time delay led to a burst of superradiant emission. The reported peak intensity was ten orders of magnitude larger than that from ordinary spontaneous emission, which is emitted isotropically. The experimental results were found to be in good agreement with predictions made with the semi-classical theory of superradiance discussed by MacGillivray and Feld [1976] (see Section 1.2.2 for more details).

Superradiance was subsequently observed at far-infrared [Rosenberger and DeTemple, 1981] and optical [Cahuzac et al., 1979] wavelengths for large-sample realizations. It was only at millimetre and other long-wavelength domains that superradiance could be realized in a small-sample [Gross et al., 1979]. This was mainly due to the experimental difficulties in preparing a large number of excited particles in a regular pattern within a small-sample in the optical and infrared domains. In 1995, after the realization of Bose-Einstein condensates (BEC), it became possible to investigate superradiance action in small-samples interacting with short-wavelength radiation. The first observation of superradiance in a BEC sample was in 1999 by Inouye et al. [1999].

Experimental studies of superradiance led to the discovery of interesting features for this effect, which contributed significantly to the development of superradiance theory. For example, observations of the transition from the superradiance regime to amplified spontaneous emission (ASE) helped to understand the role of non-coherent relaxation/dephasing effects (e.g., collisions) in the evolution of a superradiance system. ASE systems, i.e., mirror-less lasers/masers, operate in the rate equation regime, which describes the change in the population of atomic/molecular energy levels due to non-coherent processes. The spectral line profile of ASE is similar to a thermal atomic/molecular spectral shape, although exhibiting a linewidth a few times narrower. Also, the radiation intensity output from ASE does not show the N^2 dependence or the delays observed for superradiance (see Section 1.2.3) [Siegman, 1971].

1.1.3 The Requirements of Superradiance

In essence, superradiance concerns systems in which population inversion is achieved and where the constituent atoms/molecules are closely packed; the effect is strongest and easier to

detect when neighbouring particles are separated by approximately less than the wavelength of radiation coupled to the system. Coherent interactions can be established in such a system if other relaxation or dephasing processes do not disturb the build-up of correlations among atoms/molecules, which act as radiators. When a superradiant sample is prepared in an inverted state through a pumping mechanism, the energy stored in the sample is released after a delay-time $t_{\rm D}$ for a small-sample, ($\tau_{\rm D}$ for a large-sample), which is proportional to $T_{\rm R}$ the characteristic time-scale of superradiance. The duration of a superradiant intensity burst is also set by $T_{\rm R}$. In Dicke's perfect superradiant system, in a small-sample $T_{\rm R} = \tau_{\rm sp}/N$ where $\tau_{\rm sp}$ is the spontaneous decay time of a single atom/molecule in the sample and N the number of inverted atoms/molecules. The superradiance delay time for such a small-sample is given by $t_{\rm D} = T_{\rm R} \ln(N)$.

In a large-sample the geometrical characteristics of the sample become important and, for example, in a cyclindrical large-sample as a result of propagation effects $T_{\rm R}$ is modified to

$$T_{\rm R} = \tau_{\rm sp} \frac{8\pi}{3nL\lambda^2}, \tag{1.1}$$

where L stands for the length of the sample and n represents the number density of inverted atoms/molecules [Benedict et al., 1996]. Accordingly, the average delay-time $\langle \tau_{\rm D} \rangle = T_{\rm R} \ln(N)$ depends on the geometry of the sample via $T_{\rm R}$. The parameters $\tau_{\rm D}$ and $T_{\rm R}$ are compared to the time-scales of non-coherent processes in order to determine the evolution of a non-ideal matter-field system. If a non-coherent relaxation process depletes the inversion in the system over a time-scale $T_{\rm rel}$, then the time-scale of superradiance needs to be shorter than that of the corresponding non-coherent effect to allow coherent interactions in the sample. More precisely, the system can only operate in the superradiance regime if $\tau_{\rm D}$, $T_{\rm R} < T_{\rm rel}$. However, the superradiance delay-time $\tau_{\rm D}$ is usually about an order of magnitude larger than $T_{\rm R}$, implying that $\tau_{\rm D}$ sets the necessary condition for coherent interactions.

The coherent process can be also interrupted by the so-called dephasing effects that disturb the phase matching process in a sample. Elastic collisions, for example, affect the spacing between the energy levels of the colliding particles through short-range interactions and introduce a phase shift in the quantum state of the system. Since superradiance re-

quires a symmetrical evolution throughout the sample, such dephasing mechanisms break the symmetry and weaken the cooperative process. This also implies that $\tau_{\rm D} < T_{\rm deph}$ for superradiance to ensue.

A further requirement of superradiance is velocity coherence among atoms/molecules in the system. The random thermal motions in a sample result in the Doppler line broadening effect, which can significantly reduce the number of atoms/molecules partaking in the coherent process. In fact, only those atoms/molecules that maintain a good velocity coherence experience a symmetrical coupling to the radiation field necessary for superradiance. In a sample where a good coherence cannot be preserved in the velocity field of the atoms/molecules, coherent interactions can be terminated right from the start. This also implies that superradiance cannot be expected in a thermally relaxed gas.

In summary, beside the two necessary requirements of population inversion and velocity coherence, one must also have $\tau_{\rm D} < T'$, where T' is the time-scale of the most important relaxation/dephasing effect in the sample. In a system where the aforementioned set of conditions is satisfied, superradiance can take place.

1.2 The Theory of Superradiance

The theoretical studies of superradiance after Dicke's original model [Dicke, 1954] employed mainly two different points of view. The first, and so-called Schrödinger picture considers the ensemble of N two level atoms/molecules as a full quantum mechanical system and describes superradiance as a collective and coherent spontaneous emission developed through the ensemble. This approach was also used by Dicke [1954], and is more suitable for the studies of small-samples. The second approach describes superradiance as a temporal amplification of photon noise or of an external field by an extended atomic/molecular medium, and is mainly used in the studies of large-samples. In this approach, the atomic/molecular sample is described by the polarization (or the magnetization for magnetic dipole transitions; see Chapter 2) and population inversion at each spatial point. The time evolution of these quantities, as well as that of the radiation field, provide a complete picture of the coherent effect in the large-samples. This so-called Heisenberg picture is also quantum mechanical

in nature but involves equations that are similar to the Bloch-Maxwell equations obtained in a semi-classical analysis of a matter-field system. It should be noted that these two approaches (i.e., the Schrodinger and Heisenberg pictures) describe the same physical effect and are selected based on their relative ease of use for a given system [Gross and Haroche, 1982, Benedict et al., 1996].

1.2.1 The Schrödinger Picture

In the Schrödinger picture, the matter-field system is represented by its density matrix, which for a system containing a large number of particles is a giant mathematical object. The density matrix contains a large amount of information on all the atomic/molecular and field observables that can be extracted with the corresponding density operators. As our main interest generally lies with the atomic/molecular observables, the reduced atomic/molecular density operator obtained by taking the trace over all field variables of the density matrix plays a central role in the Schrödinger picture. In this picture the evolution of the system, and accordingly that of the density matrix, follows the Schrödinger equation, resulting in the superradiance master equation. The master equation contains integration over time, all field modes, directions, as well as a summation over all couples of atoms/molecules. In a small-sample, this complicated equation reduces to a simpler form but is still difficult to solve. In the ISM, if superradiance is not rendered impossible by dephasing effects in a small-sample, the smaller number of atoms/molecules, which is reflected in the radiation intensity, makes it unlikely to observe the effect [Rajabi and Houde, 2016a,b]. For this reason, we have mainly focussed on the study of large-samples in the ISM and thus adapted the Heisenberg approach for the studies presented in this thesis.

1.2.2 The Heisenberg Picture

In a large-sample, the Heisenberg picture provides a more straightforward approach as an alternative method since it considers only the two atomic/molecular observables that are usually measured in superradiance experiments. In this approach, the atomic/molecular population inversion and polarization state, as well as the radiation field operator are defined

locally in the sample, and the evolution of the operators obeys the Heisenberg equation. The resulting set of equations for electric dipolar coupling between radiation and matter is[1]

$$\frac{\partial \hat{\mathbb{N}}}{\partial \tau} = \frac{i}{\hbar}\left(\hat{P}_0^+ \hat{E}_0^+ - \hat{E}_0^- \hat{P}_0^-\right) \tag{1.2}$$

$$\frac{\partial \hat{P}_0^+}{\partial \tau} = \frac{2id^2}{\hbar}\hat{E}_0^- \hat{\mathbb{N}} \tag{1.3}$$

$$\frac{\partial \hat{E}_0^+}{\partial z} = \frac{i\omega}{2\epsilon_0 c}\hat{P}_0^-, \tag{1.4}$$

which describes the evolution of the system in the retarded-time frame $\tau = t - z/c$, where z is the axis of propagation and c the speed of light [Gross and Haroche, 1982]. In these equations quantities $\hat{P}_0^{\pm}$ and $\hat{E}_0^{\pm}$ are, respectively, the envelopes for the polarization and the electric field vectors. The quantity $\hat{\mathbb{N}}$ is linearly proportional to the population inversion in the sample, while d and ω represent, respectively, the electric dipole matrix element and the angular frequency of the radiation field at resonance with the atomic/molecular transition.

The set of Equations (1.2) to (1.4), also known as Maxwell-Bloch equations, represent the evolution of an ideal system in which dephasing/relaxation effects are neglected. One can adapt these equations to more realistic conditions by including population decay and de-polarization terms as follows

$$\frac{\partial \hat{\mathbb{N}}}{\partial \tau} = \frac{i}{\hbar}\left(\hat{P}_0^+ \hat{E}_0^+ - \hat{E}_0^- \hat{P}_0^-\right) - \frac{\hat{\mathbb{N}}}{T_1} \tag{1.5}$$

$$\frac{\partial \hat{P}_0^+}{\partial \tau} = \frac{2id^2}{\hbar}\hat{E}_0^- \hat{\mathbb{N}} - \frac{\hat{P}_0^+}{T_2} \tag{1.6}$$

$$\frac{\partial \hat{E}_0^+}{\partial z} = \frac{i\omega}{2\epsilon_0 c}\hat{P}_0^-, \tag{1.7}$$

where T_1 and T_2 are (phenomenological) time-scales for non-coherent relaxation and dephasing, respectively [Mandel, 2010].

The resulting set of coupled non-linear equations can be only solved numerically. In this thesis, we show the results of our numerical analysis for the special case $T_1 = T_2 = T'$ for which Equations (1.5) to (1.7) can be reduced to the so-called Sine-Gordon equation

$$\frac{d^2\theta}{dq^2} + \frac{1}{q}\frac{d\theta}{dq} = \sin(\theta), \tag{1.8}$$

[1]The system of Equations (1.2) to (1.4) is derived in the slowly varying envelope approximation (SVEA) approximation (see Chapter 2 for more details).

through the following change of variables

$$\hat{\mathbb{N}} = \frac{N}{2V}\cos(\theta)\, e^{-\tau/T'} \tag{1.9}$$

$$\hat{P}_0^+ = \frac{Nd}{2V}\sin(\theta)\, e^{-\tau/T'}, \tag{1.10}$$

where θ is the so-called Bloch angle and N the number of inverted atoms/molecules within the sample volume V at $\tau = 0$. The variable q in Equation (1.8) is a dimensionless parameter defined as

$$q = 2\sqrt{\frac{z\tau'}{LT_{\mathrm{R}}}}, \tag{1.11}$$

where $\tau' = T'\left(1 - e^{-\tau/T'}\right)$. Given the initial conditions for θ and $d\theta/dq$ we can solve the Sine-Gordon equation numerically to find θ and subsequently determine the field amplitude $\hat{E}_0^{\pm}$ emerging out of the sample as a function of the retarded time τ. The intensity of the outgoing radiation I_{SR} is then calculated

$$I_{\mathrm{SR}} = \frac{c\epsilon_0}{2}\left|\hat{E}_0^+\right|^2. \tag{1.12}$$

1.2.3 Characteristics of Superradiant Emission

In Dicke's original model, the superradiant emission from an ideal small-sample composed of N atoms/molecules is characterized by a single burst where the peak intensity scales as N^2. More precisely, the intensity of superradiant pulse is given by [Dicke, 1954, Gross and Haroche, 1982]

$$I_{\mathrm{SR}} = \frac{N^2\hbar\omega\Gamma}{2}\cosh^{-2}\left[\frac{N\Gamma}{2}(t - t_{\mathrm{D}})\right], \tag{1.13}$$

where $\hbar\omega$ is the energy of a photon otherwise emitted spontaneously with a decay rate $\Gamma = 1/\tau_{\mathrm{sp}}$. As seen in Figure 1.1 the corresponding superradiant intensity reaches its maximum value after the delay time $t_{\mathrm{D}} = (N\Gamma)^{-1}\ln(N)$.

In an ideal large-sample, the superradiant intensity can be calculated numerically by solving the Maxwell-Bloch equations for the special case $T_1 = T_2 = \infty$ (see Section 1.2.2 for details). The propagation effects in a large-sample result in multiple superradiant burst events while the peak intensity of consecutive bursts gradually drops as shown in Figure 1.2. This phenomenon known as the ringing effect results from the re-absorption and re-emission

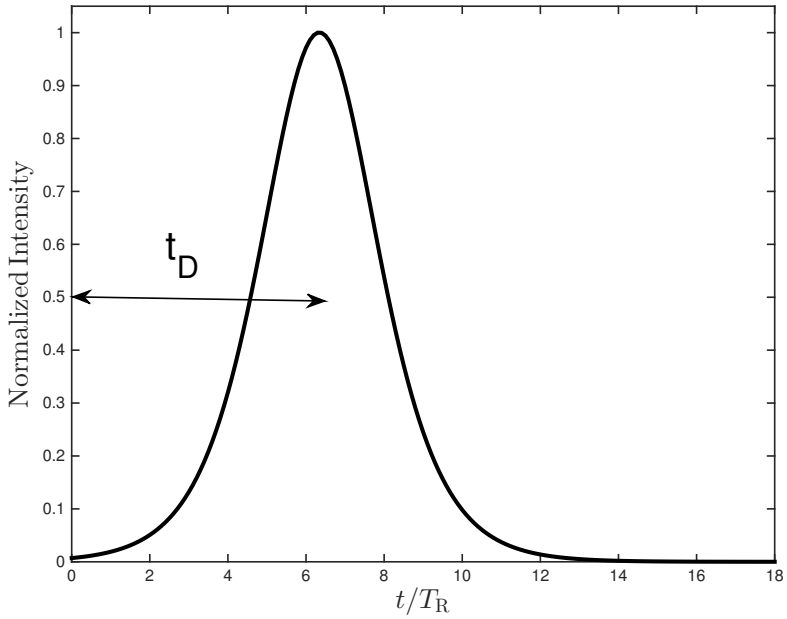

Figure 1.1: The ideal small-sample superradiant system. The normalized radiation intensity is plotted versus the time axis, scaled to the superradiance characteristic small-sample time-scale $T_{\mathrm{R}} = (N\Gamma)^{-1}$.

of photons at the observer-facing cross-section (or end-fire) of the (cylindrical) large-sample. As can be seen in the figure the first burst event for a large-sample resembles the burst for a small-sample, but T_{R} and τ_{D} characterize the output intensity differently. More precisely, a function similar as in the case of the small-sample, i.e., $\cosh^{-2}\left[(\tau-\tau_{\mathrm{D}})/(T_{\mathrm{R}}\tau_{\mathrm{D}})^{1/2}\right]$, can tailor the first burst, but with a width given by $(T_{\mathrm{R}}\tau_{\mathrm{D}})^{1/2}$ instead of τ_{sp}/N (where T_{R} is given by Equation (1.1)). In Figure 1.2 we show that the inner part of the envelope of the intensity curve can be described by $\cosh^{-2}\left(\left[(\tau-\tau_{\mathrm{D}})/\tau_{\mathrm{D}}\right]^{1/2}\right)$ (for $\tau \geq \tau_{\mathrm{D}}$), while its tail tends to $\exp\left(-\left[(\tau-\tau_{\mathrm{D}})/\tau_{\mathrm{D}}\right]^{1/2}\right)$ (for $\tau \geq \tau_{\mathrm{D}}$).

In a large-sample where dephasing/relaxation effects are included (e.g., $T_1 = T_2 = T' \neq \infty$) the number of burst events varies as a function of T'/T_{R}. In Figure 1.3, we show the intensity of superradiant emission for three different T'/T_{R}. As seen in the figure, the ringing effect is weakened as a result of dephasing/relaxation mechanisms that evidently tend to work against superradiance.

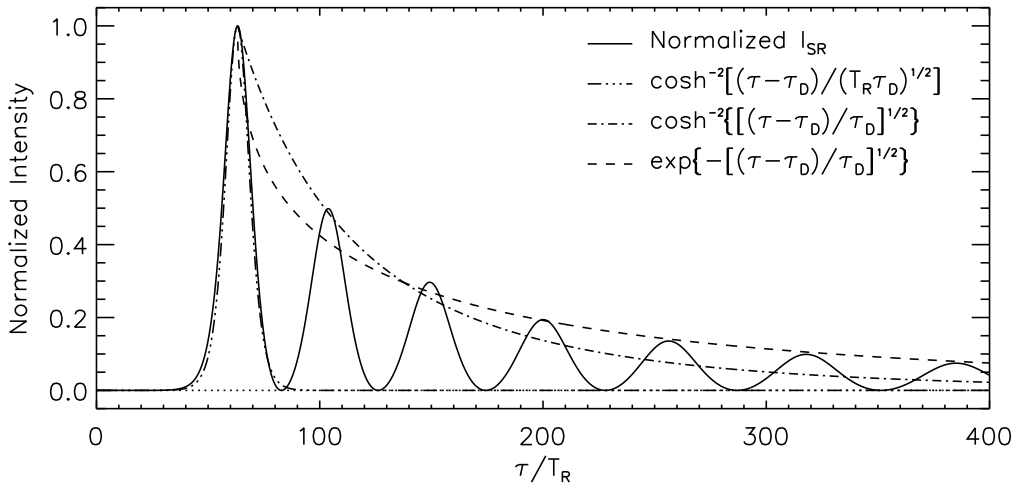

Figure 1.2: The superradiant intensity of an ideal large-sample, normalized to one, is plotted versus the retarded-time axis, scaled to the characteristic large-sample time-scale of superradiance $T_{\rm R}$.

It should be noted that superradiant emission is contained within a highly directionally focussed beam. For a cylindrical large-sample, the superradiant beam is aligned with the axis of symmetry of the sample emerging out of its end-fire.

These characteristics of superradiant emission, i.e., highly directional, intense bursts of radiation exhibiting intensity variations over a wide range of time-scales, can be used to identify coherent interactions in a medium.

1.3 Superradiance and the Maser Action

Sources characterized by high intensity radiation travelling along beams of narrow angular sizes are now routinely detected in the ISM and are associated with the maser action. A maser (Microwave Amplification by Stimulated Emission of Radiation) occurs when there is amplification of incident radiation in a medium. The main requirements for the maser action are a population inversion for the energy levels of the spectral line under consideration, sufficient velocity coherence along the line of sight, and a large enough number of atoms/molecules to provide the needed amplification (we note that these requirements are

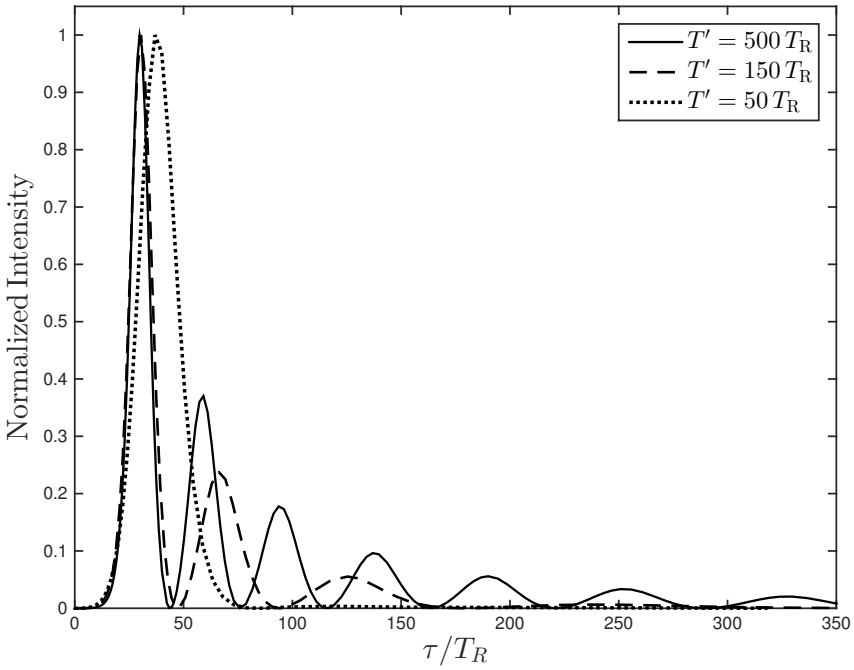

Figure 1.3: The non-ideal large-sample superradiant intensity, normalized to one, plotted versus the retarded-time, scaled to the characteristic time-scale of superradiance T_{R}, for different T'. The dephasing/relaxation effects are characterized by T'.

also needed for superradiance). Masers from several molecules (e.g, OH, H_2O, and CH_3OH) have been detected in a variety of astronomical settings. These detections not only confirm the possibility of achieving population inversion and velocity coherence in the masing regions but also point to sites where superradiance might develop. Interestingly, the monitoring of some maser sources has revealed significant intensity variations over time-scales ranging from hours to years [Gray, 2012]. Several studies were conducted with the objective of finding a viable explanation for some of the observed intensity variations within the context of maser theory, but none were fully satisfactory. Since superradiance provides a natural mechanism for intensity variations over various time-scales, the study of this phenomenon in the corresponding regions might shed light on the underlying mechanism at play at least for some of these cases.

It should be noted that, although superradiance and maser both belong to a family of

collective effects, these are two fundamentally different phenomena. In particular, unlike superradiance an astronomical maser is a non-coherent radiation process, which can operate in a steady state regime. More precisely, for a maser a group of excited atoms/molecules emit through the stimulated emission process as long as inversion can be maintained in the masing region. Superradiance, on the other hand, is a transient phenomenon, producing strong bursts of radiation taking place over a range of time-scales. The coherent interactions between matter and the radiation field, which are the essence of superradiance, require more restrictive conditions (e.g., $\tau_{\rm D} < T'$) that are more difficult to be met and maintained. This may result in transitions between maser and superradiance regimes in a given system, where superradiant requirements are only met temporarily (see Section 3.4.3 in Chapter 3 for more details). It is important to note that the maser action can be described as a series of successive events where an incident photon stimulates the emission of a subsequent photon, repeatedly throughout a sample. On the other hand, superradiance coherence emphasizes the fact that the group of atoms/molecules interacting with radiation field acts as a single quantum mechanical system [Nussenzveig, 1973].

Astronomical masers were discovered in several environments, e.g., circumstellar envelopes (CSEs) of highly eveloved stars, star-forming regions, and shocked regions where supernova remnants expand into molecular clouds [Elitzur, 1992]. In parts of this thesis, we will focus on 1612-MHz OH masers in the CSEs of evolved stars, as well as 22-GHz H_2O and 6.7-GHz CH_3OH masers near HII regions within star-forming complexes.

1.3.1 The Circumstellar Envelope of Evolved Stars – The 1612-MHz OH Maser Line

Low- to intermediate-mass stars (i.e., stars with masses of about 1 $M_\odot$ to 8 $M_\odot$) become variable in the final stages of their evolution. During this phase, some of the gas particles in the photosphere of these stars are ejected outwardly through mechanical and radiative processes, and eventually form the CSE of the star. The CSE of such stars can harbour different types of masers depending on their composition. OH 1612-MHz masers can occur in the CSE of oxygen-rich (M-type) stars (e.g., Mira variables and OH-IR stars). The

modeling of the pumping process for this line suggests that the maser action can operate at a distance of about $r \leq 10^{16}$ cm from the star [Gray, 2012]. This is where the expanding shell of the CSE reaches a terminal velocity and the condition of velocity coherence can be achieved over the so-called Sobolev length. For Mira variables or OH-IR stars the Sobolev length is typically on the order of $10^{14} - 10^{16}$ cm (see Chapter 3).

It is known that the infrared (IR) radiation emanating from warm dust, also formed in CSEs of evolved stars, is mainly responsible for the population inversion in the 1612-MHz OH line in masing regions. Changes in the brightness of the central star modulate the IR radiation from dust and subsequently the intensity of the masers. However, in some cases the intensity variations observed in the 1612-MHz line do not exhibit any correlation with that of the central star and remain unexplained. The study of superradiance in the corresponding regions may unravel the cause of such intensity variations.

1.3.2 Star-forming Regions – The 22-GHz H_2O and 6.7-GHz CH_3OH Maser Lines

Star formation is initiated by the gravitational collapse of clouds of molecular gas, which results in the formation of centrally condensed protostellar objects. The most massive stars that will ensue from the formation process (i.e., O- and early B-type stars) will be hot enough to produce ultraviolet (UV) radiation, which will ionize the ambient gas and eventually lead to the formation of highly ionized atomic hydrogen regions (i.e., the so-called HII regions). HII regions appear at a later stage in the star-forming process, and first reveal themselves as 'hyper' and 'ultra-compact' (i.e., an ucHII) when the massive protostar becomes hot enough to bring ionization. An ucHII region then expands and in the process entrains the surrounding material into some sort of organized flowing motion. Some masers (e.g., 6.7-GHz CH_3OH masers) are associated with HII regions and are accordingly categorized as 'late' masers. These late masers attain population inversion through radiative pumping via infrared radiation emitted by dust in the protostellar environment. There are, however, a class of masers (e.g., most 22-GHz H_2O masers), which can form in the earlier stages of evolution of a protostar. These masers, also known as early masers, are usually associated with shock

regions where frequent molecular collisions play an important role in the establishment of the needed population inversion [Gray, 2012]. But it should be noted that the infrared radiation from dust may also contribute to the pumping of early masers as it is not possible to have a purely collisional pump in a maser region [Goldreich and Kwan, 1974]. This is because the frequent collisions can re-establish the local thermodynamic equilibrium (LTE) conditions and thus render impossible the existence of the population inversion needed to allow the maser action.

Statistical studies of masers in star-forming regions (SFRs) indicate that masers are mostly associated with high-mass SFRs where an appreciable amplification can be achieved through the presence of large populations of maser molecules. Still, some 22-GHz H_2O masers have been detected in low-mass SFRs, in shocked gas formed by molecular outflows from young stellar objects [Gray, 2012]. The long-term monitoring of some 22-GHz H_2O masers indicated flux variations on time-scales of the order of a few days to several months [Sullivan III, 1973]. These variations were linked to changes in the pumping rates of masers or structural/dynamical variations of maser cloudlets [Peng, 1989]. However, some flaring observations show distinct behaviours that cannot be understood within the context of existing maser models.

Finally, 6.7-GHz CH_3OH masers also show intensity variations, which in some cases occur periodically or regularly [Goedhart et al., 2003]. The time-scales of these variations range from hours to months. Changes in infrared radiation, which are reflected in the pumping rate of the masers, were thought to be responsible for such time-variations. However, the observations of nearly simultaneous flarings of 6.7-GHz CH_3OH and 4.8-GHz H_2CO masers [Araya et al., 2010], or recently 6.7-GHz CH_3OH and 22-GHz H_2O masers [Szymczak et al., 2016], within relatively small spatial scales raised some fundamental questions, which are addressed in this thesis.

1.4 Dephasing/Relaxation Effects in the ISM

In order to determine the possibility of coherent interactions in the ISM, we need to identify the non-coherent processes that act as dephasing/relaxation mechanisms against superra-

diance. For any region in the ISM, collisions with hydrogen atoms and molecules, ions, electrons, or dust grains can change the internal state of an atom/molecule (inelastic collisions) or interupt the phase-locking process required for superradiance (elastic collisions). As mentioned earlier, the time-scale of dephasing/relaxation effects must be longer than the time-scale of coherent interactions (i.e., $\tau_{\rm D}$) to allow superradiance in a non-ideal system. The time-scale of inelastic collisions can be estimated with the knowledge of the collisional cross sections for appropriate density and temperature conditions in a medium, while noting that the high abundances of hydrogen (in its atomic or molecular forms, depending on the conditions) makes it the main collision partner of most atoms/molecules in the ISM. For elastic collisions, the mean time between collisions can be determined using

$$T_{\rm c} = \frac{1}{\sigma_{\rm g} n \bar{v}}, \tag{1.14}$$

where $\sigma_{\rm g}$ and n are, respectively, the geometric cross-sectional area and number density of the most important collision partner moving with the mean relative velocity $\bar{v}$. Elastic collisions are usually more frequent than inelastic collisions and are used to calculate the collisional time-scale for the superradiance samples studied in this thesis.

In the ISM, either in CSEs of evolved stars or near HII regions, the population of energy levels of atoms/molecules are affected by the infrared radiation from warm dust. As mentioned earlier, infrared radiation can act as a pump populating the energy levels corresponding to a maser line. At the same time, these couplings can be also considered as a relaxation mechanism depleting the population out of maser levels. The large dipole moments of these transitions make them very interesting, although the rate of a radiative transition is very sensitive to the opacity at the corresponding wavelength. The opacity varies over different regions and an infrared coupling route can switch roles between pumping and depleting the population of a given level. It is, therefore, sometimes important to include relaxation effects due to infrared radiation in the estimation of relaxation time-scales for superradiace.

1.5 This Thesis: Superradiance in the ISM

This thesis consists of three projects that investigate the possibilty of superradiance in the ISM. In Chapter 2 the formalism of superradiance is extended to magnetic dipolar transitions

and to transitions exhibiting circular polarization. While this chapter gives a thorough review of the theory of superradiance, it is mainly focussed on the interaction of HI samples with the 21 cm line. The search for observational signatures of superradiance for this line has yet to be conducted.

In Chapter 3 we apply the concept of superradiance to the OH molecule 1612 MHz spectral line. The interaction of this line with radiatively pumped OH samples in the CSE of evolved stars is studied. We apply our superradiance model to data found in the literature for intensity flares detected in the U Orionis Mira star and the IRAS 18276-1431 pre-planetary nebula.

In Chapter 4 we extend our superradiance analysis to the 6.7-GHz CH_3OH and 22-GHz H_2O maser lines. We show that superradiance provides a viable explanation for flaring observations of the 6.7-GHz CH_3OH and 22-GHz H_2O detected, respectively, in the G33.64-0.21 and Cep A star-forming regions. Finally, we show that superradiance provides a natural mechanism for the recent observations of seemingly alternating CH_3OH and H_2O maser flares in G107.298+5.639.

Bibliography

E. D. Araya, P. Hofner, W. M. Goss, S. Kurtz, A. M. S. Richards, H. Linz, L. Olmi, and M. Sewiło. Quasi-periodic formaldehyde maser flares in the massive protostellar object IRAS 18566+ 0408. *The Astrophysical Journal Letters*, 717(2):L133, 2010.

F. T. Arecchi and E. Courtens. Cooperative phenomena in resonant electromagnetic propagation. *Physical Review A*, 2(5):1730, 1970.

M. G. Benedict, A. M. Ermolaev, V. A. Malyshev, I. V. Sokolov, and E. D. Trifonov. *Superradiance Multiatomic Coherent Emission*. Bristol: IOP Publishing Ltd, 1996.

R. Bonifacio and G. Preparata. Coherent spontaneous emission. *Physical Review A*, 2(2): 336, 1970.

R. Bonifacio, P. Schwendimann, and F. Haake. Quantum statistical theory of superradiance. I. *Physical Review A*, 4(1):302, 1971a.

R. Bonifacio, P. Schwendimann, and F. Haake. Quantum statistical theory of superradiance. II. *Physical Review A*, 4(3):854, 1971b.

P. Cahuzac, H. Sontag, and P. E. Toschek. Visible superfluorescence from atomic europium. *Optics Communications*, 31(1):37–41, 1979.

F. De Martini and G. Preparata. Dicke superradiance and long range dipole-dipole coupling. *Physics Letters A*, 48(1):43–44, 1974.

R. H. Dicke. Coherence in spontaneous radiation processes. *Physical Review*, 93(1):99, 1954.

R. H. Dicke. The coherence brightened laser. *Quantum Electronics*, 1:35–54, 1964.

M. Elitzur. *Astronomical masers*, volume 170 of *Astrophysics and Space Science Library*. Dordrecht: Kluwer, 1992.

D. Emerson. *Interpreting astronomical spectra*. John Wiley & Sons, 1996.

S. Goedhart, M. J. Gaylard, and D. J. Van Der Walt. Periodic flares in the methanol maser source G9.62+0.20E. *Monthly Notices of the Royal Astronomical Society*, 339(4):L33–L36, 2003.

P. Goldreich and J. Kwan. Astrophysical masers. V. pump mechanism for H2O masers. *The Astrophysical Journal*, 191:93–100, 1974.

F. Gounand, M. Hugon, P. R. Fournier, and J. Berlande. Superradiant cascading effects in rubidium Rydberg levels. *Journal of Physics B: Atomic and Molecular Physics*, 12(4):547, 1979.

M. Gray. *Maser Sources in Astrophysics*. New York: Cambridge University Press, 2012.

M. Gross and S. Haroche. Superradiance: An essay on the theory of collective spontaneous emission. *Physics Reports*, 93:301–396, December 1982.

M. Gross, P. Goy, C. Fabre, S. Haroche, and J. M. Raimond. Maser oscillation and microwave superradiance in small systems of Rydberg atoms. *Physical Review Letters*, 43(5):343, 1979.

S. Inouye, A. P. Chikkatur, D. M. Stamper-Kurn, J. Stenger, D. E. Pritchard, and W. Ketterle. Superradiant Rayleigh scattering from a Bose-Einstein condensate. *Science*, 285 (5427):571–574, 1999.

Y. Kaluzny, P. Goy, M. Gross, J. M. Raimond, and S. Haroche. Observation of self-induced Rabi oscillations in two-level atoms excited inside a resonant cavity: The ringing regime of superradiance. *Physical Review Letters*, 51(13):1175, 1983.

R. H. Lehmberg. Radiation from an n-atom system. I. general formalism. *Physical Review A*, 2(3):883, 1970.

G. D. Lin and S. F. Yelin. 6 superradiance: An integrated approach to cooperative effects in various systems. *Advances in Atomic Molecular and Optical Physics*, 61:295, 2012.

J. C. MacGillivray and M. S. Feld. Theory of superradiance in an extended, optically thick medium. *Physical Review A*, 14(3):1169, 1976.

J. C. MacGillivray and M. S. Feld. Limits of superradiance as a process for achieving short pulses of high energy. *Physical Review A*, 23(3):1334, 1981.

P. Mandel. *Nonlinear optics*. Wiley-VCH, 2010.

L. Moi, P. Goy, M. Gross, J. M. Raimond, C. Fabre, and S. Haroche. Rydberg-atom masers. I. A theoretical and experimental study of super-radiant systems in the millimeter-wave domain. *Physical Review A*, 27(4):2043, 1983.

H. M. Nussenzveig. *Introduction to Quantum Optics*. New York: Gordon & Breach, 1973.

R. S. Peng. Time variation of type I H2O masers. I-long term flux density variation of the W49N H2O maser. II-a preliminary model for the time variation of H2O masers in ordinary, physically quiet environments. *Astronomy and Astrophysics*, 216:165–184, 1989.

J. M. Raimond, P. Goy, M. Gross, C. Fabre, and S. Haroche. Statistics of millimeter-wave photons emitted by a Rydberg-atom maser: An experimental study of fluctuations in single-mode superradiance. *Physical Review Letters*, 49(26):1924, 1982.

Fereshteh Rajabi and Martin Houde. Dickes superradiance in astrophysics.I. the 21 cm Line. *The Astrophysical Journal*, 826(2):216, 2016a.

Fereshteh Rajabi and Martin Houde. Dickes superradiance in astrophysics. II. the OH 1612 MHz line. *The Astrophysical Journal*, 828(1):57, 2016b.

N. E. Rehler and J. H. Eberly. Superradiance. *Physical Review A*, 3(5):1735, 1971.

A. T. Rosenberger and T. A. DeTemple. Far-infrared superradiance in methyl fluoride. *Physical Review A*, 24(2):868, 1981.

M. F. H. Schuurmans, Q. H. F. Vrehen, D. Polder, and H. M. Gibbs. Superfluorescence. *Advances in atomic and molecular physics*, 17:167–228, 1982.

A. E. Siegman. *An introduction to lasers and masers*. McGraw-Hill, 1971.

N. Skribanowitz, I. P. Herman, J. C. MacGillivray, and M. S. Feld. Observation of Dicke superradiance in optically pumped HF gas. *Physical Review Letters*, 30(8):309, 1973.

W. T. Sullivan III. Microwave water vapor emmision from Galactic sources. *The Astrophysical Journal Supplement Series*, 25:393, 1973.

M. Szymczak, M. Olech, P. Wolak, A. Bartkiewicz, and M. Gawroński. Discovery of periodic and alternating flares of the methanol and water masers in G107.298+5.639. *Monthly Notices of the Royal Astronomical Society: Letters*, 459(1):L56–L60, 2016.

Q. H. F. Vrehen, H. M. J. Hikspoors, and H. M. Gibbs. Quantum beats in superfluorescence in atomic cesium. *Physical Review Letters*, 38(14):764, 1977.

Chapter 2

Dicke's Superradiance in Astrophysics. I – The 21 cm Line[1]

2.1 Introduction

It is generally assumed that in much of the interstellar medium (ISM) emission emanating from atomic and molecular transitions within a radiating gas happen independently for each atom or molecule. From intensity measurements of such spectral lines, important parameters (e.g., density and temperature) can be determined and the physical conditions in a given environment thus characterized [Townes and Schawlow, 1955, Emerson, 1996, Goldsmith and Langer, 1999, Irwin, 2007]. For example, in cases where the spectral lines are optically thin, the intensity will be found to scale linearly with the number of atoms or molecules responsible for the detected radiation. The soundness of this approach rests mostly on the assumption that spontaneous emission from different atoms or molecules happens independently.

As was pointed out by R. H. Dicke in a seminal paper several decades ago [Dicke, 1954], the assumption of independent spontaneous emission for the components of a gas does not apply in all conditions. As will be discussed in this paper, and following Dicke's original analysis, closely packed atoms can interact with their common electromagnetic field and radiate coherently. That is, the spontaneous emission of atoms or molecules in such a gas

[1]Rajabi, F., & Houde, M. 2016, The Astrophysical Journal, 826, 216

will not be independent, but rather take place in a cooperative manner. In the ideal case, this phenomenon will lead to a much more intense and focused radiation (proportional to the square of the number of atoms), which Dicke called superradiance. Since Dicke's original proposal, the field of superradiance research has flourished, and an abundant literature has developed within the physics community. The first experimental detection of superradiance in the laboratory was achieved by Skribanowitz et al. [1973], while several other independent verifications [Gross et al., 1976, Gibbs et al., 1977, Carlson et al., 1980, Moi et al., 1983, Greiner et al., 2000, Xia et al., 2012] have since been realized under a large domain of conditions and experimental setups (see Chap. 2 of Benedict et al. 1996, MacGillivray and Feld 1976, Andreev et al. 1980, Gross and Haroche 1982 for reviews).

While the reality of the superradiance phenomenon has long been clearly established in the laboratory, to the best of our knowledge it has yet to be investigated within an astrophysical context. It appears to us important to do so since some of the requirements and conditions needed for the realization of a superradiant system are known to be satisfied in some regions of the ISM. More precisely, superradiance can arise in systems where there is a population inversion, and the effect will be much stronger and more likely to be realized when atoms or molecules are separated by approximately less than the wavelength of radiation (see below and Section 2.3.2).

The population inversion condition is known to occur in the ISM and is partly responsible for the ubiquitous presence of masers (see Fish 2007, Watson 2008, Vlemmings 2012, Sarma 2012 for recent reviews). But it is also important to realize that, although it is a necessary condition, population inversion is not by itself sufficient to ensure superradiance. It is also required that sufficient velocity coherence exists between the atoms partaking in the effect, and that any other dephasing takes place on time-scales longer than those characterizing superradiance. When all these conditions are met, a coherent behavior can be established between the atoms, and superradiance can ensue. We note, however, that, as will be discussed later on, superradiance is unlikely to take place in thermally relaxed regions of the ISM. This is because Doppler broadening resulting from, say, a Maxwellian velocity distribution would leave too few atoms with the required velocity coherence to allow superradiance to develop. Our analysis will therefore imply other types of environments where

thermal equilibrium has not been reached. For example, any region in the ISM into which a significant amount of energy is being suddenly released (e.g., shocks or regions where significant radiation flares occur) will be strongly out of equilibrium and provide conditions that are potentially markedly different from those found in a thermal gas and may meet the requirements for superradiance. Also, although superradiance can also occur for large interatomic or molecular separations (i.e., greater than the wavelength of radiation; see Section 2.3.1), the aforementioned constraint of small interatomic or molecular separation, and its implication for the corresponding densities, is likely to be met for only a limited number of spectral lines, but a few astrophysically important transitions are suitable candidates. One of these spectral lines is the 21 cm atomic hydrogen transition.

Even though a 21 cm maser has yet to be discovered, which would also imply the realization of a population inversion for this spectral line, as will be seen through our analysis the length-scales required for superradiance at 21 cm are very small compared to those that would be needed for maser amplification in the ISM (Storer and Sciama 1968, and see below). It follows that, although the lack of observational evidence of masers for this transition significantly affects the probability of detecting superradiance, it does not rule it out. Also, the existence of higher densities of atomic hydrogen in some parts of the ISM would increase the potential detectability of superradiance if the other necessary conditions for its realization previously listed were also met. Furthermore, with the recent discoveries of radio bursts at frequencies close to 1400 MHz [Kida et al., 2008, Thornton et al., 2013], the investigation of the properties of a transient phenomenon such as superradiance is timely. This is why in this first paper on the subject we chose to introduce the concept of superradiance to the ISM using this spectral line.

Whether or not a population inversion can easily be realized for the energy levels leading to the 21 cm line, it has been considered in the existing literature [Shklovskii, 1967, Storer and Sciama, 1968, Dijkstra and Loeb, 2008], and we know of at least one region (the Orion Veil) where the kinetic temperature is lower than the 21 cm spin temperature, providing evidence for a population inversion [Abel et al., 2006]. The main pumping process covered in the literature corresponds to the situation when a H I gas is close to a source of radiation that emits a field with an intensity $I_v(\nu)$ in the neighborhood of the Lyα line. A hydrogen

atom in the ground hyperfine state ($n = 1,\ F = 0$) can absorb a photon and become excited to the $n = 2$ level. Later on, the atom returns to the upper hyperfine state ($n = 1,\ F = 1$), emitting a slightly less energetic photon than the initial one absorbed by the atom. The same can happen for a hydrogen atom initially in the hyperfine state ($n = 1,\ F = 1$) that returns to the ground ($n = 1,\ F = 0$) state after excitation to the $n = 2$ level, emitting a slightly more energetic photon in the process. The absorption rate of the photons for both cases depends on the intensity of the radiation $I_v\,(\nu)$, but the return (emission) process does not. Therefore, the $F = 0$ level will undergo more absorptions followed by a return to the ($n = 1,\ F = 1$) level whenever $I_v\,(\nu)$ harbors more blue than red photons and will become accordingly less populated than the $F = 1$ level [Wouthuysen, 1952, Field, 1958, Shklovskii, 1967, Storer and Sciama, 1968]. Although Storer and Sciama [1968] concluded that it is unlikely to maintain a population inversion over the extended region needed for the maser amplification with this process, they also pointed out that an "appreciable" inversion can thus be realized over a region of thickness $\sim 6 \times 10^{-5}$ pc. Given the above inversion scenario, we would expect that environments located in the periphery or near boundaries of H II regions could provide conditions suitable for the development of superradiance, for example. The aforementioned evidence for a 21 cm population inversion in the Orion Veil brings support to this idea. Whatever the case, the 21 cm line will serve us as a starting point for the development of the superradiance formalism for the ISM (in the present case for a magnetic dipolar transition), which will then be refined in the future and also applied to other (electric dipolar) spectral lines (e.g., the OH 1612 MHz, CH_3OH 6.7 GHz, and H_2O 22 GHz maser transitions) where observational evidence for superradiance can be found in the literature [Rajabi and Houde, 2016, Rajabi and Houde, 2016].

It should also be pointed out that superradiance is a fundamentally different phenomenon from the maser action, even though the two may seem similar at first glance. An astronomical maser is a collective but not coherent phenomenon. More precisely, for a maser, a group of atoms, initially in their excited states, emit through the stimulated emission process but cannot be considered as a single quantum system. That is, it is possible to describe maser action through successive events where an excited atom is stimulated by the incident radiation and emits a photon, with the same stimulation/emission processes subsequently

repeated for different atoms in the masing sample. In contrast, for superradiance, coherence emphasizes the fact that the group of atoms interacting with the radiation field behaves like a single quantum system [Nussenzveig, 1973]. That is, the superradiance emission process cannot be broken down into successive events, as is the case for maser radiation. Finally, superradiance is a transient effect in which a strong directional pulse is radiated over a relatively short time-scale, while maser action operates more in a steady-state regime as long as population inversion is maintained.

The material covered in this paper goes as follows. We start with a general discussion of the concept of superradiance for the so-called small and large samples, as originally discussed by Dicke [1954, 1964], in Section 2.2. In Section 2.3, we examine the possibility of building cooperative behavior in a H I sample based on a comparative analysis of time-scales for the 21 cm line in a H I gas, as well as present corresponding numerical results. A discussion and short conclusion follow in Sections 2.4 and 2.5, respectively, while the superradiance formalism and detailed derivations for the material discussed in the main sections of the paper will be found in appendices at the end of this chapter.

2.2 Superradiance

2.2.1 Dicke's Small-sample Model

Dicke originally proposed in 1954 a model where an ensemble of N initially inverted two-level atoms interacting with their common radiation field is considered as a single quantum mechanical system [Dicke, 1954]. In his model, a two-level atom is modeled as a spin-1/2 particle in a magnetic field where the spin up configuration corresponds to the excited state $|e\rangle$ and the spin down to the ground state $|g\rangle$. Just as an ensemble of N spin-1/2 particles can be described using two quantum numbers s and m_s, the eigenstates of the combined N two-level atoms in Dicke's model can also be labeled with two quantum numbers r and m_r such that $0 \leq r \leq N/2$ and $m_r = -r, -r+1, \ldots, r-1, r$, where

$$m_r = \frac{N_e - N_g}{2}, \tag{2.1}$$

with N_e and N_g the number of particles in the excited and ground states, respectively.

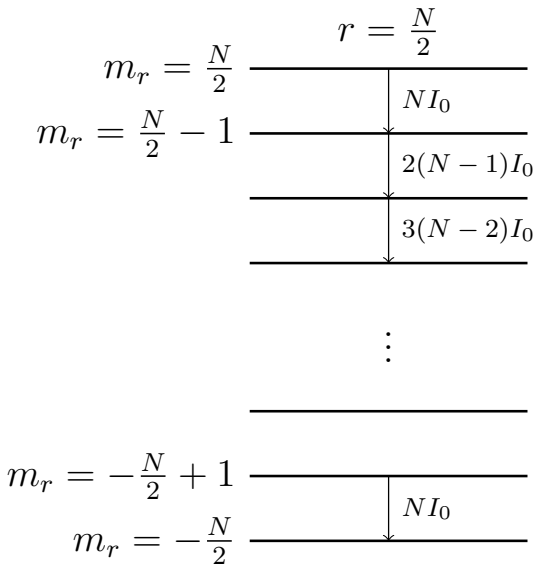

Figure 2.1: Dicke states with $r = N/2$ for a system of N two-level (spin-1/2) particles. Spontaneous radiation intensities are indicated on the right.

From the complete set of eigenstates characterizing this quantum mechanical system, those symmetrical under the permutation of any pair of atoms are particularly important and are called Dicke states. The initial state $|e, e, ..., e\rangle$ of N fully inverted spin-1/2 particles corresponding to N fully inverted two-level atoms is one such Dicke state and is identified by $r = N/2$ and $m_r = N/2$. When an atom in the ensemble decays to its ground state by emitting a photon, the quantum number m_r is decreased by one while r remains unchanged, and the system moves to another symmetric state. Dicke showed that the radiation intensity from such an ensemble cascading from the initial ($r = N/2$, $m_r = N/2$) state down through an arbitrary state (r, m_r) is

$$I = I_0 \left(r + m_r\right) \left(r - m_r + 1\right) \tag{2.2}$$

if the volume containing the ensemble of N two-level atoms is much smaller than λ^3, the cube of the wavelength of the radiation interacting with the atoms. In Equation (2.2), I_0 is the radiation intensity due to spontaneous emission from a single two-level atom. This particular type of system and density condition defines a *small sample*. This cascading process is depicted in Figure 2.1.

Furthermore, Dicke pointed out that in the ($r = N/2$, $m_r = 0$) state, where the half of the atoms are in the ground state and the other half in the excited state, the radiation intensity of the system is maximum at

$$I = I_0 \left(\frac{N}{2}\right)\left(\frac{N}{2}+1\right) \tag{2.3}$$

$$\propto N^2 I_0, \tag{2.4}$$

implying a significantly enhanced radiation beam, a phenomenon he named *superradiance*. This can be understood by the fact that when the distance between neighboring atoms is much smaller than the wavelength of radiation, the photon emitted by one atom is seen to be in phase by neighboring atoms and can bring about the emission of a new photon of the same mode and in the same direction as the initial photon. This process can continue through the whole ensemble, resulting in an intense superradiant radiation pulse proportional to N^2 (see Equation [2.4]). In contrast to the superradiance observed in a perfectly coherent system, in a noncoherent system all atoms act independently with a radiation intensity scaling linearly with N. This possibility of coherent interactions is in contrast with the common assumption that, in the ISM, atoms, for example, mainly interact independently with the radiation field, such that the intensity of the radiation is a linear function of the atomic density.

In order to conduct a more careful investigation of the possibility of coherent interactions, especially superradiance in a H I gas, we will need to adapt Dicke's original theory to the corresponding astrophysical conditions. We therefore first need to carefully understand all the assumptions that lead to a symmetrical ensemble and superradiance in the original model of Dicke [1954]. The main assumptions can be listed as follows:

- A small sample of neutral atoms is confined to a volume $\mathcal{V} \ll \lambda^3$ with the walls of the volume transparent to the radiation field.

- The N two-level atoms in the sample are separated by a distance much less than λ but distant enough not to worry about any overlap between the wave functions of neighboring atoms, which would require that the wave functions be symmetrized.

- The ensemble of N initially inverted hydrogen atoms possesses a permutation symmetry under the exchange of any pair of atoms in the sample. This is a restricting condition that could prove difficult to satisfy in general.

- The transition between atomic levels takes place between nondegenerate levels, collisions between atoms do not affect their internal states, and collisional broadening is neglected as a result of the small size of the sample [Dicke, 1953].

- Although it is mentioned in Dicke [1954] that the main results of his study are independent of the type of coupling between atoms and the field, the interaction of the atoms with the radiation field in Dicke's model is assumed to be electric dipolar.

- Finally, the radiation field is assumed to be uniform through the small sample, the electric dipoles associated with the atoms are parallel, and propagation effects neglected.

Comparing a corresponding small sample of N neutral hydrogen atoms interacting with the 21 cm line in the ISM with a Dicke sample, we can see that some of the assumptions made in the Dicke formalism hold and some do not. For example, the transitions between the hyperfine states of a hydrogen atom take place between nondegenerate levels since the external magnetic field in the ISM lifts the upper-level degeneracy (see Section 2.3). Also, a small sample of H I atoms found in many regions in the ISM would readily verify the criterion that $N \gg 1$ in a volume $\mathcal{V} < \lambda^3$ and could thus be approximately assumed to experience the same 21 cm radiation field without consideration of propagation effects. On the other hand, unlike in Dicke's sample, collisional and Doppler broadening effects should, in the most general case, be considered because, for example, collisions between hydrogen atoms affect the internal hyperfine states in their electronic ground state through spin de-excitation [Field, 1958]. Most importantly, it must also be noted that the type of coupling between hydrogen atoms and the 21 cm line is magnetic dipolar in nature.

Above all, the permutation symmetry of atoms, which is a key assumption in the Dicke model, is difficult to preserve in an actual situation because of dipole-dipole interactions between the atoms. Dipole-dipole interactions have a r'^{-3} dependency, and these short-range interactions become important in small samples where the distance between atoms

r' is smaller than λ (see Section 2.3.1). In the Dicke model, the symmetry-breaking effect of dipole-dipole interactions is ignored. In later studies of superradiance (e.g., Gross and Haroche 1982), it has been shown that in general dipole-dipole interactions break the permutation symmetry, except in those configurations where all atoms have identical close-neighbor environments. This symmetry-breaking effect results in weakened correlations and a subsequent deviation from a perfectly symmetrical superradiance behavior (i.e., the $I \propto N^2$ relation in Equation [2.4]). In a sample of N atoms, if s atoms ($s < N$) experience a similar close neighborhood, the correlation can build up among this group of atoms, and the intensity of radiation from the whole sample is expected to be larger than the intensity of a fully noncoherent system ($I_{\rm nc}$) but smaller than that of a perfect superradiance system ($I_{\rm SR}$).

In a small sample of N neutral hydrogen atoms in the ISM, it may thus appear possible to develop coherent behaviors if the permutation symmetry is conserved among a group of atoms in the sample. This is arguably a reasonable assumption on average for an ensemble of atoms within the small volumes discussed here. That is, the different atoms in the sample are likely to be subjected to the same conditions when averaged over time and space. Furthermore, we also note that in a H I-sample the magnetic dipole-dipole interactions are definitely weaker than the electric dipole-dipole interactions discussed in the literature focusing on symmetry-breaking effects.

2.2.2 Dicke's Large-sample Model

In his first paper on superradiance, Dicke also extended his formalism to a large sample, where the volume of the sample $\mathcal{V} > \lambda^3$ and the interatomic distance r' between some atoms can be greater than λ. He showed that, in a large sample, coherent radiation can occur in a particular direction $\mathbf{k}$ in which the radiation from different atoms is in phase. When the phase-matching condition is satisfied in some direction $\mathbf{k}$, the initial state of the system can be described by a correlated symmetric state of type (r, m_r), and the intensity of the radiation in a solid angle along $\mathbf{k}$ follows

$$I(\mathbf{k}) = I_0(\mathbf{k}) \left[(r + m_r)(r - m_r + 1) \right], \tag{2.5}$$

similar to Equation (2.2) for a small sample. When a photon is emitted in the direction $\mathbf{k}$, the system cascades to a lower state obeying the selection rules $\Delta r = 0$, $\Delta m_r = -1$, and similar to the case of a small sample, symmetrical states of the same r are coupled to each other through coherent transitions (see Section 2.3.1). On the other hand, when a radiated photon has a wave vector $\mathbf{k}' \neq \mathbf{k}$, the states with different r (i.e., of different symmetry) can couple, and consequently the coherence is weakened in the system [Dicke, 1954]. It follows that in a large sample consisting of N inverted atoms, the radiation by one atom is only seen to be in phase by a group of atoms (contrary to a small sample where the radiation field is assumed uniform over the whole sample), and correlation can only be developed among this group. This naturally results in a radiation intensity that is greater than that of the corresponding fully non-coherent system but smaller than the superradiance intensity of a perfectly coherent system consisting of N atoms.

Finally, in a large-sample as a result of possibly large interatomic distances (i.e., $r' > \lambda$) the symmetry breaking effects of the dipole-dipole interactions are less important, whereas the propagation effects that are absent in a small-sample cannot be neglected. The propagation of radiation over a large distance in a large-sample results in the reabsorption and reemission of the photons and consequently leads to a nonuniform evolution of the atoms in the sample (see Section 2.3.2). Beyond these factors, Dicke's analysis of the large-sample includes assumptions similar to those used for the small sample.

2.3 The Two-level H I sample

Let us consider an ensemble of neutral hydrogen atoms in the electronic ground state in some region of the ISM, where it can emit or absorb photons at the $\lambda = 21$ cm wavelength. The hydrogen 21 cm line is perhaps the most important source of information in radio astronomy and arises from the transition between two levels of the hydrogen atom in the 1s ground state. The interaction between the electron spin and the proton spin in the nucleus of the atom splits the otherwise degenerate 1s energy level into the two $F = 0$ and $F = 1$ sub-levels. The $F = 1 \leftrightarrow 0$ transition in the absence of an external magnetic field produces the 21 cm line, corresponding to a frequency $\nu = 1420.406$ MHz.

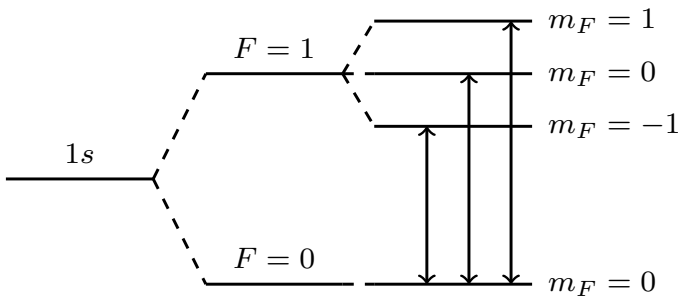

Figure 2.2: Energy level diagram for the HI 21 cm line in the presence of a Zeeman-splitting external magnetic field.

Considering a more realistic case, the magnetic field in a cold neutral gas is generally on the order of 10 μG [Crutcher, 2012], and the energy level corresponding to $F = 1$ splits into three sublevels identified by $m_F = -1, 0,$ and 1. The interaction between the $F = 0$ and $F = 1$ levels becomes more complicated as this splitting provides three possible hyperfine transitions, as shown in Figure 2.2. These hyperfine transitions link states of like parity and obey the general magnetic-dipole selection rules $\Delta F = 0, \pm 1$ and $\Delta m = 0, \pm 1$. Based on these rules, all of the three transitions shown in Figure 2.2 are allowed; however, depending on the relative orientation (or the polarization) of the magnetic component of the radiation field to the quantization axis of the atom, some transitions may be favored. In the more general case, there is a mixture of all three transitions, with each transition exhibiting particular polarization properties. In order to better understand the coherent and cooperative evolution of a sample of N hydrogen atoms coupled to its radiation field, it will be simpler for us to focus our analysis on only one of these transitions and consider the atomic system as an ensemble of two-level atoms. Although this model represents a significant simplification, the two-level atom approximation is extensively used for, and its results are well verified in, laboratory experiments involving more complicated atomic or molecular systems with more complex energy levels [Mandel, 2010].

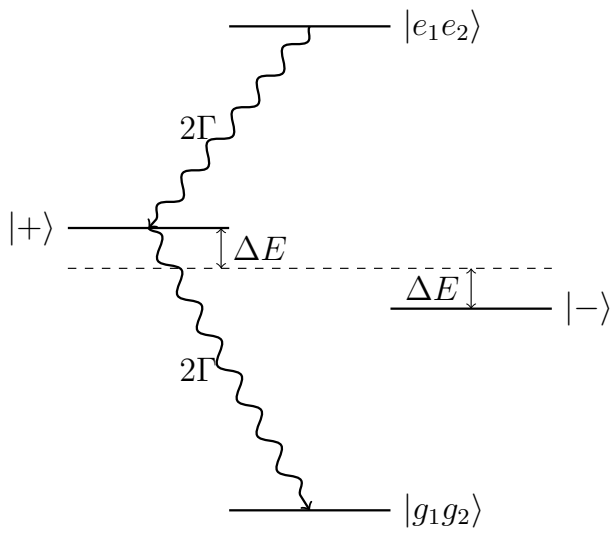

Figure 2.3: The two-hydrogen-atom system. When $kr' \ll 1$ the upper and lower symmetric states $|e_1e_2\rangle$ and $|g_1g_2\rangle$, respectively, couple to the intermediate symmetric state $|+\rangle$ at the enhanced transition rate 2Γ, where Γ is the transition rate of a single atom acting independently. In contrast, the antisymmetric state $|-\rangle$ cannot couple to the upper and lower states because of the cooperative behavior between the two atoms. The energy level shifts $\pm\Delta E$ for the $|\pm\rangle$ states are also shown.

2.3.1 Magnetic Dipole-dipole Interaction between Hydrogen Atoms

The theoretical model for the problem can be found in Appendix 2.A, where the Hamiltonian for the two-level H I sample is developed and the main equations of superradiance are derived. To simplify our discussion, we have limited our analysis to the $|F = 0,\ m = 0\rangle \longleftrightarrow |F = 1,\ m = +1\rangle$ transition through which a hydrogen atom emits a left circular polarization (LCP) photon, i.e., with its electric field vector rotating counter-clockwise as seen by the observer facing the incoming wave. One of the main components of the Hamiltonian is the magnetic dipole energy term $\hat{V}_{\mathrm{MD}}$ that describes the interaction between the atoms composing the sample (see Equations [2.50] and [2.62]). We now focus on this interaction to get a sense of how the needed cooperative behavior for superradiance develops between atoms.

Hydrogen Atoms Separated by a Small Interatomic Distance ($r' < \lambda$)

In order to have a better understanding of how cooperative behavior is built up in a sample of N atoms, it is helpful to first study the simpler case of two atoms. We specifically consider a system consisting of two hydrogen atoms, once again assuming each atom is a two-level system with the excited state $|e\rangle$ ($F = 1$) and the ground state $|g\rangle$ ($F = 0$). The two atoms are initially excited, and the state of the system is given by $|e_1\rangle \otimes |e_2\rangle = |e_1 e_2\rangle$. Eventually one of the two atoms spontaneously decays to its ground state, emitting a photon with a wavelength λ and energy $\hbar\omega$. If the interatomic distance r' is much smaller than λ (i.e., $kr' \ll 1$) and the two atoms are identical, then one cannot say which atom has emitted the photon nor which is in a given state. In the case of the two-level hydrogen atom discussed here, this decay rate must be related to that of the corresponding magnetic dipole transition given by (in MKS units)

$$\Gamma = \frac{\mu_0 k^3 \left| \langle e | \hat{\mathbf{M}} | g \rangle \right|^2}{3\hbar\pi}. \tag{2.6}$$

We can furthermore express the state of the system by either a symmetric $|+\rangle$ or antisymmetric $|-\rangle$ combination of the $|e_1 g_2\rangle$ and $|g_1 e_2\rangle$ state vectors, such as

$$|+\rangle = \frac{1}{\sqrt{2}} \left(|e_1 g_2\rangle + |g_1 e_2\rangle \right) \tag{2.7}$$

$$|-\rangle = \frac{1}{\sqrt{2}} \left(|e_1 g_2\rangle - |g_1 e_2\rangle \right), \tag{2.8}$$

which, at this stage of our analysis, have the same energy and are thus degenerate (see below).

We now refine this model by adding the magnetic dipole-dipole interaction term to the system's Hamiltonian. In this model, the magnetic dipole from one atom, say, $\hat{\mathbf{M}}_1$, interacts with the magnetic field $\hat{\mathbf{B}}_2$ due to the dipole of the other atom located at a position $\mathbf{r}' = r'\mathbf{e}_{r'}$ away in the near field, where $kr' \ll 1$ [Jackson, 1999]

$$\hat{\mathbf{B}}_2(\mathbf{r}') = \frac{\mu_0}{4\pi} \left[\frac{\cos(kr')}{r'^3} + \frac{\sin(kr')}{r'^2} \right] \left[3\mathbf{e}_{r'} \left(\mathbf{e}_{r'} \cdot \hat{\mathbf{M}}_2 \right) - \hat{\mathbf{M}}_2 \right]. \tag{2.9}$$

It can be shown that when the two dipoles are aligned, the term of the interaction Hamiltonian that is relevant to the present discussion is

$$\hat{H}_{\mathrm{dd}} = -\frac{\mu_0 k^3 \mu_{\mathrm{B}}^2}{2\pi} \left(3\left|\beta\right|^2 - 1\right) \left[\frac{\cos\left(kr'\right)}{\left(kr'\right)^3} + \frac{\sin\left(kr'\right)}{\left(kr'\right)^2}\right] \left(\hat{R}_1^+ \hat{R}_2^- + \hat{R}_1^- \hat{R}_2^+\right), \tag{2.10}$$

with $\beta = \mathbf{e}_L \cdot \mathbf{e}_{r'}$. The raising/lowering operators $\hat{R}_1^+$, $\hat{R}_1^-$, and so on are defined in Equation (2.47) and the LCP unit vector state $\mathbf{e}_L$ in Equation (2.54), while μ_{B} is the Bohr magneton. It can further be shown, through a simple diagonalization exercise, that this interaction Hamiltonian lifts the degeneracy between the $|+\rangle$ and $|-\rangle$ states of Equations (2.7) and (2.8), with their corresponding energies becoming [Protsenko, 2006]

$$E_\pm = E_0 \pm \Delta E, \tag{2.11}$$

with E_0 the unperturbed energy of the states and

$$\Delta E = \frac{\mu_0 k^3 \mu_{\mathrm{B}}^2}{2\pi} \left(3\left|\beta\right|^2 - 1\right) \left[\frac{\cos\left(kr'\right)}{\left(kr'\right)^3} + \frac{\sin\left(kr'\right)}{\left(kr'\right)^2}\right]. \tag{2.12}$$

It is then also possible to verify through Equation (2.6), setting $\hat{\mathbf{M}} = \hat{\mathbf{M}}_1 + \hat{\mathbf{M}}_2$, that the transition rates $\Gamma_\pm$ for the $|\pm\rangle$ states with the initial $|e_1 e_2\rangle$ and final $|g_1 g_2\rangle$ states are

$$\Gamma_+ = 2\Gamma \tag{2.13}$$

$$\Gamma_- = 0, \tag{2.14}$$

where Γ is the transition rate of a single atom acting independently.

The differentiation of energy levels brought about by the magnetic dipole-dipole interaction is, therefore, seen to be a function of β and the interatomic distance r'. More important, however, is the doubling of the transition rate for the symmetric state $|+\rangle$ and the cancellation of that of the antisymmetric state $|-\rangle$. Such enhanced and reduced rates are respectively associated with superradiance and subradiance. This scenario for the two-atom system is depicted in Figure 2.3.

This behavior can also be understood by considering the symmetry of the system's Hamiltonian and states. The fact that, as could easily be verified, the Hamiltonian of the system

of two atoms (including the magnetic dipole term $\hat{V}_{\rm MD}$) is totally symmetric under the permutation of the two aligned atoms when $kr' \ll 1$ implies that only states of like symmetry can be coupled. It follows that since the initial state $|e_1 e_2\rangle$ of the fully inverted system is also symmetric, it can only couple to the $|+\rangle$ intermediate state, and from there to the symmetric ground state of the system $|g_1 g_2\rangle$. Accordingly, it is interesting to note that under these conditions a system prepared in the intermediate antisymmetric state $|-\rangle$ will not decay to the ground state since $\Gamma_- = 0$. This is evidently different from the case of a noncoherent system where both atoms eventually decay to their individual ground states $|g\rangle$ at the rate Γ. We therefore see that superradiance and subradiance are characteristics of a coherent system, where the intensity of radiation does not scale linearly with the number of atoms, as is the case for a noncoherent system.

When the effect discussed here is generalized to a sample composed of N atoms confined within a volume $\mathcal{V} \ll \lambda^3$ (a small sample), we find that some of the conditions that prevailed for the two-atom case are not realized. Most importantly, Equations (2.11) and (2.12) indicate that this interaction leads to a distribution of energy levels in the system unless the atoms all have similar nearest neighborhoods (e.g., a ring-like periodic distribution of atoms; Gross and Haroche 1982). This spread in energy levels will tend to reduce the strength of the superradiance effect.

It has nonetheless been observed through numerical calculations and experiments that coherent behaviors still apply to N-atom small-sample systems where radiation is of long enough wavelength [Gross et al., 1979], as is the case for the 21 cm line. For $kr' \sim 1$ the ratio $\Delta E/E_0 \sim \Gamma/\omega$ is exceedingly small for the 21 cm line, and the time-scale associated with the energy shifts is on the order of $\hbar/\Delta E \sim (kr')^3\,\Gamma^{-1}$ [Benedict et al., 1996], which for the H I densities considered in this paper renders this type of dephasing negligible. As will be discussed later, dephasing due to collisions are more likely to set the time-scale for homogeneous dephasing. The same is not necessarily true at short wavelengths, where it is very difficult to place a large number of atoms within a subwavelength dimension in a regular pattern, and in such a sample strong dipole-dipole interactions break the symmetry and terminate the coherent behavior by introducing large energy-level shifts. Thus most of the experimental observations of superradiance took place at longer wavelengths (i.e., in the

infrared as opposed to optical; Benedict et al. 1996).

For an inverted N-atom small sample with initially uncorrelated dipoles, the first photon emitted by one of the atoms interacts with the dipole moments of the other atoms, resulting in the build-up of correlation between them. After some time, known as the delay time $t_{\rm D}$, a very high degree of correlation is developed in the system, where in the strongest superradiance regime, the N microscopic dipoles eventually act like one macroscopic dipole. The rate of emission is then enhanced to $N\Gamma$, while the radiation intensity is proportional to N^2 and becomes highly directional, being focused in a beam with a temporal half-width on the order of $1/(N\Gamma)$.

It should also be noted that the correlation between dipoles can be triggered by an external source, such as an input radiation field. This can happen if the input radiation field is stronger than the spontaneous fluctuations in the sample and the coupling of the dipoles to the external field leads to coherent behaviors. An enhancement of radiation through coupling to an external field is called *triggered superradiance* [Benedict et al., 1996].

It can be shown that the superradiance radiation intensity $I_{\rm SR}$ of an ideal H I small-sample composed of N inverted atoms is given by [Dicke, 1954, Gross and Haroche, 1982, Benedict et al., 1996]

$$I_{\rm SR} = N^2 \hbar\omega\Gamma \cosh^{-2}\left[N\Gamma\left(t - t_{\rm D}\right)\right], \tag{2.15}$$

where $\hbar\omega$ is the energy of the corresponding atomic transition and the aforementioned delay time $t_{\rm D} = (N\Gamma)^{-1}\ln(N)$. In Figure 2.4 the radiation intensity of a HI small sample with $N = 75$ atoms confined within a cube of length 4 cm ($\simeq \lambda/5$ for the 21 cm line) is plotted as a function of time using Equation (2.15). The intensity is normalized to $NI_{\rm nc}$, where $I_{\rm nc} = N\hbar\omega\Gamma$ is for the corresponding noncoherent smallsample. It can be seen in Figure 2.4 that the energy stored in the small sample is radiated away in a single burst. After time $t = t_{\rm D}$, the intensity reaches its maximum value, N times that of the noncoherent intensity, and the peak intensity of the normalized plot becomes equal to one. In this H I sample, $\Gamma^{-1} = 3.5 \times 10^{14}$ s [Draine, 2012], the delay time $t_{\rm D} = 2.0 \times 10^{13}$ s, and the characteristic time of superradiance is $T_{\rm R} = (N\Gamma)^{-1} = 4.6 \times 10^{12}$ s. It should also be pointed out that in such a sample the correlation between dipoles is initiated by internal

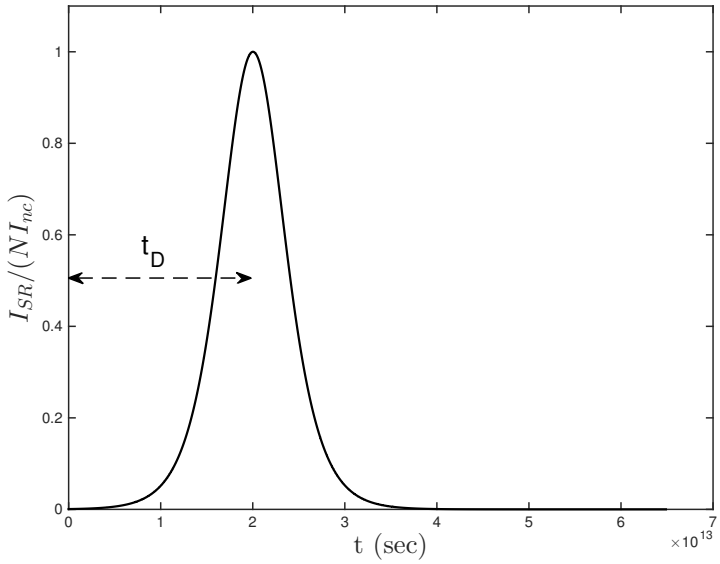

Figure 2.4: The ideal HI small-sample superradiant system. The radiation intensity is plotted as a function of time t, for $N = 75$ atoms confined within a cube of $L = 4$ cm. After the delay time $t_{\rm D} = 2.0 \times 10^{13}$ seconds the system radiates coherently in a single burst of radiation.

spontaneous fluctuations, and it is assumed that we are dealing with an ideal system, where the dipole-dipole symmetry-breaking effects are negligible and there are no other relaxation mechanisms (i.e., cooperative emission is the only decay mechanism).

In a real system, there are some relaxation and dephasing effects that compete with the build-up of the correlation, and in order to subsequently have superradiance, its characteristic timescale $T_{\rm R}$ and delay time $t_{\rm D}$ must be shorter than (in some exceptional cases on the order of) the relaxation/dephasing time-scales [Gross and Haroche, 1982, Benedict et al., 1996]. The nonideal case will be discussed in Section 2.3.2.

Two Hydrogen Atoms Separated by a Larger Interatomic Distance ($r' > \lambda$)

Let us still assume that the atoms are prepared initially in their excited states, with the state of the two-atom system given by $|e_1 e_2\rangle$. Similar to the subwavelength case, a first photon is radiated, leaving the system in an intermediate state, which, unlike for the subwavelength case, will be described with any combination of $|e_1 g_2\rangle$ and $|g_1 e_2\rangle$ states with each having

equal probability contributions, that is, not only by the $|+\rangle$ and $|-\rangle$ states. More precisely, if we associate the general symmetric state

$$|S\rangle = \frac{1}{\sqrt{2}}\left(|e_1 g_2\rangle + e^{i\phi}|g_1 e_2\rangle\right) \tag{2.16}$$

with the intermediate state shown on the left side of Figure 2.5, then we should assign its orthogonal antisymmetric state

$$|A\rangle = \frac{1}{\sqrt{2}}\left(|e_1 g_2\rangle - e^{i\phi}|g_1 e_2\rangle\right) \tag{2.17}$$

to the intermediate state on the right side of the figure [Dicke, 1964]. In Equations (2.16) and (2.17), ϕ is a phase term discriminating between the multiple choices for the intermediate states. To get a better understanding of the transition probabilities for these states, it is useful to refer to Equation (2.62) for the magnetic dipole interaction term with a radiation field for two atoms separated by $\mathbf{r}'$ and for a given $\mathbf{k}$. We then find that for coupling to, say, the $|e_1 e_2\rangle$ state the following term comes into play:

$$\hat{V}_{\mathrm{MD}} \propto \hat{R}_1^+ + \hat{R}_2^+ e^{ikr'\cos(\theta')}, \tag{2.18}$$

where θ' is the angle between $\mathbf{k}$ and $\mathbf{r}'$. Given that the transition probability (and rates) are proportional to $\left|\langle e_1 e_2|\,\hat{V}_{\mathrm{MD}}\,|S\rangle\right|^2$ and $\left|\langle e_1 e_2|\,\hat{V}_{\mathrm{MD}}\,|A\rangle\right|^2$ [Grynberg et al., 2010], we calculate using Equation (2.16), (2.17), and (2.18)

$$\Gamma_S \propto \cos^2\left\{\frac{1}{2}\left[\phi - kr'\cos\left(\theta'\right)\right]\right\} \tag{2.19}$$

$$\Gamma_A \propto \sin^2\left\{\frac{1}{2}\left[\phi - kr'\cos\left(\theta'\right)\right]\right\}. \tag{2.20}$$

We therefore see that, although the first photon can be emitted in any direction θ', its direction of emission determines ϕ and the intermediate state of the system since the transition probabilities peak at $\phi - kr'\cos\left(\theta'\right) = 2m\pi$ for Γ_S and $\phi - kr'\cos\left(\theta'\right) = n\pi$ for Γ_A (m and $n \neq 0$ are integers). Going through the same exercise for the $|g_1 g_2\rangle$ state shows a

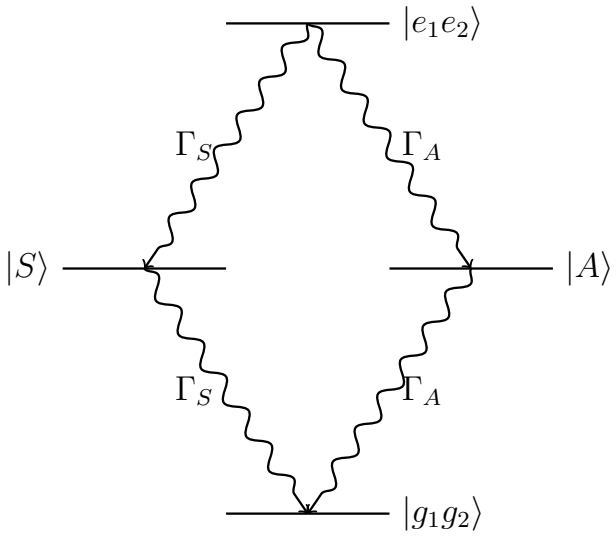

Figure 2.5: The two-hydrogen-atom system separated by $r' > \lambda$. The upper and lower symmetric states $|e_1e_2\rangle$ and $|g_1g_2\rangle$, respectively, couple to the intermediate symmetric $|S\rangle$ and antisymmetric $|A\rangle$ states with the corresponding transition rates Γ_S and Γ_A. The direction of emission of the first photon determines the intermediate state of the system, and the direction of the second photon is correlated with that of the first.

similar dependency on θ' and ϕ as in Equations (2.19) and (2.20), which implies that these transitions rates will also be likely to peak at the same value of ϕ. It follows that there is an angular correlation between two successive photons, where the direction of the second photon is correlated with the direction of the first. This angular correlation can take place even when the atoms are placed several wavelengths apart, as a result of their coupling to a common electromagnetic field, and favors intense radiation along elongated geometries (e.g., pencil-like or cylindrical structures; Dicke 1964).

Depending on the intermediate state of the system, two different classes of transitions are possible; coherent and noncoherent. If the emission of the first photon leaves the system in a symmetric intermediate state (e.g., $|S\rangle$), the symmetric coupling to the radiation field results in the coherent behavior, and consequently the system decays to the symmetric ground state $|g_1g_2\rangle$ with the corresponding transition rate shown in Figure 2.5. In contrast,

if the system is in the antisymmetric intermediate state $|A\rangle$ the coupling to the radiation field will be antisymmetric under the exchange of the atoms as they interact with the nonuniform electromagnetic field, and the system decays noncoherently to the ground state $|g_1 g_2\rangle$ with the decay rate Γ_A.

We can also explain this classically by considering two classical radiators separated by a distance $r' > \lambda$. Over large distances, the phase and the polarization of the radiation field emitted by each radiator varies from place to place. When the radiation from the two identical radiators interferes, the intensity of the total field is given by

$$I_{\text{tot}} \propto \left\langle (\mathbf{B}_1 + \mathbf{B}_2)^2 \right\rangle \tag{2.21}$$

$$\propto \left\langle B_1^2 \right\rangle + \left\langle B_2^2 \right\rangle + 2 \left\langle \mathbf{B}_1 \cdot \mathbf{B}_2 \right\rangle, \tag{2.22}$$

and can become as large as four times the intensity of a single radiator I_0 if

$$\langle \mathbf{B}_1 \cdot \mathbf{B}_2 \rangle \sim I_0. \tag{2.23}$$

If the phase of the radiation from different radiators does not match perfectly, the term containing the correlation $\langle \mathbf{B}_1 \cdot \mathbf{B}_2 \rangle$ in Equation (2.22) becomes smaller than I_0 and consequently the total intensity I_{tot} decreases until it reaches its minimum for completely out-of-phase radiators. Furthermore, the correlation term can vanish when radiators act independently. In this case, the total intensity becomes equal to the sum of the intensities of the two independent radiators (the so-called noncoherent system).

2.3.2 The N-atom Large sample $\left(\mathcal{V} > \lambda^3\right)$

We can extend our discussion for the case of two distant atoms (i.e., $r' > \lambda$) to a large sample consisting of N atoms distributed over a volume $\mathcal{V} > \lambda^3$. As stated above, the build-up of correlations in an extended N-atom sample can be understood as a constructive interference of the radiation by different atoms. In a large sample as a result of propagation over large distances (i.e., larger than λ), the phase of the radiation varies throughout the sample ($kr' \gg 1$ and $e^{i\mathbf{k}\cdot\mathbf{r}'} \nsim 1$). Consequently, the phase of the atomic magnetization differs

with position. In an inverted large sample, the radiations from different atoms interfere with each other, and when the magnetizations of the radiators are perfectly in phase, an intense propagating wave is produced in one direction (the phase-matching condition cannot be satisfied in all directions).

In order to better understand the phase-matching process, it is useful to go back to the angular correlation effect described in the two-atom case. In a large sample of N inverted atoms, when the first photon is emitted, other atoms interact with its radiation field, and the direction of the next photon is affected by the first one. In a more general sense, when a photon is radiated in a particular direction $\mathbf{k}$, it becomes more probable to observe the second photon in the same direction $\mathbf{k}$ than any other direction. Thus, as the atoms radiate, an angular correlation builds up in the sample that triggers the phase-matching process in a well-defined direction.

Ideal superradiance is the result of the symmetrical evolution of an atom-field system, and in a large sample, the propagation effects result in the nonuniform evolution of the atoms in the sample. In order to better understand propagation effects in a large sample, the atomic medium can be divided into small identical slices with dimensions larger than λ but much smaller than the length of the sample. A microscopic dipole is then associated with each slice with its magnitude being proportional to the number of excited atoms in the corresponding slice. At the beginning, the dipoles in different slices are independent and their radiation uncorrelated. After some time (or the so-called retarded time delay τ_{D}; see Equation (2.34)), as they interact with their common radiation field, the dipoles lock in to a common phase, and act as a single macroscopic dipole radiating intensely with $I_{\mathrm{SR}} = NfI_{\mathrm{nc}}$, where Nf is the enhancement factor of the superradiant intensity I_{SR} over the noncoherent intensity I_{nc} determined by the efficiency of the common phase-locking process (through the value of $f \leq 1$). The enhancement factor Nf can become very large in samples with $N \gg 1$, and it converges to N in an atomic system with dimensions of the order of λ, resulting in $I_{\mathrm{SR}} = NI_{\mathrm{nc}}$ for the most efficient phase-locking process seen in a small sample. In other words, $f < 1$ implies a limited coherent behavior in a large sample resulting in a smaller output intensity and weakened superradiance, whereas $f = 1$ indicates a fully coherent behavior leading to an intense radiation and perfect superradiance [Gross and Haroche, 1982, MacGillivray and

Feld, 1976].

This approach has the shortcoming that it cannot explain the initiation of the radiation in the system by spontaneous fluctuations, and to overcome this problem phenomenological fluctuations of dipoles in the initial stages of the evolution can be added to the formalism. In contrast, triggered superradiance can be fully explained in this manner because the correlation process is initiated by an external field, which can be defined classically. It must be pointed out that the results of this method are valid only if the propagation time of the radiation τ_{E} through a sample of length L (i.e., $\tau_{\mathrm{E}} = L/c$) is smaller than the superradiance characteristic time T_{R} given by

$$T_{\mathrm{R}} = \tau_{\mathrm{sp}} \frac{16\pi}{3n\lambda^2 L}, \tag{2.24}$$

where $\tau_{\mathrm{sp}} = 1/\Gamma$ is the spontaneous decay time of a single atom and n the density of inverted atoms (see MacGillivray and Feld 1976, Rosenberger and DeTemple 1981, and Appendix 2.B). This condition (i.e., $\tau_{\mathrm{E}} < T_{\mathrm{R}}$) is known as the Arecchi-Courtens condition, and it ensures that the atomic magnetization in different parts of the sample can lock into a common phase and coherent behavior can develop through the sample.

In Appendix 2.A, we derive the evolution equations for the radiation field and the atomic system using the Heisenberg representation, while in Appendix 2.B we solve the corresponding Maxwell-Bloch system of equations, at resonance, within the framework of the slowly varying envelope approximation (SVEA). To do so, we adopted the following form for the radiation magnetic field and atomic magnetization:

$$\hat{B}_L^{\pm}(\mathbf{r},t) = \hat{B}_0^{\pm}(\mathbf{r},t)\, e^{\pm i(kz-\omega t)} \tag{2.25}$$

$$\hat{\mathcal{M}}^{\pm}(\mathbf{r},t) = \hat{\mathcal{M}}_0^{\pm}(\mathbf{r},t)\, e^{\pm i(kz-\omega t)}, \tag{2.26}$$

with $\hat{B}_0^{\pm}$ and $\hat{\mathcal{M}}_0^{\pm}$ corresponding to slowly varying envelope operators. The superradiance of a cylindrical large sample of length L under ideal conditions is then found to be determined by the following equations for, respectively, the magnetization, the population inversion, and the magnetic field:

$$\hat{\mathcal{M}}_0^+ = \frac{\mu_{\rm B} N}{2\sqrt{2}V}\sin(\theta) \tag{2.27}$$

$$\hat{\mathbb{N}} = \frac{N}{V}\cos(\theta) \tag{2.28}$$

$$\hat{B}_0^+ = \frac{i\mu_{\rm B}}{2\sqrt{2}\gamma}\frac{\partial\theta}{\partial\tau}, \tag{2.29}$$

where $\gamma = \mu_{\rm B}^2/2\hbar$. The solution for the Bloch angle θ as a function of the retarded time $\tau = t - L/c$ is obtained through the so-called Sine-Gordon equation:

$$\frac{d^2\theta}{dq^2} + \frac{1}{q}\frac{d\theta}{dq} = \sin(\theta) \tag{2.30}$$

with

$$q = 2\sqrt{\frac{z\tau}{LT_{\rm R}}}. \tag{2.31}$$

In Figure 2.6 we show the solution for the radiation intensity of such an ideal, cylindrical large sample of H I atoms of length $L = 0.02\,cT_{\rm R}$, where c is the speed of the light, by numerically solving Equations (2.27)-(2.31). For these calculations we set a Fresnel number of unity to reduce the impact of diffraction losses, which are not taken into account in our model. This yields a cylinder of radius

$$w = \sqrt{\frac{\lambda L}{\pi}}, \tag{2.32}$$

which for our ideal sample results in $w = 0.036\,(cT_{\rm R})^{1/2}$.

In this sample, the Arecchi-Courtens condition is satisfied (i.e., $\tau_{\rm E} \ll T_{\rm R}$), allowing the use of the homogeneous condition $\theta_0 = 4.9 \times 10^{-12}$ rad for the initial value of the Bloch angle. More precisely, for the large sample used for the figure, we assumed that internal fluctuations dominate over triggered superradiance, and the initial Bloch angle was set with $\theta_0 = 2/\sqrt{N}$ [Gross and Haroche, 1982].

In Figure 2.6, the retarded-time axis is scaled to $T_{\rm R}$ and the radiation intensity to $NI_{\rm nc}$, that is, the number of inverted atoms times the corresponding noncoherent intensity that would otherwise be expected from such a sample. More precisely, for comparison purposes

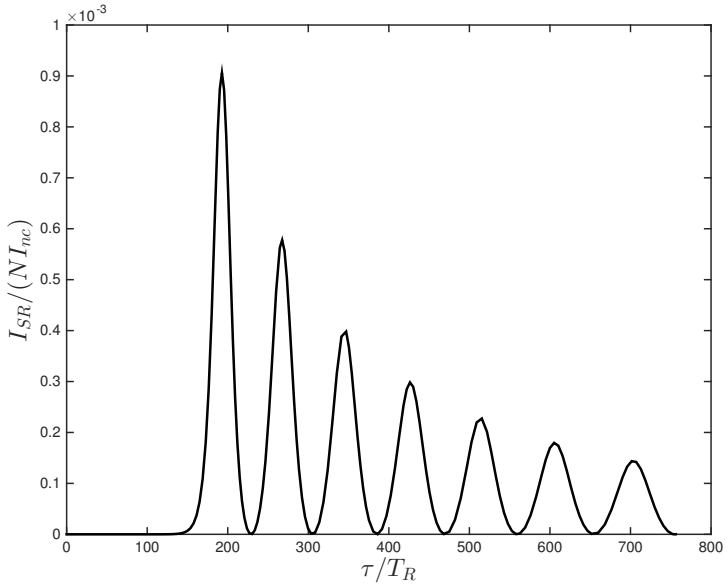

Figure 2.6: The ideal cylindrical HI large-sample. The radiation intensity, scaled to $NI_{\rm nc}$, is plotted versus the retarded time $\tau = t - L/c$ normalized to the superradiance characteristic time-scale $T_{\rm R}$. The length and radius of the cylinder are, respectively, $L = 0.02\, cT_{\rm R}$ and $w = 0.036\,(cT_{\rm R})^{1/2}$.

we consider the non-coherent intensity emanating through the sample's end-fire (i.e., the end facing the observer) of area A, within the superradiance radiation beam solid angle $\phi_{\rm D} = \lambda^2/A$ (in the direction $\mathbf{k}$ along which the phase-locking condition is satisfied) normalized to the solid angle associated with the total noncoherent radiation. We thus have

$$\begin{aligned} I_{\rm nc} &= N\hbar\omega\left(\frac{1}{A\tau_{\rm sp}}\right)\left(\frac{\phi_{\rm D}}{4\pi}\right) \\ &= \frac{4}{3}\frac{\hbar\omega}{AT_{\rm R}}, \end{aligned} \tag{2.33}$$

where Equation (2.24) was used for the last step, and $N\hbar\omega$ is the total energy initially stored in the sample. As shown in the figure, this energy is radiated away through multiple bursts, a phenomenon known as the ringing effect. This effect can be explained by the fact that atoms in different locations in the sample radiate at different times. In other words, an atom at location $z = z_0$, prepared in the excited state at $\tau = 0$, radiates its energy away and

decays to its ground state, then later on absorbs the energy radiated by another atom at a location $z < z_0$ and becomes excited, leading to another radiation event.

In a large sample, just as in a small sample, internal field fluctuations or an external field trigger superradiance, and after the delay time $\tau_{\rm D}$ the atoms radiate coherently. But contrary to a small sample, the large sample delay time depends on the initial conditions and is given by [Benedict et al., 1996]

$$\tau_{\rm D} \simeq \frac{T_{\rm R}}{4} \left| \ln \left(\frac{\theta_0}{2\pi} \right) \right|^2 . \tag{2.34}$$

In Figure 2.6 the first burst of radiation occurs after $\tau_{\rm D} \simeq 160\, T_{\rm R}$, which is consistent with the value one finds using Equation (2.34). As can also be seen, this first intensity burst only carries out a fraction of the total energy stored in the sample, while the remaining radiation happens through subsequent bursts. The number of burst events depends on the length of the sample, and as the length is increased radiation emanates through a larger number of bursts, while the peak intensity of consecutive burst events gradually drops. This is a consequence of energy conservation and the fact that, in a larger (i.e., longer) sample, radiation from different groups of atoms along the sample arrive at the end-fire at different times, and the process of absorbing the radiation, developing correlations between the dipoles, and eventually reemitting the radiation repeats multiple times over a very long period of time. On the other hand, when the length of the sample is decreased, the ringing effect becomes weaker until, for a small sample of dimension of order of λ, it totally washes out and we only observe a single burst of radiation carrying away all the energy stored in the system (as in Figure 2.4). Finally, we note that although the maximum radiation intensity seen in Figure 2.6 seems to imply that $f \sim 0.001 \ll 1$, the large number of atoms present in the sample ensures that $I_{\rm SR} \gg I_{\rm nc}$ (see Section 2.4). We should also note, however, that the Sine-Gordon equation is very sensitive to initial conditions. It therefore follows that the exact shape of the intensity curve, for example, the number of bursts in Figure 2.6, is also strongly dependent on θ_0.

Nonideal Case: Dephasing Effects

As was mentioned earlier, the characteristic timescale of superradiance $T_{\rm R}$ and the delay time $\tau_{\rm D}$ (for a large-sample) must be shorter than the relaxation/dephasing time-scales to allow the build-up of correlations in a nonideal sample. These effects include natural broadening due to the spontaneous decay time-scale $\tau_{\rm sp}$ of a single atom and collisional broadening related to the mean time between collisions $\tau_{\rm coll}$ for an atom in the sample. Although, as was stated in Section 2.1, our analysis is aimed at regions of the ISM where thermal equilibrium has not been reached and where consequently the assignation of a temperature to determine, for example, collision rates is perhaps ill-defined, we will nonetheless adopt such a procedure for the rest of our discussion to get a sense of the time-scales involved. Accordingly, in a H I gas different types of collisions can take place depending on the temperature and density. For environments of temperatures ranging from approximately 10 K to 300 K, which are the focus of our analysis, collisions between two neutral hydrogen atoms (H-H collisions) dominate and fall into two categories: elastic and inelastic. During an elastic H-H collision, the spacing between the atomic energy levels is slightly affected, but no transition between them is induced. The change in energy spacing occurs as a result of short-range interaction forces between the two colliding particles and induces a phase shift in the wave function of the scattered atoms. After a number of elastic collisions, an atom can lose coherence with the interacting radiation field as a result of the randomness in the perturbations. In contrast, in an inelastic H-H collision, the internal energy of the hydrogen atoms will be changed. This occurs when the two hydrogen atoms with oppositely directed electron spins approach each other at distances less than approximately 10^{-8} cm. This process is known as electron exchange or the spin de-excitation effect. As a result of such a collision, the induced phase shift can lead to a change in the internal spin states [Wittke and Dicke, 1956], and it is found that spin de-excitation is the dominating relaxation process in a high-density collision-dominated H I gas. We therefore find that H-H collisions not only can affect the strength of a potential coherent 21 cm radiation by removing from the population of the excited hyperfine states, they also contribute to the line breadth and can change the shape of the spectral line by affecting the spacing between internal energy levels. For example, the

time-scale of H-H collisions is estimated to be on the order of 10^8 s in the case of elastic scattering and 10^9 s for spin de-excitations, using the mean effective collisional cross sections given in Irwin [2007] for a H I gas at $T = 100\,\mathrm{K}$ and $n = 10\,\mathrm{cm}^{-3}$. The mean time between collision τ_{coll} is thus set to the shortest of these time-scales and must at least be larger than T_{R} and τ_{D} to allow coherent behavior (see Section 2.4).

In addition, other broadening effects, such as Doppler broadening, are further dephasing mechanisms that can destroy cooperative behavior if their time-scales (importantly the so-called Doppler dephasing time, i.e., the reciprocal of the Doppler width) are smaller than T_{R} and τ_{D} [Meziane et al., 2002, Bonifacio and Lugiato, 1975]. In a thermally relaxed gas, thermal motions are probably the most important dephasing effects and result in line broadenings that correspond to very short dephasing time-scales (e.g., $T_{\mathrm{therm}} \sim 10^{-3}$ s at $T = 100$ K). In the presence of such strong dephasing effects, correlations cannot develop between the dipoles, and any coherent interaction will be terminated right from the start. Hence our earlier comment that we do not expect to find superradiance under conditions of thermal equilibrium, but potentially only in (out-of-equilibrium) regions where strong velocity coherence can be maintained along the line of sight. Furthermore, this condition may be only met among a group of atoms in such regions, therefore reducing the number of inverted atoms in the sample that could participate in coherent interactions. However, we know from maser observations that a high level of velocity coherence can be achieved in some regions of the ISM, and we expect that superradiance could happen under similar conditions. As was mentioned in Section 2.1, the main inversion pumping mechanism likely involved for the 21 cm transition points to the surroundings of H II as potential sites for superradiance in this spectral line. It follows that we should also anticipate an analogous (very small) volume filling factor for the emitting regions of superradiant sources as for masers.

In Figure 2.7 the intensity of the H I large sample discussed in Section 2.3.2 (and presented in Figure 2.6 for the ideal case) is plotted as a function of the retarded time τ for the special case where dephasing/relaxation effects are included and characterized by a single time-scale set to $T' = 541\,T_{\mathrm{R}}$ (see Section 2.4 and Appendix 2.B). These results were obtained by once again numerically solving Equation (2.30), while the magnetization and population inversion are given by

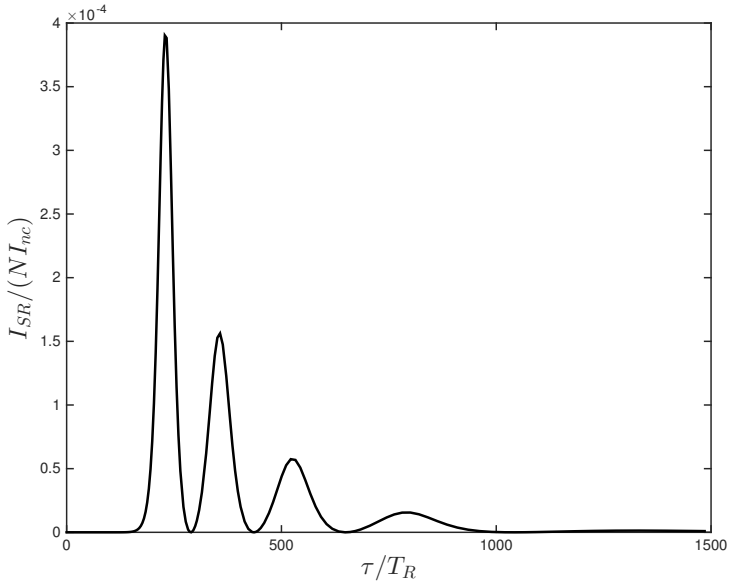

Figure 2.7: The non-ideal HI cylindrical large-sample. All parameters are as in Figure 2.6, except that dephasing/relaxation effects are included for the special case where they are characterized by a single time-scale $T' = 541\,T_{\rm R}$. The ringing effect is weakened as a result of the dephasing.

$$\hat{\mathcal{M}}_0^+ = \frac{\mu_{\rm B} N}{2\sqrt{2}V} \sin(\theta)\, e^{-\tau/T'} \tag{2.35}$$

$$\hat{\mathbb{N}} = \frac{N}{V} \cos(\theta)\, e^{-\tau/T'}, \tag{2.36}$$

and the dimensionless parameter

$$q = 2\sqrt{\frac{z\tau'}{LT_{\rm R}}} \tag{2.37}$$

with

$$\tau' = T' \left(1 - e^{-\tau/T'}\right). \tag{2.38}$$

The magnetic field is once again given by Equation (2.29). The intensity and time axes are scaled like those of Figure 2.6 for the ideal H I sample. We can see from Figure 2.7 that the

ringing effect seen in the ideal sample is also present here but is weakened by the dephasing and basically terminated after $\tau \sim 1000\, T_{\rm R}$ (i.e., approximately the dephasing time-scale). The dephasing effects also affect the maximum energy radiated away through each burst event and result in slightly weaker intensities.

2.4 Discussion - Cooperative Behavior in a HI Gas in the ISM

As is made evident from our previous discussions, the characteristic time-scale of superradiance $T_{\rm R}$ is a fundamental criterion to consider in the investigation of this cooperative behavior. For an ideal small sample of volume $\mathcal{V} < \lambda^3 \sim 10^4$ cm^3, for total hydrogen densities $1\ \text{cm}^{-3} < n_{\rm H} < 100\ \text{cm}^{-3}$ and a population inversion $\eta \sim 0.01$, the superradiance time-scale

$$T_{\rm R} = \frac{\tau_{\rm sp}}{\eta n_{\rm H} \mathcal{V}}, \tag{2.39}$$

$$\sim \frac{10^{12}}{n_{\rm H}}\ \text{s} \tag{2.40}$$

is such that $T_{\rm R} \sim 10^{10} - 10^{12}$ s, where $\tau_{\rm sp} \sim 10^{14}$ s for the 21 cm line. As mentioned in Section 2.3.2, $t_{\rm D}$ ($\approx T_{\rm R}$, in this case) must be shorter than the relaxation/dephasing time-scales in order to allow the build-up of cooperative behaviors in the sample. In a typical H I gas, an important relaxation mechanism for an atom is collisional de-excitation, the rate for which is given by

$$\tau_{\rm coll} = \frac{1}{n_{\rm H} \kappa_{10}}. \tag{2.41}$$

Values for the collisional de-excitation rate coefficient κ_{10} for the hyperfine state $F = 1$ over a range of temperatures can be found in Zygelman [2005], and for $10\ \text{K} < T < 300\ \text{K}$ we find $\tau_{\rm coll} \sim 10^8 - 10^{12}$ s for the previous range of atomic hydrogen densities. These collision rates become $\tau_{\rm coll} \sim 10^7 - 10^{12}$ s when elastic collisions are considered [Irwin, 2007]. It can thus be seen that the expected collisional relaxation time-scales are likely to render superradiance improbable for small H I sample, especially at higher temperatures. This suggests the investigation of larger samples containing more atoms.

Although in a large sample the general cooperative behavior is weaker than the ideal Dicke superradiance, the greater number of atoms will reduce $T_{\rm R}$, increase the radiation intensity, and make it more likely to observe the effect. However, it is also important to realize that not only must the condition $T_{\rm R} < T'$ be realized for establishing superradiance, such that the noncoherent de-excitation does not become the dominant mechanism to release the energy of the system, but we must also ensure that $\tau_{\rm D} < T'$ is verified since $\tau_{\rm D} > T_{\rm R}$ from Equation (2.34). In other words, the delay time needed to establish coherence in the sample must also be smaller than the dephasing time-scale.

It is important to note that the requirement $\tau_{\rm D} < T'$ effectively sets a threshold that must be met for the onset of superradiance. From the dependency of $\tau_{\rm D}$ on the different parameters (see Equation [2.34]) we find that, for a given transition, it can only be reduced below T' through a corresponding increase of the inverted population's column density nL. It follows that superradiance will only be triggered when the column density meets or exceeds some critical value [Rajabi and Houde, 2016]. Contrary to what is the case for laboratory superradiance experiments, where short laser pulses are used to create the necessary population inversion, the existence of a threshold also implies that there is no requirement for the presence of a pulse to initiate superradiance in the ISM (but see below). It only matters that a critical level of inversion is reached, and the rate at which it is attained is irrelevant.

However, stronger superradiance bursts can be achieved in the presence of population-inverting pulses that bring the column density to levels significantly exceeding its critical value. But in such cases the values attained for nL can be limited by the pumping time $T_{\rm P}$ over which the population inversion is achieved throughout the sample. For example, as we increase the length of the sample, $T_{\rm R}$ and $\tau_{\rm D}$ decrease, but, it becomes necessary to achieve the population inversion over a larger length-scale. There are two types of pumping mechanisms available to achieve the population inversion in an atomic system: swept pumping and instantaneous pumping [MacGillivray and Feld, 1981, Gross and Haroche, 1982]. In the swept-pumping scenario, the atomic sample is pumped longitudinally by a pulse traveling along the sample, and the pumping process is characterized by a finite pumping time $T_{\rm P}$, whereas for instantaneous pumping a transverse excitation causes the simultaneous excitation of all atoms in the sample, resulting in $T_{\rm P} \approx 0$. When the pumping process cannot be

achieved instantaneously but is realized over a finite time, the output intensity of a small or a large sample is only affected slightly as long as $T_{\rm P} < \tau_{\rm D}$. The main effect of the finite pumping time is then an increase in the delay time of the superradiant process in comparison to what one expects from Equation (2.34): the actual delay time $\tau'_{\rm D}$ will be longer than the theoretical delay time $\tau_{\rm D}$ [MacGillivray and Feld, 1981].

However, if pumping occurs at an approximately constant rate over some pulse time interval in a H I gas (i.e., $dn(t)/dt \simeq \Lambda$, where Λ is a constant) and the first burst of superradiance radiation is emitted before the expected inversion density n is achieved throughout the sample, then we need to replace n by its effective value at time $t = \tau'_{\rm D}$ (i.e., $n_{\rm eff} = n\,(\tau'_{\rm D})$). In this case, only a fraction of atoms contribute to the first burst, and the system cannot emit as much of the energy stored within it through a series of coherent bursts [MacGillivray and Feld, 1981]. If the pulse (pumping) time becomes too long and the first superradiant burst is emitted before the inversion is achieved along the sample, only a few coherent bursts can be observed. This happens as the system reaches a quasi-steady state, in which the growth and depletion of population occur with the same rates. In the quasi-steady state, the radiation intensity is given by $I = \hbar\omega L\,(dn/dt)$ and is no longer proportional to N^2 [MacGillivray and Feld, 1981]. The transition from a superradiant to the quasi-steady regime was first observed in the laboratory by Gross et al. [1976]. For an astronomical system, this would correspond to passing from a superradiant system to an astronomical (mirror-less) maser. We therefore conclude that, in the ISM, superradiance will not happen in a steady-state regime, but will rather be characterized by strong variability in radiation intensities over time. One could, for example, conceive of an emitting region harboring a maser that would be episodically modulated with strong bursts of radiation due to superradiance, perhaps resulting from some radiative trigger or a sudden decrease in $\tau_{\rm D}$ (from a corresponding increase in the inverted population; for example, see Rajabi and Houde 2016, Rajabi and Houde 2016).

In a more general context, i.e., without limiting the discussion to the 21 cm line, it is also important to note that superradiance triggered through population-inverting pulses (that bring nL significantly above its critical value) cannot result if these pulses are due to collisions alone. This is because of the undesirable consequences that collisions have on the dephasing/relaxation of a sample. That is, if $T_{\rm P}$ is the pumping time due to collisions, then

we know from our previous discussion that $T_{\rm P} < \tau_{\rm D}$ for pulse-initiated superradiance to be possible. But since in this case the time-scale for collision dephasing is $T' = T_{\rm P}$, it follows that $\tau_{\rm D} > T'$ and superradiance will be inhibited by collisions.

When $N \gg 1$ we have for the average delay time $\langle \tau_{\rm D} \rangle = T_{\rm R} \ln(N)$ [Gross and Haroche, 1982], which means that $\langle \tau_{\rm D} \rangle$ is usually an order of magnitude or two larger than $T_{\rm R}$ for the large samples to be studied. As we will now see, for the range of densities and temperatures considered for our analysis, $\langle \tau_{\rm D} \rangle < T'$ can be realized in a large set of conditions. In a H I large sample where all the necessary conditions for superradiance are fulfilled (i.e., $T_{\rm P}, \tau_{\rm E} < \langle \tau_{\rm D} \rangle < T'$, with sufficient velocity coherence), we can estimate the time-scale of potential superradiance bursts using the results of our numerical analyses for the corresponding large sample, as long as the Fresnel number is kept close to unity. For the following examples we considered a density $n_{\rm H} = 10\ {\rm cm}^{-3}$ with an inversion factor $\eta = 0.01$, implying an inverted population of 940 atoms in a volume λ^3. Our results indicate that radiation bursts over time-scales on the order of days (i.e., from Figure 2.7 a few hundred times $T_{\rm R} = 10^3$ s, while $\langle \tau_{\rm D} \rangle = 5.2 \times 10^4$ s) can be associated with cylindrical H I samples of length and radius $L \approx 10^{11}$ cm and $w \approx 9 \times 10^5$ cm, respectively, while bursts over timescales on the order of minutes (i.e., $T_{\rm R} = 1$ s and $\langle \tau_{\rm D} \rangle = 66$ s) can be associated with samples with $L \approx 10^{14}$ cm (approximately equal to 6×10^{-5} pc; see Storer and Sciama 1968) and $w \approx 3 \times 10^7$ cm. In all cases, we have $T' \approx \tau_{\rm coll} > \langle \tau_{\rm D} \rangle$ over a wide range of conditions, ensuring that dephasing effects will not destroy atomic coherent behaviors, and we found $f \approx 10^{-4}$ (from Figure 2.7) with an efficiency factor Nf ranging from approximately 10^{12}-10^{24}, from the shortest to the longest sample length L. These results imply a corresponding amplification factor of 10^{10} to 10^{22} over the corresponding noncoherent intensity of such samples (taking into account the noninverted population).

Although the samples considered above would probably not yield strong detections (e.g., for the sample of length $L \approx 10^{14}$ cm and $w \approx 9 \times 10^7$ cm we calculate an integrated flux $\sim 10^{-22}\,{\rm erg\,s^{-1}\,cm^{-2}}$ at a distance of 400 pc), given the small radii considered here it is unlikely that only a single superradiant system would be realized in a region harboring an inverted population. That is, if we assume a reasonable maser spot size for the population-inverted region (e.g., $w_{\rm spot} \sim 1$ au), then it becomes possible that a very large number

of superradiant systems could simultaneously erupt ($w_{\rm spot}/w \sim 10^6$) and render a strong detection more likely when the conditions for superradiance are met [Rajabi and Houde, 2016]. This leads us to suggest, that despite the simplicity of and the approximations used in our model, significant intensity variability due to superradiance could be detectable for the 21 cm line in some regions of the ISM.

2.5 Conclusions

We have applied the concept of superradiance introduced by Dicke [1954] to the ISM by extending the corresponding analysis to the magnetic dipole interaction characterizing the atomic hydrogen 21 cm line. Our results suggest that only relatively low levels of population inversion over short astronomical length-scales (i.e., ≈ 0.001 AU) are needed to sustain the cooperative behavior leading to superradiant radiation in the ISM. This phenomenon is characterized by strong intensity variability over a range of time-scales, and our numerical calculations show that such episodic bursts of radiation could potentially happen over periods ranging from hours to months.

This first paper on this topic has, in part, served as an introduction to superradiance in the ISM, but much remains to be done. For example, we have not attempted to characterize the shapes of superradiant spectral lines or their polarization properties, which for the 21 cm line would necessitate the consideration of all hyperfine $F = 1 \leftrightarrow 0$ transitions. In subsequent publications, we thus intend to extend our analysis to tackle these questions and investigate the potential for superradiance in other important astronomical spectral lines. It would further be beneficial to broaden the scope of our analysis to include a wider range of conditions such effects as pumping, diffraction losses, and different sample geometries associated to different Fresnel numbers.

Appendices

2.A Theoretical Model

2.A.1 The Hamiltonian and the Maxwell-Bloch Equations

We follow Dicke [1954] and approximate the Hamiltonian for a sample of N hydrogen atoms with each atom acting as a two-level system, while taking into account the magnetic nature of the dipole-radiation interaction applicable to this case:

$$\hat{H} = \hat{H}_0 + \hat{H}_{\text{rad}} + \hbar \sum_{j=1}^{N} \omega_j \left(\hat{R}_{j3} + \frac{\hat{1}}{2} \right) - \sum_{j=1}^{N} \hat{\mathbf{M}}_j \cdot \hat{\mathbf{B}} \left(\mathbf{r}_j \right). \tag{2.42}$$

In this Hamiltonian equation, $\hat{H}_0$ contains the translational and interatomic interaction energies of the atoms, $\hat{H}_{\text{rad}}$ is the radiation field Hamiltonian term, $\hbar\omega_j \left(\hat{R}_{j3} + \hat{1}/2 \right)$ is the internal energy of the j^{th} two-level atom ($\hat{1}$ is the unit operator), which has the eigenvalues 0 and $\hbar\omega_j$, and the last term stands for the interaction between the electromagnetic field and the magnetic dipole of the j^{th} atom $\hat{\mathbf{M}}_j$. Since this Hamiltonian is written under the magnetic dipole approximation, it implies that the magnetic field $\hat{\mathbf{B}}$ does not change considerably over the size of the atom and is determined by its value at the position of the center of mass of the atom, $\mathbf{r}_j$. Finally, the effects of the hyperfine interaction between the proton and electron spins within a single hydrogen atom and the Zeeman interaction due to an external magnetic field would be included in the frequency ω_j of the atomic transition.

Following Dicke, we define the operators $\hat{R}_x$, $\hat{R}_y$, $\hat{R}_3$, and $\hat{R}^2$ such that

$$\hat{R}_K \left(\mathbf{r} \right) = \sum_{j=1}^{N} \hat{R}_{jK} \delta \left(\mathbf{r} - \mathbf{r}_j \right), \quad K = x, y, 3 \tag{2.43}$$

$$\hat{R}^2 \left(\mathbf{r} \right) = \hat{R}_x^2 + \hat{R}_y^2 + \hat{R}_3^2 \tag{2.44}$$

$$\left[\hat{R}^2 \left(\mathbf{r} \right), \hat{R}_K \left(\mathbf{r}' \right) \right] = 0 \tag{2.45}$$

$$\left[\hat{R}_a \left(\mathbf{r} \right), \hat{R}_b \left(\mathbf{r}' \right) \right] = i\varepsilon_{abc} \hat{R}_c \left(\mathbf{r} \right) \delta \left(\mathbf{r} - \mathbf{r}' \right), \quad a, b, c = x, y, 3, \tag{2.46}$$

which are similar to the relations found in the spin or general angular momentum formalisms.

We can also define the raising and lowering operators

$$\hat{R}^{\pm}(\mathbf{r}) = \hat{R}_x(\mathbf{r}) \pm i\hat{R}_y(\mathbf{r}), \tag{2.47}$$

which further verify the following commutation relations:

$$\begin{aligned}
\left[\hat{R}^{\pm}(\mathbf{r}), \hat{R}_3(\mathbf{r}')\right] &= \mp\hat{R}^{\pm}(\mathbf{r})\delta(\mathbf{r}-\mathbf{r}') && (2.48)\\
\left[\hat{R}^{+}(\mathbf{r}), \hat{R}^{-}(\mathbf{r}')\right] &= 2\hat{R}_3(\mathbf{r})\delta(\mathbf{r}-\mathbf{r}'). && (2.49)
\end{aligned}$$

It is clear from the form of the Hamiltonian and the commutation relations between the operators that $\hat{R}^2$ and $\hat{R}_3$ commute with $\hat{H}$ and, therefore, share the eigenfunctions $|r, m_r\rangle$ introduced in Section 2.2.1 to describe the state of the system.

The atomic hydrogen transitions at 21 cm are magnetic dipolar in nature and bring into consideration the next leading term in our analysis, i.e., the magnetic dipole interaction found on the right-hand-side of Equation (2.42):

$$\hat{V}_{\mathrm{MD}} = -\sum_{j=1}^{N} \hat{\mathbf{M}}_j \cdot \hat{\mathbf{B}}\left(\mathbf{r}_j\right), \tag{2.50}$$

which is at the center of our analysis. In general, the magnetic dipole operator $\hat{\mathbf{M}}_j$ of the j^{th}atom can be written as [Condon and Shortley, 1951]

$$\begin{aligned}
\hat{\mathbf{M}}_j &= \mu_F \hat{\mathbf{F}}_j && (2.51)\\
\mu_F &\simeq g_J \left[\frac{F\left(F+1\right) + J\left(J+1\right) - I\left(I+1\right)}{2F\left(F+1\right)}\right], && (2.52)
\end{aligned}$$

where $\hat{\mathbf{J}}$ is the sum of the electronic orbital $\hat{\mathbf{L}}$ and spin $\hat{\mathbf{S}}$ angular momenta (i.e., $\hat{\mathbf{J}} = \hat{\mathbf{L}} + \hat{\mathbf{S}}$), and $\hat{\mathbf{F}}$ is the sum of $\hat{\mathbf{J}}$ and the nuclear spin $\hat{\mathbf{I}}$ (i.e., $\hat{\mathbf{F}} = \hat{\mathbf{J}} + \hat{\mathbf{I}}$). For the hyperfine levels of the ground state of the hydrogen atom, we have $F = 0$ and 1, $J = S = 1/2$, $I = 1/2$, and $\mu_F \simeq g_J/2$, whereas $g_J = g_e\mu_{\mathrm{B}}/\hbar$. In this equation, $g_e \simeq 2$ and μ_{B} is the Bohr magneton. The operator $\hat{\mathbf{F}}_j$ can also be written in terms of pseudospin operator $\hat{\mathbf{R}}_j$ as $\hat{\mathbf{F}}_j = \hbar\left(\hat{\mathbf{R}}_j + \hat{\mathbf{1}}/2\right)$, allowing us to write

$$\hat{\mathbf{M}}_j = \mu_{\mathrm{B}}\left(\hat{\mathbf{R}}_j + \frac{\hat{\mathbf{1}}}{2}\right). \tag{2.53}$$

For the $|F=0,m=0\rangle \longleftrightarrow |F=1,m=+1\rangle$ LCP transition we consider, the circular polarization state of radiation can be defined using the corresponding unit vectors [Grynberg et al., 2010]:

$$\mathbf{e}_L = -\frac{1}{\sqrt{2}}\left(\mathbf{e}_x + i\mathbf{e}_y\right) \tag{2.54}$$

$$\mathbf{e}_R = \frac{1}{\sqrt{2}}\left(\mathbf{e}_x - i\mathbf{e}_y\right), \tag{2.55}$$

which with $\mathbf{e}_3$ can be used to write the pseudospin operator as

$$\hat{\mathbf{R}}_j = \frac{1}{\sqrt{2}}\left(-\hat{R}_j^- \mathbf{e}_L + \hat{R}_j^+ \mathbf{e}_R\right) + \hat{R}_{j3}\mathbf{e}_3. \tag{2.56}$$

In a HI gas, the LCP magnetic component of the radiation propagating along the $\mathbf{k}$ direction interacts with the magnetic dipole of a hydrogen atom, resulting in a transition between the two hyperfine levels. The corresponding magnetic field operator can be expressed as

$$\hat{\mathbf{B}}_L(\mathbf{r},t) = \sum_{\mathbf{k}}\left[\hat{B}^+_{L\mathbf{k}}(\mathbf{r})e^{-i\omega_k t}\mathbf{e}_L + \hat{B}^-_{L\mathbf{k}}(\mathbf{r})e^{i\omega_k t}\mathbf{e}_L^*\right], \tag{2.57}$$

where

$$\hat{B}^+_{L\mathbf{k}}(\mathbf{r}) = \frac{1}{c}\sqrt{\frac{\hbar\omega_k}{2\epsilon_0 V}}\hat{a}_{L\mathbf{k}}e^{i\mathbf{k}\cdot\mathbf{r}} \tag{2.58}$$

$$= \left(\hat{B}^-_{L\mathbf{k}}\right)^\dagger, \tag{2.59}$$

and V is the arbitrary volume of quantization. In Equations (2.58) and (2.59), $a_{L\mathbf{k}}$ and $a^\dagger_{L\mathbf{k}}$ are, respectively, the LCP second quantization field annihilation and creation operators, and they obey the following commutation relation:

$$\left[\hat{a}_{L\mathbf{k}}, \hat{a}^\dagger_{L\mathbf{k}'}\right] = \hat{1}\delta_{\mathbf{k}\mathbf{k}'}. \tag{2.60}$$

As a result, one can express the magnetic dipole interaction term in Equation (2.50) for transitions involving only LCP photons as

$$\hat{V}_{\mathrm{MD}} = -\mu_{\mathrm{B}} \sum_{j=1}^{N} \hat{\mathbf{R}}_j \cdot \hat{\mathbf{B}}_L(\mathbf{r}_j) \tag{2.61}$$

$$= \frac{\mu_{\mathrm{B}}}{\sqrt{2}c} \sum_{j=1}^{N} \sum_{\mathbf{k}} \sqrt{\frac{\hbar\omega_k}{2\epsilon_0 V}} \left(\hat{R}_j^+ \hat{a}_{L\mathbf{k}} e^{i\mathbf{k}\cdot\mathbf{r}_j} + \hat{R}_j^- \hat{a}_{L\mathbf{k}}^\dagger e^{-i\mathbf{k}\cdot\mathbf{r}_j} \right), \tag{2.62}$$

using $\hat{\mathbf{R}} \cdot \mathbf{e}_L = -\hat{R}^+/\sqrt{2}$ and $\hat{\mathbf{R}} \cdot \mathbf{e}_L^* = -\hat{R}^-/\sqrt{2}$. It will also prove useful to write Equation (2.62) in the following form:

$$\hat{V}_{\mathrm{MD}} = -\int_V \hat{\boldsymbol{\mathcal{M}}}(\mathbf{r}) \cdot \hat{\mathbf{B}}_L(\mathbf{r}) d^3r, \tag{2.63}$$

which allows a definition of the transverse macroscopic magnetization operator $\hat{\boldsymbol{\mathcal{M}}}(\mathbf{r})$ in terms of the raising and lowering density operators $\hat{R}^+$ and $\hat{R}^-$ as follows:

$$\hat{\boldsymbol{\mathcal{M}}}(\mathbf{r}) = -\frac{\mu_B}{\sqrt{2}} \left[\hat{R}^-(\mathbf{r})\, \mathbf{e}_L + \hat{R}^+(\mathbf{r})\, \mathbf{e}_L^* \right] \tag{2.64}$$

$$\equiv \hat{\boldsymbol{\mathcal{M}}}^+(\mathbf{r}) + \hat{\boldsymbol{\mathcal{M}}}^-(\mathbf{r}). \tag{2.65}$$

Neglecting inhomogeneous broadening effects (i.e., we omit $\hat{H}_0$ and set $\omega_j = \omega_0$) and inserting Equation (2.62) in Equation (2.42), the Hamiltonian of the HI-sample system interacting with the 21 cm line via the $(F, m_F : 0, 0 \longleftrightarrow 1, +1)$ transition becomes

$$\hat{H} = \hbar\omega_0 \sum_{j=1}^{N} \left(\hat{R}_{j3} + \frac{\hat{1}}{2} \right) + \hat{H}_{\mathrm{rad}} + \frac{\mu_B}{\sqrt{2}c} \sum_{\mathbf{k}} \sqrt{\frac{\hbar\omega_{\mathbf{k}}}{2\epsilon_0 V}} \sum_{j=1}^{N} \left(\hat{R}_j^+ \hat{a}_{L\mathbf{k}} e^{i\mathbf{k}\cdot\mathbf{r}_j} + \hat{R}_j^- \hat{a}_{L\mathbf{k}}^\dagger e^{-i\mathbf{k}\cdot\mathbf{r}_j} \right). \tag{2.66}$$

The radiation Hamiltonian term $\hat{H}_{\mathrm{rad}}$ can be expressed in terms of the second quantized operators $\hat{a}_{L\mathbf{k}}$ and $\hat{a}_{L\mathbf{k}}^\dagger$, and $\hat{a}_{R\mathbf{k}}$ and $\hat{a}_{R\mathbf{k}}^\dagger$ associated with left and right circular-polarized radiation states, respectively, with

$$\hat{H}_{\mathrm{rad}} = \hbar\omega \sum_{\mathbf{k}} \left[\left(\hat{a}_{L\mathbf{k}}^\dagger \hat{a}_{L\mathbf{k}} + \frac{\hat{1}}{2} \right) + \left(\hat{a}_{R\mathbf{k}}^\dagger \hat{a}_{R\mathbf{k}} + \frac{\hat{1}}{2} \right) \right]. \tag{2.67}$$

As discussed in the literature [Gross and Haroche, 1982, Benedict et al., 1996], the evolution of the atomic system can be calculated using the Heisenberg equation of motion for the operator $\hat{X}$ in a system described by the Hamiltonian $\hat{H}$ with

$$\frac{d\hat{X}}{dt} = \frac{1}{i\hbar}[\hat{X}, \hat{H}]. \tag{2.68}$$

One can then readily find the following equations of motions for $\hat{R}^+$, $\hat{R}^-$, and $\hat{R}_3$:

$$\begin{aligned}
\frac{d\hat{R}^+}{dt} &= i\omega_0\hat{R}^+ - \frac{i\sqrt{2}\mu_B}{\hbar}\hat{R}_3\hat{B}_L^- && (2.69)\\
\frac{d\hat{R}^-}{dt} &= -i\omega_0\hat{R}^- + \frac{i\sqrt{2}\mu_B}{\hbar}\hat{R}_3\hat{B}_L^+ && (2.70)\\
\frac{d\hat{R}_3}{dt} &= -\frac{i\mu_B}{\sqrt{2}\hbar}\left(\hat{R}^+\hat{B}_L^+ - \hat{R}^-\hat{B}_L^-\right), && (2.71)
\end{aligned}$$

where, for simplicity, we now set $\hat{B}_L^{\pm}$ for the value of the LCP component of the magnetic field averaged over the positions of the atoms. In a similar way, we can write the following equations of motion for the raising and lowering magnetization operators $\hat{\boldsymbol{\mathcal{M}}}^+(\mathbf{r})$ and $\hat{\boldsymbol{\mathcal{M}}}^-(\mathbf{r})$ using Equation (2.64) as

$$\begin{aligned}
\frac{d\hat{\boldsymbol{\mathcal{M}}}^+}{dt} &= -i\omega_0\hat{\boldsymbol{\mathcal{M}}}^+ - \frac{i\mu_{\mathrm{B}}^2}{\hbar}\left(\mathbf{e}_L\cdot\hat{\mathbf{B}}_L^+\right)\hat{R}_3\mathbf{e}_L && (2.72)\\
\frac{d\hat{\boldsymbol{\mathcal{M}}}^-}{dt} &= i\omega_0\hat{\boldsymbol{\mathcal{M}}}^- + \frac{i\mu_{\mathrm{B}}^2}{\hbar}\left(\mathbf{e}_L^*\cdot\hat{\mathbf{B}}_L^-\right)\hat{R}_3\mathbf{e}_L^*. && (2.73)
\end{aligned}$$

It is also useful to define the operator $\hat{\mathbb{N}}$

$$\begin{aligned}
\hat{\mathbb{N}} &= 2\hat{R}_3 && (2.74)\\
&= 2\sum_{j=1}^{N}\hat{R}_{3j}\delta(\mathbf{r}-\mathbf{r}_j), && (2.75)
\end{aligned}$$

which can be interpreted as a population inversion density operator considering that $\hat{R}_{3j}$ has eigenvalues of $\pm 1/2$ and the eigenvalue of $\hat{R}_3 = \sum\hat{R}_{3j}$ is equal to half of the population difference between the excited level $F = 1$, $m_F = 1$ and the ground level $F = 0$, $m_F = 0$ at time t. Using Equation (2.75) one can show that Equations (2.71)-(2.73) can be rewritten as

$$\frac{d\hat{\mathbb{N}}}{dt} = \frac{2i}{\hbar}\left(\hat{\boldsymbol{\mathcal{M}}}^+\cdot\hat{\mathbf{B}}_L^+ - \hat{\boldsymbol{\mathcal{M}}}^-\cdot\hat{\mathbf{B}}_L^-\right) \tag{2.76}$$

$$\frac{d\hat{\boldsymbol{\mathcal{M}}}^{+}}{dt} = -i\omega_0\hat{\boldsymbol{\mathcal{M}}}^{+} - i\gamma\left(\mathbf{e}_L\cdot\hat{\mathbf{B}}_L^{+}\right)\hat{\mathbb{N}}\mathbf{e}_L \tag{2.77}$$

$$\frac{d\hat{\boldsymbol{\mathcal{M}}}^{-}}{dt} = i\omega_0\hat{\boldsymbol{\mathcal{M}}}^{-} + i\gamma\left(\mathbf{e}_L^{*}\cdot\hat{\mathbf{B}}_L^{-}\right)\hat{\mathbb{N}}\mathbf{e}_L^{*}, \tag{2.78}$$

where $\gamma = \mu_{\mathrm{B}}^2/2\hbar$.

Furthermore, in the Heisenberg representation one can derive the equation

$$-\nabla^2\hat{\mathbf{B}}_L^{\pm} + \frac{1}{c^2}\frac{\partial^2\hat{\mathbf{B}}_L^{\pm}}{\partial t^2} = -\mu_0\nabla^2\hat{\boldsymbol{\mathcal{M}}}^{\pm} \tag{2.79}$$

for the evolution of the magnetic component of the radiation field when defining

$$\hat{B}_L^{\pm}(\mathbf{r},t) = \hat{B}_0^{\pm}(\mathbf{r},t)\,e^{\pm i(kz-\omega t)} \tag{2.80}$$

$$\hat{\mathcal{M}}^{\pm}(\mathbf{r},t) = \hat{\mathcal{M}}_0^{\pm}(\mathbf{r},t)\,e^{\pm i(kz-\omega t)}, \tag{2.81}$$

using the slowly varying envelope approximation (SVEA), where $\hat{B}_0^{\pm}$ and $\hat{\mathcal{M}}_0^{\pm}$ are slow-varying envelope operators multiplied by fast-oscillating exponential terms propagating in the positive z direction. Within the context of the SVEA, we assume that the $\hat{B}_0^{\pm}$ and $\hat{\mathcal{M}}_0^{\pm}$ significantly change over time-scales much longer than $1/\omega$ and length-scales much larger than $1/k$ [Gross and Haroche, 1982]. Upon applying the SVEA, Equation (2.79) is simplified to

$$\left(\frac{\partial}{\partial z} + \frac{1}{c}\frac{\partial}{\partial t}\right)\hat{B}_0^{\pm} \simeq \pm\frac{i\mu_0\omega}{2c}\hat{\mathcal{M}}_0^{\pm}. \tag{2.82}$$

In the derivation of Equation (2.82), we neglected any transverse effects on the radiation field and magnetization (i.e., $\partial B_0^{\pm}/\partial x \approx \partial B_0^{\pm}/\partial y \approx 0$ and $\partial\hat{\mathcal{M}}_0^{\pm}/\partial x \approx \partial\hat{\mathcal{M}}_0^{\pm}/\partial y \approx 0$), which should be included in numerical calculations for a true three-dimensional sample.

Using Equations (2.80) and (2.81), we can rewrite Equations (2.76), (2.77), and (2.78) at resonance, that is, when $\omega = \omega_0$, in the reduced form of

$$\frac{d\hat{\mathcal{M}}_0^{\pm}}{dt} = \mp i\gamma\hat{B}_0^{\pm}\hat{\mathbb{N}} \tag{2.83}$$

$$\frac{d\hat{\mathbb{N}}}{dt} = \frac{2i}{\hbar}\left(\hat{\mathcal{M}}_0^{-}\hat{B}_0^{+} - \hat{\mathcal{M}}_0^{+}\hat{B}_0^{-}\right). \tag{2.84}$$

Equations (2.82)-(2.84) are known as the Maxwell-Bloch equations and can be solved simultaneously to determine the time evolution of the radiation field, magnetization, and excitation state for an ideal sample.

2.A.2 Dephasing Effects and Pumping

The previous derivations for the ideal case must be augmented appropriately when dealing with more realistic conditions for the ISM, where dephasing and relaxation effects cannot be neglected and continuous pumping of the atomic system can take place. One can phenomenologically add the corresponding terms to the atomic equations as follows [Mandel, 2010]:

$$\frac{d\hat{\mathcal{M}}_0^+}{dt} = -i\gamma\hat{B}_0^+\hat{\mathbb{N}} - \frac{1}{T_2}\hat{\mathcal{M}}_0^+ + \Lambda_{\mathrm{M}} \tag{2.85}$$

$$\frac{d\hat{\mathbb{N}}}{dt} = \frac{2i}{\hbar}\left(\hat{\mathcal{M}}_0^-\hat{B}_0^+ - \hat{\mathcal{M}}_0^+\hat{B}_0^-\right) - \frac{1}{T_1}\left(\hat{\mathbb{N}} - \mathbb{N}_{\mathrm{eq}}\right), \tag{2.86}$$

where T_1 and T_2 are the characteristic time-scales for, respectively, population decay and demagnetization, $\mathbb{N}_{\mathrm{eq}}$ is the "equilibrium" value for $\hat{\mathbb{N}}$ obtained in the absence of interaction with the coherent field $\hat{B}_L$, and Λ_{M} represents any source term of magnetization.

The one-dimensional magnetic field Equation (2.82) can also be adapted to the more realistic conditions by adding a correction term to account for the loss of radiation due to transverse effects and diffraction, which depend on the shape and symmetry of the sample. These are characterized by the Fresnel number

$$F_{\mathrm{n}} = \frac{A}{\lambda L}, \tag{2.87}$$

where A and L, respectively, stand for the cross section and length of the sample. For samples of cylindrical symmetry with a Fresnel number smaller than one, transverse effects of the field are negligible, whereas the diffraction of radiation along the propagation axis can play an important role. Gross and Haroche [1982] have shown that a damping term B_0^+/L_{diff} can be included in the field equation to take into account diffraction effects in samples with $F_{\mathrm{n}} \ll 1$. For such a sample, Equation (2.82) can be approximately augmented to

$$\left(\frac{\partial}{\partial z} + \frac{1}{c}\frac{\partial}{\partial t}\right)\hat{B}_0^+(z,\tau) + \frac{1}{L_{\mathrm{diff}}}B_0^+(z,\tau) \simeq \frac{i\mu_0\omega}{2c}\hat{\mathcal{M}}_0^+, \tag{2.88}$$

where $L_{\text{diff}} \simeq F_{\text{n}} L/0.35$ [Gross and Haroche, 1982].

The atom-field Equations (2.85), (2.86), and (2.88) also form a Maxwell-Bloch system of equations and provide a more complete and realistic picture for the evolution of the system. This set of equations can be numerically solved for a given set of parameters T_1, T_2, $\mathbb{N}_{\text{eq}}$, and Λ_{M}.

2.B The Sine-Gordon Solution

The set of Equations (2.85), (2.86) and (2.88) can only be solved analytically for a few special cases [Mandel, 2010]. We first consider the ideal condition, where the dephasing/relaxation, diffraction, and pumping terms are neglected (i.e., $T_1 = T_2 = \infty$, $L_{\text{diff}} = \infty$, and $\Lambda_{\text{M}} = 0$). Effecting a change of variable from t to the retarded time $\tau = t - z/c$ yields

$$\left(\frac{\partial}{\partial z} + \frac{1}{c}\frac{\partial}{\partial t}\right) = \frac{\partial}{\partial z} \tag{2.89}$$

$$\frac{\partial}{\partial t} = \frac{\partial}{\partial \tau}, \tag{2.90}$$

which can be used to simplify the set of Maxwell-Bloch equations (2.82)-(2.84) to

$$\frac{\partial \hat{\mathcal{M}}_0^{\pm}}{\partial \tau} = \mp i\gamma \hat{B}_0^{\pm} \hat{\mathbb{N}} \tag{2.91}$$

$$\frac{\partial \hat{\mathbb{N}}}{\partial \tau} = \frac{2i}{\hbar}\left(\hat{\mathcal{M}}_0^{-}\hat{B}_0^{+} - \hat{\mathcal{M}}_0^{+}\hat{B}_0^{-}\right) \tag{2.92}$$

$$\frac{\partial \hat{B}_0^{\pm}(z,\tau)}{\partial z} \simeq \pm\frac{i\mu_0\omega}{2c}\hat{\mathcal{M}}_0^{\pm}. \tag{2.93}$$

The form of Equations (2.91) and (2.92) implies that $\left|\hat{\boldsymbol{\mathcal{M}}}^{+}\right|^2 + \left|\hat{\boldsymbol{\mathcal{M}}}^{-}\right|^2 + (\mu_{\text{B}}^2/4)\left|\hat{\mathbb{N}}\right|^2$ is a conserved quantity and allows us to redefine $\hat{\mathcal{M}}_0^{\pm}$ and $\mathbb{N}$ as

$$\hat{\mathcal{M}}_0^{+} = \frac{\mu_{\text{B}} N}{2\sqrt{2}V}\sin(\theta) \tag{2.94}$$

$$\hat{\mathbb{N}} = \frac{N}{V}\cos(\theta), \tag{2.95}$$

where N is the number of inverted atoms in the sample at $\tau = 0$ and θ is the so-called Bloch angle.

Taking these solutions into account, at resonance Equations (2.91) and (2.93) are transformed to

$$\hat{B}_0^+ = \frac{i\mu_{\rm B}}{2\sqrt{2}\gamma}\frac{\partial\theta}{\partial\tau} \tag{2.96}$$

$$\frac{\partial\hat{B}_0^+}{\partial z} = \frac{i\mu_0\omega\mu_{\rm B}N}{4\sqrt{2}cV}\sin(\theta) \tag{2.97}$$

in the retarded time frame. Taking the spatial derivative of Equation (2.96) we can write

$$\frac{\partial\hat{B}_0^+}{\partial z} = \frac{i\mu_{\rm B}}{2\sqrt{2}\gamma}\frac{\partial^2\theta}{\partial z\partial\tau}, \tag{2.98}$$

which when compared to Equation (2.97) yields the following nonlinear equation

$$\frac{\partial^2\theta}{\partial z\partial\tau} = \frac{\mu_0\mu_{\rm B}^2\omega N}{4\hbar cV}\sin(\theta) \tag{2.99}$$

upon using $\gamma = \mu_{\rm B}^2/2\hbar$. This equation is further transformed with the introduction of a new dimensionless variable [Gross and Haroche, 1982]

$$q = 2\sqrt{\frac{z\tau}{LT_{\rm R}}}, \tag{2.100}$$

to

$$\frac{d^2\theta}{dq^2} + \frac{1}{q}\frac{d\theta}{dq} = \sin(\theta), \tag{2.101}$$

with $T_{\rm R}$ the characteristic time for superradiance given by Equation (2.24). Equation (2.101) is the so-called Sine-Gordon equation [Gross and Haroche, 1982]. This equation can be numerically solved and the corresponding solution for θ substituted back into Equation (2.96) to determine the field amplitude $\hat{B}_0^+$ emerging from the sample (at $z = L$) as a function of the retarded time τ. Knowing $\hat{B}_0^+(L,\tau)$, the output radiation intensity I is given by

$$I = \frac{c}{2\mu_0}\left|\hat{B}_0^+\right|^2. \tag{2.102}$$

A more realistic case where dephasing/relaxation is included with a single time-scale (i.e., $T' = T_1 = T_2 \neq \infty$, $L_{\rm diff} = \infty$, and $\Lambda_{\rm M} = \mathbb{N}_{\rm eq} = 0$) can be dealt with in a similar manner. We then have the corresponding definitions for Equations (2.94) and (2.95)

$$\hat{\mathcal{M}}_0^+ = \frac{\mu_{\rm B} N}{2\sqrt{2}V} \sin(\theta)\, e^{-\tau/T'} \tag{2.103}$$

$$\hat{\mathbb{N}} = \frac{N}{V} \cos(\theta)\, e^{-\tau/T'}, \tag{2.104}$$

which also lead to Equation (2.96) for $\hat{B}_0^+$. Performing a spatial derivative on Equation (2.96) yields

$$\frac{\partial^2 \theta}{\partial z \partial \tau} = \frac{\mu_0 \mu_{\rm B}^2 \omega N}{4\hbar c V} \sin(\theta)\, e^{-\tau/T'}. \tag{2.105}$$

A comparison of Equation (2.105) with (2.99) shows that the presence of dephasing implies a source term containing a decaying exponential. This exponential factor can be removed from this equation through the following change of variable:

$$\tau \longrightarrow \tau' = T' \left(1 - e^{-\tau/T'}\right), \tag{2.106}$$

which allows us to transform Equation (2.105) to the Sine-Gordon equation (i.e., Equation (2.101)) by redefining the dimensionless parameter q with the following:

$$q = 2\sqrt{\frac{z\tau'}{LT_{\rm R}}}. \tag{2.107}$$

Bibliography

N. P. Abel, G. J. Ferland, C. R. ODell, G. Shaw, and T. H. Troland. Physical conditions in Orions Veil. II. a multicomponent study of the line of sight toward the trapezium. *The Astrophysical Journal*, 644(1):344, 2006.

A. V. Andreev, V. I. Emel'yanov, and Y. A. Il'inskiĭ. Collective spontaneous emission (Dicke superradiance). *Soviet Physics Uspekhi*, 23(8):493, 1980.

M. G. Benedict, A. M. Ermolaev, V. A. Malyshev, I. V. Sokolov, and E. D. Trifonov. *Superradiance Multiatomic Coherent Emission*. Bristol: IOP Publishing Ltd, 1996.

R. Bonifacio and L. A. Lugiato. Cooperative radiation processes in two-level systems: Superfluorescence. *Physical Review A*, 11(5):1507, 1975.

N. W. Carlson, D. J. Jackson, A. L. Schawlow, M. Gross, and S. Haroche. Superradiance triggering spectroscopy. *Optics Communications*, 32(2):350–354, 1980.

E. U. Condon and G. H. Shortley. *The theory of atomic spectra*. Cambridge University Press, 1951.

R. M. Crutcher. Magnetic fields in molecular clouds. *Annual Review of Astronomy and Astrophysics*, 50:29–63, 2012.

R. H. Dicke. The effect of collisions upon the Doppler width of spectral lines. *Physical Review*, 89(2):472, 1953.

R. H. Dicke. Coherence in spontaneous radiation processes. *Physical Review*, 93(1):99, 1954.

R. H. Dicke. The coherence brightened laser. *Quantum Electronics*, 1:35–54, 1964.

M. Dijkstra and A. Loeb. Requirements for cosmological 21-cm masers. *New Astronomy*, 13 (6):395–404, 2008.

B. T. Draine. *Physics of the interstellar and intergalactic medium*. Princeton, NJ: Princeton University Press, 2012.

D. Emerson. *Interpreting Astronomical Spectra*. New York: Wiley, 1996.

G. B. Field. Excitation of the hydrogen 21-cm line. *Proceedings of the IRE*, 46(1):240–250, 1958.

V. L. Fish. Masers and star formation. *Proceedings of the International Astronomical Union*, 3(S242):71–80, 2007.

H. M. Gibbs, Q. H. F. Vrehen, and H. M. J. Hikspoors. Single-pulse superfluorescence in cesium. *Physical Review Letters*, 39(9):547, 1977.

P. F. Goldsmith and W. D. Langer. Population diagram analysis of molecular line emission. *The Astrophysical Journal*, 517(1):209, 1999.

C. Greiner, B. Boggs, and T. W. Mossberg. Superradiant emission dynamics of an optically thin material sample in a short-decay-time optical cavity. *Physical Review Letters*, 85(18): 3793, 2000.

M. Gross and S. Haroche. Superradiance: An essay on the theory of collective spontaneous emission. *Physics Reports*, 93:301–396, December 1982.

M. Gross, C. Fabre, P. Pillet, and S. Haroche. Observation of near-infrared dicke superradiance on cascading transitions in atomic sodium. *Physical Review Letters*, 36(17):1035, 1976.

M. Gross, P. Goy, C. Fabre, S. Haroche, and J. M. Raimond. Maser oscillation and microwave superradiance in small systems of Rydberg atoms. *Physical Review Letters*, 43(5):343, 1979.

G. Grynberg, A. Aspect, and C. Fabre. *Introduction to quantum optics: from the semi-classical approach to quantized light*. Cambridge University Press, 2010.

J. A. Irwin. *Decoding the Cosmos*. Chichester: Wiley, 2007.

J. D. Jackson. *Classical electrodynamics*. New York: Wiley, 1999.

S. Kida, K. Niinuma, S. Suzuki, T. Tanaka, R. Nakanura, K. Takefuji, N. Matsumura, M. Kuniyoshi, and T. Daishido. Two strong radio bursts at high and medium Galactic latitude. *New Astronomy*, 13(7):519–525, 2008.

J. C. MacGillivray and M. S. Feld. Theory of superradiance in an extended, optically thick medium. *Physical Review A*, 14(3):1169, 1976.

J. C. MacGillivray and M. S. Feld. Limits of superradiance as a process for achieving short pulses of high energy. *Physical Review A*, 23(3):1334, 1981.

P. Mandel. *Nonlinear optics*. Wiley-VCH, 2010.

J. Meziane, S. Oullemine, K. Amezian, and E. Boursey. Competition between collective and stimulated effects in 130Te2 superfluorescence. *Chemical Physics Letters*, 363(5):573–578, 2002.

L. Moi, P. Goy, M. Gross, J. M. Raimond, C. Fabre, and S. Haroche. Rydberg-atom masers. I. a theoretical and experimental study of super-radiant systems in the millimeter-wave domain. *Physical Review A*, 27(4):2043, 1983.

H. M. Nussenzveig. *Introduction to Quantum Optics*. New York: Gordon and Breach, 1973.

I. E. Protsenko. Superradiance of trapped atoms. *Journal of Russian Laser Research*, 27(5): 414–436, 2006.

F. Rajabi and M. Houde. Explaining Recurring Maser Flares in the ISM Through Large-scale Entangled Quantum Mechanical States. *Science Advances, Submitted*, 2016.

Fereshteh Rajabi and Martin Houde. Dickes superradiance in astrophysics. II. the OH 1612 MHz line. *The Astrophysical Journal*, 828(1):57, 2016.

A. T. Rosenberger and T. A. DeTemple. Far-infrared superradiance in methyl fluoride. *Physical Review A*, 24(2):868, 1981.

A. P. Sarma. Polarization of class I methanol (CH3OH) masers. *Proceedings of the International Astronomical Union*, 8(S287):41–48, 2012.

I. S. Shklovskii. Possible maser effect in clouds of interstellar hydrogen in the Galactic corona. *Soviet Astronomy*, 11:240, 1967.

N. Skribanowitz, I. P. Herman, J. C. MacGillivray, and M. S. Feld. Observation of Dicke superradiance in optically pumped HF gas. *Physical Review Letters*, 30(8):309, 1973.

S. H. Storer and D. W. Sciama. Is interstellar hydrogen capable of maser action at 21 centimetres? *Nature*, 217:1237, 1968.

D. Thornton, B. Stappers, M. Bailes, B. Barsdell, S. Bates, N. D. R. Bhat, M. Burgay, S. Burke-Spolaor, D. J. Champion, P. Coster, et al. A population of fast radio bursts at cosmological distances. *Science*, 341(6141):53–56, 2013.

C. H. Townes and A. L. Schawlow. *Microwave spectroscopy*. New York: McGraw Hill, 1955.

W. H. T. Vlemmings. Maser polarization and magnetic fields. *Proceedings of the International Astronomical Union*, 8(S287):31–40, 2012.

W. D. Watson. Magnetic fields and the polarization of astrophysical maser radiation: a review. *arXiv preprint arXiv:0811.1292*, 2008.

J. P. Wittke and R. H. Dicke. Redetermination of the hyperfine splitting in the ground state of atomic hydrogen. *Physical Review*, 103(3):620, 1956.

S. A. Wouthuysen. On the excitation mechanism of the 21-cm (radio-frequency) interstellar hydrogen emission line. *The Astronomical Journal*, 57:31–32, 1952.

H. Xia, A. .A. Svidzinsky, L. Yuan, C. Lu, S. Suckewer, and M. O. Scully. Observing superradiant decay of excited-state helium atoms inside helium plasma. *Physical review letters*, 109(9):093604, 2012.

B. Zygelman. Hyperfine level-changing collisions of hydrogen atoms and tomography of the dark age universe. *The Astrophysical Journal*, 622(2):1356, 2005.

Chapter 3

Dicke's Superradiance in Astrophysics. II – The OH 1612 MHz Line[1]

3.1 Introduction

The OH (hydroxyl) rotational transitions at nearly 18 cm were the first interstellar molecular lines detected in the radio range [Weinreb et al., 1963, Bertolotti, 2015]. The ground level of that molecule is split into two sub-levels known as Λ-doublets with $\pm\Lambda\hbar$ energies. Each component of the Λ-doublets is also split into two hyperfine levels labelled $F = 1$ and $F = 2$, as shown in Figure 3.1. The transitions that connect sub-levels with the same F-values are called the *main lines*, whereas the transitions between sub-levels of different F-value are called the *satellite lines* [Stahler and Palla, 2008]. The four transitions including the two main lines at 1665 MHz and 1667 MHz and the two satellite lines at 1612 MHz and 1720 MHz compose the group of 18 cm wavelength lines. In optically thin regions under conditions of local thermodynamic equilibrium (LTE), the expected intensity ratios are approximately 1:5:9:1 for the 1612 MHz, 1665 MHz, 1667 MHz and 1720 MHz lines, respectively [Elitzur, 1992]. However, in several observations different line ratios were measured [McGee et al.,

[1]Rajabi, F., & Houde, M. 2016, The Astrophysical Journal, 828, 57

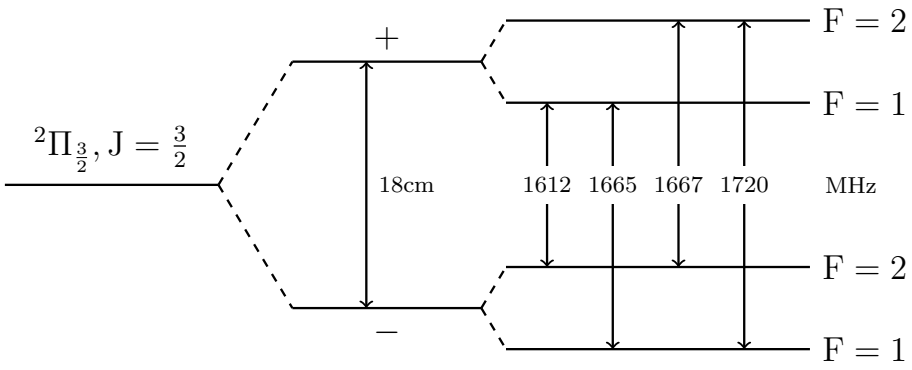

Figure 3.1: The schematic diagram of the ground rotational state of the OH molecule. The ground rotational level labelled by $^2\Pi_{3/2}$, $J = 3/2$ splits into $\Lambda-$doublet sub-levels shown as $\pm$ states. This splitting is due to the interaction between the rotational and electronic angular momenta of the molecule. Each $\Lambda-$doublet sub-level further splits into two hyperfine levels as a result of the interaction between the electron and nuclear spins of hydrogen atom. The four possible maser transitions are shown with their corresponding frequencies in MHz. Note that the hyperfine splitting is not to scale.

1965], and in some cases the intensity of a given line significantly exceeded that predicted using LTE [Weaver et al., 1965]. The strong anomalous line intensities were explained by postulating maser action for the corresponding transitions.

Maser action occurs when LTE conditions are violated and velocity coherence is achieved between a group of population-inverted molecules. In the presence of a pumping mechanism that can maintain a higher population in the excited level, the corresponding transition can exhibit the exceptionally high intensity typical of maser sources [Elitzur, 1992]. The aforementioned study of Weaver et al. [1965] reported the first detection of an OH maser, which was to be followed by several other detections in different regions of the interstellar medium (ISM). A few years later Turner [1970] suggested classifying OH maser sources into two classes: Type I and Type II, depending on their brightest detected line. In Type I, the main-line transitions, especially the one at 1665 MHz, are dominant. The sources in this class are usually detected in star-forming sites near H II regions. Type II sources are

further divided into Type IIa and Type IIb in which the brightest line corresponds to one of the satellite lines. Type IIa OH maser sources, which are usually detected in supernova remnants, are brightest at 1720 MHz, while in Type IIb the 1612 MHz line is dominant. These sources are often spatially associated with highly evolved stars undergoing rapid mass loss and enclosed in a circumstellar shell [Gray, 2012]. In addition, the first extragalactic OH maser was detected in 1982 by Baan et al. [1982] in Arp 220 (IC 4553) with a luminosity approximately 10^8 times greater than that of typical Galactic OH masers. This led to the term "megamaser." Since then several OH megamasers, and even gigamasers, have been detected [Darling and Giovanelli, 2002], usually in the nuclear region of luminous or ultra-luminous infrared galaxies [Lockett and Elitzur, 2008].

The existence of 18-cm OH masers confirms the possibility of inverting populations in the ground level Λ-doublets of this molecule in the ISM. Different pumping mechanisms are suggested for different types of Galactic and extragalactic masers. For instance, Type IIb maser sources near evolved stars are known to be pumped by the far-infrared radiation emitted from dust (Elitzur 1992, He 2005, Gray et al. 2005; see Section 3.2 for more details), while it is suggested that the pumping of OH Type I main-line masers is controlled by collisions with H_2 molecules in star-forming regions [Kylafis and Norman, 1990]. Maser action also requires line-of-sight velocity coherence, which can lead to an abnormally narrow line-width through amplification along the radiation path. For Galactic OH 18-cm lines the typical line width is ≤ 1 km/s [McBride et al., 2013].

Population inversion and velocity coherence are also required for the superradiance co-operative radiation process. In 1954, R. H. Dicke pointed out that a sample consisting of N excited atoms/molecules interacting with a common radiation field cannot always be considered as a collection of independent radiators [Dicke, 1954]. He showed that, under ideal conditions and after a time delay, the sample of atoms/molecules can radiate its stored energy at an enhanced rate $N\Gamma$; N times faster than the spontaneous emission rate Γ of a single atom/molecule. As a result, the intensity of the output radiation $I_{\rm SR}$ scales as the square of the number of inverted atoms/molecules N, unlike the linear dependency of the radiation intensity from the corresponding non-coherent system $I_{\rm nc}$ (Rajabi and Houde 2016; hereafter Paper I).

In the ISM, it is usually assumed that atoms/molecules interact with the radiation field independently and the intensity of the radiation becomes a linear function of the atomic/molecular density (if the line is optically thin). But in the case of the OH 18-cm line, for which the detection of several maser sources verifies the possibility of achieving population inversion and velocity coherence in some regions, this assumption may fail and it becomes important to examine the possibility of superradiance and coherent interactions. Accordingly, in this paper we follow on the superradiance analysis performed in Paper I for the HI 21 cm (magnetic dipole) transition with a similar study for the OH 18 cm (electric dipole) line. In order to do so, we first discuss the necessary conditions for superradiance in Section 3.2, and narrow down our focus to the 1612 MHz line interacting with OH molecules in the outer regions of the circumstellar envelope (CSE) of highly evolved stars. In Section 3.3, we investigate the likelihood that these conditions can be met in these regions using the Heisenberg approach, with a method of analysis that is an electric dipolar version of the magnetic dipole study found in Paper I and is similar to earlier analyses found in the physics literature [Gross and Haroche, 1982, Benedict et al., 1996]. In Section 3.4 we discuss our numerical results on the characteristics of a potential OH 1612 MHz coherent system, with an application to previous observations performed on the U Orionis Mira star [Jewell et al., 1981] and the IRAS18276-1431 pre-planetary nebula [Wolak et al., 2014]. We end with a short conclusion in Section 3.5.

3.2 Requirements for Superradiance

In this section we provide a brief summary of the requirements needed for superradiance, but a more detailed discussion will be found in Section 2 of Paper I. Our discussion applies equally well to atoms or molecules, however, we will focus on molecular superradiance since OH is the subject of our analysis.

When a group of N excited molecules are placed within a volume V much smaller than λ^3, the cube of the wavelength of the radiation λ interacting with the molecules, the radiation by one molecule is seen to be in phase by the other molecules. As a result, the radiation from the different molecules interferes constructively and a strong directional pulse emerges

from the sample [Dicke, 1954]. This process can also be described from the molecular point of view. In a small-sample (i.e., defined for $V \ll \lambda^3$) the intermolecular distance r is much smaller than λ and, for such small intermolecular distances, the interaction between the molecular dipoles and the radiation field is symmetrical throughout the sample. As a result, after a delay time $t_{\rm D}$ the molecular dipoles lock to a common phase and act like a single macroscopic dipole radiating a superradiant intensity $I_{\rm SR} = NI_{\rm nc}$, where $I_{\rm nc}$ is the intensity of a fully non-coherent system [Dicke, 1954, Gross and Haroche, 1982, Benedict et al., 1996].

The phenomenon can be extended to a large-sample, defined as N molecules distributed over a volume $V \gg \lambda^3$, with inter-molecular spacings potentially larger than λ. In a large-sample, the phase of the radiation varies from place to place as a result of propagation. This will lead to a non-uniform spatial evolution of the molecules, and can result in a weaker coherent behavior as compared to that of a small-sample. However, the higher number of molecules partaking in coherent interactions in a large-sample can make up for this, resulting in an intense output superradiant pulse with $I_{\rm SR} = NfI_{\rm nc}$, where the Nf factor determines the enhancement of the radiation intensity in comparison to $I_{\rm nc}$ and the efficiency of the common phase-locking process is reflected in $f\,(< 1)$ alone. Unlike for a small-sample, the phase-matching condition in a large-sample can only be met in some particular directions, and the fact that the phase-locking factor f is always smaller than unity implies a weakened superradiance. It is found that after a delay time $\tau_{\rm D}$, a first burst of superradiance emerges the sample followed by a number of weaker bursts, the so-called ringing effect (see Section 3.3 below, and Sections 3 and 4 in Paper I). The ringing effect is associated with the re-absorption and re-emission of radiation through the end-fire (i.e., the observer-facing cross-section of the superradiant sample) of a large-sample interacting with the incoming radiation originating from other parts farther away in the sample.

Any mechanism that non-coherently reduces the excited level population (e.g., collisional relaxation) or disturbs the phase-locking process can diminish and even terminate superradiance. It is therefore necessary that the time-scale of dephasing/relaxation effects be longer than $\tau_{\rm D}$ in a large-sample (or $t_{\rm D}$ in a small-sample) to allow for the development of any coherent behavior. This also explains why velocity coherence is an essential condition for superradiance. In the absence of velocity coherence, random thermal motions in a gas

results in Doppler line broadening that corresponds to a very short dephasing time-scale (i.e., $T_{\rm therm} \ll \tau_{\rm D}$), and renders this phenomenon the most likely cause of dephasing in a sample. For this reason, it is not expected that superradiance could arise in a thermally relaxed gas. Our study of superradiance is better suited to regions of the ISM where thermal equilibrium has not been reached (e.g., shocks; see Paper I). However, this does not imply that Doppler broadening is not present in a velocity-coherent region, but it is expected to be less constraining than in a thermally relaxed environment.

For any region in the ISM, inelastic collisions with ions, electrons, hydrogen atoms and molecules, or dust grains can further change the internal state of an OH molecule, and if the associated time-scale is smaller than $\tau_{\rm D}$, coherent behavior and superradiance can be suppressed. Although they do not change the internal state of a molecule, elastic collisions can also interrupt the coherent phase-locking process and weaken superradiance. This is because during an elastic collision the spacings between energy levels for the colliding counterparts change as a result of short-range interaction forces. After a number of such collisions each acting like a random perturbation, the molecule can lose coherence with the interacting radiation field [Wittke and Dicke, 1956]. Elastic collisions are normally more frequent than inelastic collisions, and the mean time between elastic collisions usually sets the time-scale of collisional dephasing/relaxation $T_{\rm c}$ and the corresponding condition $\tau_{\rm D} < T_{\rm c}$ is required to allow the build-up of coherent interactions.

The above discussion also implies that coherent interactions cannot be developed in a collisionally pumped OH sample since that would require that the pumping time-scale $T_{\rm P} = T_{\rm c} < \tau_{\rm D}$, which contradicts the necessary condition $T_{\rm c} > \tau_{\rm D}$ for superradiance (see Paper I). Thus, for our present study of superradiance we will only focus on OH samples that are believed to be inverted through radiative processes. The studies of pumping mechanism of OH masers show that the 1612 MHz masers associated with evolved stars are pumped by far-infrared photons at 35 and 53 μm [Litvak, 1969, Jewell et al., 1979, Gray, 2012, Elitzur, 1992]. These photons are emitted from dust shells formed by mass losses from the central star. The radiative pumping model for 1612 MHz masers near evolved stars is corroborated by the observation of correlated variations in the intensities of the star and corresponding masers [Harvey et al., 1974, Jewell et al., 1979]. While recent studies by He [2005] and

Lockett and Elitzur [2008] suggest that OH megamasers, which emit primarily at 1667 MHz and 1665 MHz, are also pumped by far-infrared radiation (more precisely 53 μm radiation from dust), the determination of the exact pumping mechanism of main-line masers still requires more studies and collisional processes are not generally ruled out from the pumping scenarios [Gray, 2012]. Hence, in this paper we limit our investigation to the possibility of superradiance for the 1612 MHz line interacting with OH molecules in the circumstellar envelopes of late-type stars.

3.2.1 OH Samples Near Evolved Stars

One of the final stages in the evolution of a low- to intermediate-mass star (i.e., stars with masses of about 1 $M_\odot$ to 8 $M_\odot$) is the asymptotic giant branch (AGB) phase. In that stage, the star, which is composed of an oxygen/carbon core enclosed within layers of hydrogen and helium, becomes variable and can produce shock waves. Shock waves initiate the mass-loss process from the photosphere of the star to cooler regions where the gas particles can clump into dust grains, which interact with the radiation from the star over a broad continuum. Through these interactions the radially outgoing photons transfer their momentum to dust grains driving them outward. This also results in an outflow of the gas particles that are coupled to dust grains through collisions [Lamers and Cassinelli, 1999, Gray, 2012]. As outflowing waves move further from the star, they become cooler and denser and form the CSE. The CSE of an evolved star can harbor masers of different types depending on its composition. OH masers are usually found in the CSE of oxygen-rich (or M-type) stars. Examples of such stars are Mira variables, long-period M-type stars with periods of 100-500 days [Karttunen et al., 2007], which are known sources of 1612 MHz OH maser emission. OH-IR stars are another group of long-period variables (LPV) that were originally detected through their 1612 MHz OH maser emission and the infrared radiation emanating from their CSE. Miras are variable at both visible and infrared wavelengths, whereas the CSE of OH-IR stars absorbs starlight at visible wavelengths and re-emits it in the infrared. OH-IR stars are thought to lose mass at a rate of 10^{-8} $M_\odot$ yr^{-1} to 10^{-4} $M_\odot$ yr^{-1} forming larger CSEs than Miras, which have a lower mass-loss rate. The CSEs of these evolved stars are theoretically divided into three zones [Gray, 1999], of which the inner and outer zones are

relevant to our study. In the outermost zone, where the CSE is optically thin, UV light from the interstellar medium dissociates H_2O molecules into OH. In the inner zones, the radiation from the central star is absorbed by dust grains and is re-emitted in the infrared. It was initially suggested by Elitzur et al. [1976] that the 35- and 53-μm infrared photons emitted from dust pump the 1612 MHz OH masers in the outer regions of the CSE of evolved stars. The pumping scheme proposed by Elitzur et al. [1976] was modified by Gray et al. [2005], and their detailed analysis of collisional and radiative couplings of OH molecules in the expanding CSE of OH-IR stars indicated that the strongest pumping route uses 53-μm photons.

The CSE of evolved stars expands radially and reaches a constant terminal velocity $v_\infty \sim 10$ km s^{-1} to 20 km s^{-1} in its outer regions [Gray, 2012]. At distances about $r \gtrsim 10^{16}$ cm from the central star, velocity coherence is achieved among OH molecules moving with the well-defined terminal velocity in the radial or tangential directions relative to the OH shell [Draine, 2011]. This velocity coherence can be maintained over the so-called Sobolev length, which is typically on the order of $10^{14} - 10^{16}$ cm for LPV evolved stars (see Section 3.4.1 below). This, therefore, may allow the existence of relatively long OH samples, if inversion is achieved through infrared pumping from warm dust. In such samples coherent correlations may develop if the shortest non-coherent relaxation/dephasing time-scale is larger than $\tau_{\rm D}$.

Although our analysis is better adapted to regions where thermal equilibrium has not been reached, we will approximate the time-scale of relaxation/dephasing effects in the usual manner applicable to a thermally relaxed gas. We should, however, keep in mind that the time-scales calculated that way are likely to provide overestimates and should be considered as worst case scenarios, as far as superradiance is concerned. One of the main relaxation/dephasing mechanisms in the CSE of evolved stars is collision. We will therefore determine collision time-scales in OH samples given a temperature T and number density $n_{\rm H_2}$ of hydrogen molecules, which are expected to be the main collisional partners of OH in molecular gas shells [Gray, 2012]. These parameters depend on the mass-loss rate of the central star in a circumstellar envelope [Goldreich and Scoville, 1976]. For instance, at a mass-loss rate of $1 \times 10^{-5}\,{\rm M}_\odot\,{\rm yr}^{-1}$ the abundance of OH molecules is estimated to be approximately 10 cm^{-3}, while $n_{\rm H_2} \sim 10^6$ cm^{-3} at $r \approx 10^{16}$ cm based on the study of different

physical and chemical processes taking place in the CSEs of OH-IR stars [Gray et al., 2005]. Allowing for potentially lower mass-loss rates, we will consider the 10^4 cm^{-3} $\leq n_{\rm H_2} \leq 10^6$ cm^{-3} range in what follows.

The time-scale of OH$-$H$_2$ collisions can be determined with the knowledge of the collisional cross sections in these regions. The cross sections for inelastic OH$-$H$_2$ collisions at different temperatures are given in Offer et al. [1994], and the related time-scale is estimated to range from 10^5 sec to 10^7 sec for 10^6 cm^{-3} $\geq n_{\rm H_2} \geq 10^4$ cm^{-3}, respectively. For elastic OH$-$H$_2$ collisions the corresponding time-scale is given by

$$T_{\rm c} = \frac{1}{n_{\rm H_2}\sigma_{\rm g}\bar{v}}, \tag{3.1}$$

where $\sigma_{\rm g} \simeq 4 \times 10^{-16}\,{\rm cm}^2$ is the geometrical cross-sectional area of a hydrogen molecule and $\bar{v}$ is the mean relative velocity of OH molecules [Irwin, 2007, Souers, 1986]. For example, $\bar{v}$ is estimated to be ~ 1 km s^{-1} at $T \sim 100$ K. Inserting these values into Equation (3.1) gives 10^4 sec $\leq T_{\rm c} \leq 10^6$ sec for 10^6 cm^{-3} $\geq n_{\rm H_2} \geq 10^4$ cm^{-3}, respectively. As was already mentioned, elastic OH$-$H$_2$ collisions are found to be somewhat more frequent than their inelastic counterpart and thus set the time-scale of collisional dephasing $T_{\rm c}$.

Another important process that affects the population of OH energy levels in the CSE of evolved stars is the infrared radiative coupling of rotational levels. As was mentioned earlier, the warm dust in the CSE absorbs the radiation from the central star and re-emits it at mid- and far-infrared wavelengths. The different infrared couplings of the OH rotational levels have large transition dipoles leading to fast excitation/relaxation rates. It should be noted that these transition rates also depend on the opacity at the corresponding infrared wavelengths, which vary over the different zones of the CSE. Among the different infrared coupling routes some pump the 1612-MHz line while others deplete the population inversion and have a relaxation effect. The numerical studies conducted by Gray et al. [2005] show that these infrared couplings are responsible for the inverted OH zones, with a relaxation time-scale for the 1612-MHz line, including collisional and radiative couplings, on the order of $\sim 10^4$ sec for a mass loss rate of 10^{-5} M$_\odot$ yr^{-1}. Allowing for variations with different mass loss rates, we find that the radiative relaxation time-scales are comparable to those expected from collisions in these regions. For the sake of our discussion we will assume, for simplicity,

that the time-scale of OH$-$H$_2$ collisions sets the upper limit for the characteristic time-scales of superradiance in circumstellar OH samples, but we keep in mind that infrared radiative coupling may also be responsible for this. For the aforementioned range of H_2 densities, when assuming thermal equilibrium the delay time $\tau_{\rm D}$ and the characteristic time of superradiance $T_{\rm R}$ should not exceed 10^4 sec to 10^6 sec. Although these figures should be viewed as worst case scenarios (i.e., lower limits), they allow us to get a sense of the time-scales involved. As we will see later, these time-scales imply intensity variations that could last as long as several years.

3.3 Analytical Model

In this section we use the formalism developed in Gross and Haroche [1982] to describe the behavior of a superradiant system. Since, as will be seen in Section 3.4, the realization of superradiance small-sample is unlikely to take place in the CSEs of evolved stars for the collisional time-scales previously calculated (see Paper I), we focus our analysis on the case of a large-sample.

Taking into account the dephasing/relaxation effects, the behavior of a superradiant system can be expressed by a set of so-called Maxwell-Bloch equations within the framework of the slowly varying envelope approximation (SVEA)

$$\frac{\partial \hat{\mathbb{N}}}{\partial \tau} = \frac{i}{\hbar}\left(\hat{P}_0^+ \hat{E}_0^+ - \hat{E}_0^- \hat{P}_0^-\right) - \frac{\hat{\mathbb{N}}}{T_1} \tag{3.2}$$

$$\frac{\partial \hat{P}_0^+}{\partial \tau} = \frac{2id^2}{\hbar}\hat{E}_0^- \hat{\mathbb{N}} - \frac{\hat{P}_0^+}{T_2} \tag{3.3}$$

$$\frac{\partial \hat{E}_0^+}{\partial z} = \frac{i\omega}{2\epsilon_0 c}\hat{P}_0^-, \tag{3.4}$$

where T_1 is the (phenomenological) time-scale of non-coherent population relaxation (e.g., through inelastic collisions) and similarly T_2 for phase relaxation (e.g., through elastic collisions). These equations were derived within the context of the Heisenberg representation. The quantities $\hat{P}_0^{\pm}$ and $\hat{E}_0^{\pm}$ are the envelopes for the polarization $\hat{\mathbf{P}}^{\pm}$ and the electric field $\hat{\mathbf{E}}^{\pm}$ vectors, respectively, which are assumed to have the following form

$$\hat{\mathbf{P}}^{\pm}(z,\tau) = \hat{P}_0^{\pm}(z,\tau)\, e^{\pm i\omega\tau}\hat{\boldsymbol{\epsilon}}_{\mathrm{m}} \tag{3.5}$$

$$\hat{\mathbf{E}}^{\pm}(z,\tau) = \hat{E}_0^{\pm}(z,\tau)\, e^{\mp i\omega\tau}\hat{\boldsymbol{\epsilon}}_{\mathrm{m}}, \tag{3.6}$$

with $\hat{\boldsymbol{\epsilon}}_{\mathrm{m}}$ the unit vector indicating the orientation of the molecular electric dipole moment. The population inversion density is given by (twice) $\hat{\mathbb{N}}$, while d and ω are, respectively, the transition dipole matrix element and the angular frequency of the radiation field at resonance with the molecular transition. Equations (3.2) to (3.4) are derived using a two-level system model and describe the evolution of the matter-field system in the retarded-time frame τ ($= t - z/c$, where c is the speed of light). In the ISM, an OH sample interacting with the radiation along the line-of-sight can be modeled by a cylindrical large-sample along the z-axis. Although a one-dimensional field equation discards the loss of radiation due to diffraction or transverse effects, it is an approximation that reduces the number of variables and allows us to move the analysis forward while retaining the essential physics of the problem. Nonetheless, considerations of the sample's geometry, described by the Fresnel number $F = A/(\lambda L)$, with A and L the cross-section and length of the sample, respectively, will also enter our analysis.

Under the assumption that the different dephasing time-scales are similar (i.e., $T' \equiv T_1 = T_2$), the Maxwell-Bloch equations can be solved by effecting the following change of variables

$$\hat{\mathbb{N}} = \frac{N}{2V}\cos(\theta)\, e^{-\tau/T'} \tag{3.7}$$

$$\hat{P}_0^{+} = \frac{Nd}{2V}\sin(\theta)\, e^{-\tau/T'}, \tag{3.8}$$

where θ is the so-called Bloch angle and N is the number of inverted molecules at $\tau = 0$ in the sample volume V. Inserting Equations (3.7) and (3.8) into the system of Equations (3.2)-(3.4) yields

$$\hat{E}_0^{+} = \frac{i\hbar}{2d}\frac{\partial\theta}{\partial\tau} \tag{3.9}$$

$$\frac{d^2\theta}{dq^2} + \frac{1}{q}\frac{d\theta}{dq} = \sin(\theta), \tag{3.10}$$

with q

$$q = 2\sqrt{\frac{z\tau'}{LT_{\rm R}}}, \tag{3.11}$$

and $\tau' = T'\left(1 - e^{-\tau/T'}\right)$. The characteristic time-scale of superradiance $T_{\rm R}$ is given by

$$T_{\rm R} = \tau_{\rm sp}\frac{8\pi}{3n\lambda^2 L}, \tag{3.12}$$

where $\tau_{\rm sp}$ is the spontaneous decay time-scale of a single molecule and $n = N/V$ the density of inverted molecules in the sample [Gross and Haroche, 1982, Benedict et al., 1996]. Equation (3.10) is the so-called Sine-Gordon equation, which can be solved numerically to find solutions for $\theta\,(q)$ at the end-fire of the sample (i.e., at $z = L$). The solution for θ as a function τ can be used to evaluate $\hat{E}_0^+\,(z = L, \tau)$ from Equation (3.9), and then the intensity of radiation emerging from the sample with

$$I_{\rm SR} \;=\; \frac{c\epsilon_0}{2}\left|\hat{E}_0^+\right|^2, \tag{3.13}$$

where ϵ_0 is the permittivity of vacuum.

In Figure 3.2 we show three solutions for the radiation intensity from a cylindrical large-sample of OH molecules interacting with the 1612 MHz line, for the cases where $T' = 70\,T_{\rm R}$, $210\,T_{\rm R}$, and $700\,T_{\rm R}$. For these calculations we set the total number density of OH molecules to $n_{\rm OH} = 10\ {\rm cm}^{-3}$, the level of inversion $\eta = 0.01$, and $T_{\rm R} = 7$ days. The length of the sample L is set through Equation (3.12) for the given $T_{\rm R}$, and the Fresnel number is set to unity forcing the radius of the sample to $w = \sqrt{\lambda L/\pi}$. This value for the Fresnel number minimizes diffraction losses, which are not taken into account in our model [Gross and Haroche, 1982]. In the figure the radiation intensity axis is scaled to $NI_{\rm nc}$ and the retarded-time axis is normalized to $T_{\rm R}$. We can express the non-coherent intensity $I_{\rm nc}$ as

$$I_{\rm nc} = N\hbar\omega\left(\frac{1}{A\tau_{\rm sp}}\right)\left(\frac{\phi_{\rm D}}{4\pi}\right), \tag{3.14}$$

where $N\hbar\omega$ is the total energy initially stored in the OH sample, of which a fraction $\phi_{\rm D}/4\pi$ emerges from the end-fire of the sample through a cross-sectional area A over the spontaneous decay time-scale $\tau_{\rm sp}$. The superradiance beam solid-angle $\phi_{\rm D}$ is defined as

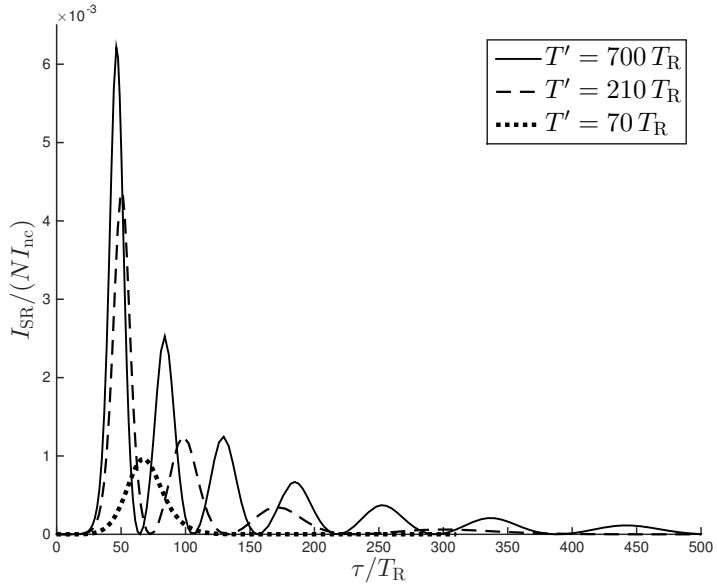

Figure 3.2: The OH cylindrical large-sample. The intensity axis, scaled to NI_{nc} , is plotted versus the retarded-time axis, normalized to the superradiance characteristic time-scale T_{R}. The length of the sample L is set through Equation (3.12) for a given T_{R}, and the Fresnel number is set to unity forcing the radius of the sample to $w = \sqrt{\lambda L/\pi}$. Dephasing effects are included for three different time-scales $T' = 70\,T_{\mathrm{R}}$, $210\,T_{\mathrm{R}}$, and $700\,T_{\mathrm{R}}$.

$$\phi_{\mathrm{D}} = \frac{\lambda^2}{A}, \tag{3.15}$$

in the direction of the cylinder's symmetry axis where the phase-locking condition is fulfilled. Equation (3.14) can be rewritten as

$$I_{\mathrm{nc}} = \frac{2}{3}\frac{\hbar\omega}{AT_{\mathrm{R}}}, \tag{3.16}$$

using Equations (3.12) and (3.15). Equation (3.16) makes it clear that the non-coherent intensity is roughly N times smaller than the maximum superradiance intensity, since for the latter approximately N inverted molecules decay to their ground level over the characteristics time-scale of superradiance T_{R}.

In a large-sample, internal fluctuations (i.e., the thermal noise or spontaneous emission) as well as an external radiation can trigger superradiance. For the calculations presented in

Figure 3.2 we used internal fluctuations to set the initial Bloch angle at $\theta_0 = 2/\sqrt{N}$ [Gross and Haroche, 1982]. Once superradiance is initiated, dipoles in a large-sample lock into a common phase and radiate coherently after the delay time [Benedict et al., 1996]

$$\tau_{\rm D} \;\simeq\; \frac{T_{\rm R}}{4}\left|\ln\left(\frac{\theta_0}{2\pi}\right)\right|^2 . \tag{3.17}$$

For the above OH sample we have $\theta_0 = 4.7 \times 10^{-5}$ rad, which results in $\tau_{\rm D} \simeq 35\,T_{\rm R}$ using Equation (3.17), in good agreement with the time appearance of the first burst of radiation in Figure 3.2. As can be also seen in the figure, the total energy stored in the OH sample is released through consecutive bursts with a gradual drop in the peak intensities, with the number of bursts depending on the length of sample and the dephasing time-scale T'. More precisely, for longer samples and dephasing time-scales (e.g., for $T' = 210\,T_{\rm R}$ and $700\,T_{\rm R}$ in the figure) the process of re-absorption/re-emission takes place more frequently at the end-fire of the sample, leading to a larger number of burst events. However, we should also note that the (non-linear) Sine-Gordon equation is highly sensitive to initial conditions. It follows that the selected value for θ_0 also has an impact on the appearance of the intensity curve (e.g., in the number of bursts present).

It should be also pointed out that the scaled peak intensities in Figure 3.2 indicate the phase-locking factor $0.001 \lesssim f \lesssim 0.01$ depending on the dephasing time-scale. But the large number of inverted molecules N in an OH large-sample in a circumstellar envelope will imply, even when multiplied by such a small value for f, a significant enhancement factor resulting in $I_{\rm SR} \gg I_{\rm nc}$.

3.4 Discussion

The condition $\tau_{\rm D} < T'$ further implies $T_{\rm R} < T'$, since in a large-sample composed of $N \gg 1$ molecules $\tau_{\rm D}$ is at least an order of magnitude larger than $T_{\rm R}$ (see Equation [3.17]). More precisely, the average delay time, i.e., for several realizations of a superradiance system with a different θ_0, is given by [Gross and Haroche, 1982]

$$\langle \tau_{\rm D} \rangle = T_{\rm R} \ln\left(N\right), \tag{3.18}$$

which again indicates that $T_R < \langle \tau_{\rm D} \rangle$.

In a small-sample, where there are a relatively small number of atoms, the two time-scales $T_{\rm R}$ and $\langle \tau_{\rm D} \rangle$ are approximately of the same order of magnitude and the condition $\tau_{\rm D} < T'$ can be interchanged with $T_{\rm R} < T'$. For such cases the superradiance time-scale can be calculated from [Dicke, 1954]

$$T_{\rm R} = \frac{\tau_{\rm sp}}{\eta n_{\rm OH} V}, \tag{3.19}$$

where, once again, η is the population inversion factor, $n_{\rm OH}$ is the total molecular density, and V is the volume of the sample. A small-sample of OH molecules interacting with the 1612 MHz line is characterized by $V < \lambda^3 \sim 10^3$ cm^{-3}. Applying this constraint on the volume and substituting $\tau_{\rm sp} \sim 10^{11}$ sec for the 1612 MHz transition line transforms Equation (3.19) to

$$T_{\rm R} > \frac{10^8}{\eta n_{\rm OH}} \, \text{sec}, \tag{3.20}$$

yielding $T_{\rm R} > 10^9$ sec for $n_{\rm OH} \sim 10$ cm^{-3} [Gray et al., 2005] and $\eta \sim 0.01$, which are appropriate for masing regions in circumstellar envelopes. On the other hand, we previously calculated the time-scale of OH$-$H$_2$ collisions $T_{\rm c}$ in circumstellar OH samples to be $\sim 10^4$ sec to 10^6 sec for molecular hydrogen densities 10^6 cm^{-3} $> n_{\rm H_2} > 10^4$ cm^{-3} (see Section 3.2.1). Although our estimated range for this collision time-scale is likely under-estimated, it indicates that superradiance is unlikely to take place in corresponding OH small-samples since $T_{\rm c} = T' < T_{\rm R}$.

In a large-sample $T_{\rm R}$ is set by the two sample parameters: length L and density of inverted molecules n (see Equation [3.12]). Although it may initially appear that in a large-sample $T_{\rm R}$ can always be set to a value smaller than T' by adjusting L or n, in the ISM these parameters are constrained by the physical characteristics of the region within which the population inversion is realized.

In the case of CSE OH samples, the length of an inverted region depends on the mass-loss rate of the central pulsating star, which changes as the star evolves. The computational modeling of CSEs of OH-IR stars by Gray et al. [2005] suggests that the radial extent of OH population-inverted zones shrinks as the mass-loss rate of the central star increases.

More precisely, the mass-loss rate affects the optical depth of the infrared pump photons and subsequently the thickness of inverted OH zones. Hence, in higher mass-loss rates the envelope becomes more opaque to pump photons and the extent of the region accessible to pump decreases. It is expected that population-inverted regions typically range from 10^{11} cm to 10^{14} cm in thickness [Gray et al., 2005].

Using Equation (3.12) we can use this range for the length L of a cylindrical large-sample, along with our previous values of $n = \eta n_{\rm OH} = 0.1$ cm^{-3} (i.e., 643 molecules within λ^3) and $\tau_{\rm sp} = 7.8 \times 10^{10}$ sec to find $10^{-1}\,{\rm sec} \gtrsim T_{\rm R} \gtrsim 10^{-3}\,{\rm sec}$ for $10^{11}\,{\rm cm} < L < 10^{14}\,{\rm cm}$. Using a Fresnel number of unity to minimize diffraction losses in our calculations, specifying a radius $w = \sqrt{\lambda L/\pi}$ ranging from 7.7×10^5 cm to 2.4×10^7 cm, we find that $10\,{\rm sec} \gtrsim \langle \tau_{\rm D} \rangle \gtrsim 10^{-2}\,{\rm sec}$ for the same range of cylindrical lengths. The time-scales are evidently very short in comparison to our previous estimates of $10^4\,{\rm sec} < T_{\rm c} < 10^6\,{\rm sec}$. It thus appears reasonable to expect that superradiance could take place in the CSEs of such evolved stars. Indeed, we find that $\langle \tau_{\rm D} \rangle \sim 10^6$ sec for as small a value as $L = 10^5$ cm. Given these numbers, we now investigate potential observational evidence for superradiance in the OH 1612 MHz line.

3.4.1 The U Orionis Mira Star

U Orionis is a M8 III-type OH Mira variable with a period of 372 days, which has exhibited in the past significant variations in the intensity of several OH maser emission lines. Jewell et al. [1981] reported the results of their monitoring program of the 1612 MHz, 1665 MHz, and 1667 MHz masers observed in the CSE of U Ori, along with a compilation of similar data taken from several other sources [Pataki and Kolena, 1974, Reid et al., 1977, Cimerman, 1979, Fix, 1979] covering several years of observations (i.e., from 1974 to 1979). All three maser lines exhibited significant flaring events during that period. Although the 1665 MHz and 1667 MHz masers showed strong correlation in their intensity variations, the 1612 MHz maser displayed a completely different behavior characterized by the authors as a "damped oscillator decline" spanning about an order of magnitude in intensity range over the period. These variations were also clearly uncorrelated with the star's light curve (see Figure 1 of Jewell et al. 1981), and there has been no satisfactory explanation for such behavior that we are aware of so far.

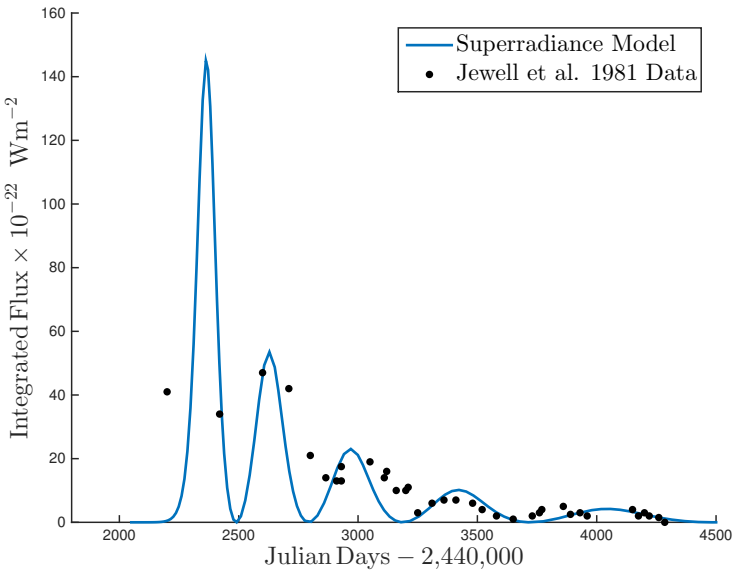

Figure 3.3: A superradiance intensity model (solid blue curve) with $T_{\rm R} = 6.5$ days, $T' = 393\,T_{\rm R}$, and $\theta_0 = 4.4 \times 10^{-5}$ rad superposed on data from Jewell et al. [1981] (black dots) obtained during the 1974 to 1979 OH 1612 MHz maser flaring episode of U Orionis.

Since the ringing in superradiance intensity displayed in the $T' = 210\,T_{\rm R}$ and $700\,T_{\rm R}$ curves shown in Figure 3.2 is also reminiscent of a "damped oscillator" behavior, the data of Jewell et al. [1981] provide us with a first opportunity to test our OH 1612 MHz superradiance model. We accordingly show in Figure 3.3 the results of our attempt. In the figure, the black dots are taken from Figure 1 of Jewell et al. [1981], while the (blue) solid curve is calculated from our model discussed in Section 3.3. We have once again used the internal fluctuation condition to trigger superradiance (i.e, $\theta_0 = 2/\sqrt{N}$), which resulted in $\theta_0 = 4.4 \times 10^{-5}$ rad ($\tau_{\rm D} \simeq 35\,T_{\rm R}$; see Equation [3.17]) for the chosen parameters $T_{\rm R} = 6.5$ days and $T' = 393\,T_{\rm R}$, while keeping $n = 0.1$ cm^{-3}. Given the simplicity of our one-dimensional superradiance model we have not attempted to perform any formal fit to the data, but merely adjusted the model's free parameters (i.e., $T_{\rm R}$ and T') to reproduce the main features found in the data. Our model was also "normalized" in intensity to that of the data. Unfortunately, the data is sparse early on (i.e., up to approximately Day 2600) and we cannot be certain of the proper behavior during that period, but the intensity is well constrained for the rest of the

observation period. We should also note that the data compiled in Jewell et al. [1981], realized with different facilities and instruments probing sometimes different polarization states, do not focus on a single spectral feature but rather represent the integrated flux over a finite bandwidth. Despite these facts and the simplicity of our model, the oscillatory behavior of the intensity is relatively well captured by the superradiance model. More precisely, the intensity of the last four maxima (at times beyond Day 2500) are reasonably well matched by the curve, both in their relative intensities and times of occurrence.

We note that the superradiant system stemming from our calculations yields a cylindrical length $L = 3.4 \times 10^4$ cm, which is orders of magnitude shorter than corresponding scales expected for masers. It follows that, within the context of our model, a large number of superradiant large-samples must be responsible for creating a radiation intensity strong enough to be detected during the flaring period (see Section 3.4.3 below). Also, the dephasing time T' needed to reproduce the data corresponds to approximately 7 years ($\sim 10^8$ sec and $\simeq 10\,\tau_{\rm D}$) and points to conditions significantly less constraining than those previously calculated for a thermally relaxed gas, as expected. This implies the existence of significant velocity coherence over the length L of a superradiant sample. This may not be surprising considering the Sobolev length for this source, which we evaluate to be $L_{\rm Sobolev} \sim 10^{16}$ cm using previously published data on the velocity gradient found in U Ori's CSE [Laury-Micoulaut et al., 1979]. The relative smallness of a superradiant sample (i.e., $L/L_{\rm Sobolev} \sim 10^{-12}$) is an indicator of small frequency shifts and longer dephasing time-scales in the superradiant samples.

3.4.2 The IRAS18276-1431 Pre-planetary Nebula

IRAS18276-1431 (OH17.7-2.0) is a pre-planetary nebula with a detached CSE and central star of spectral type earlier than K5, long known for its strong 1612 MHz OH maser emission [Bowers, 1978]. Wolak et al. [2014] have recently published the results of a monitoring campaign performed between 2002 and 2009, where emission from OH masers at 1612 MHz, 1665 MHz, and 1667 MHz was measured twice monthly using the Nançay Radio Telescope. While a monotonic decay and rise in intensity were detected at 1665 MHz and 1667 MHz, respectively, the integrated flux from the red-shifted part of the 1612 MHz spectrum revealed a significant intensity flare lasting approximately 6 years. Furthermore, during that same

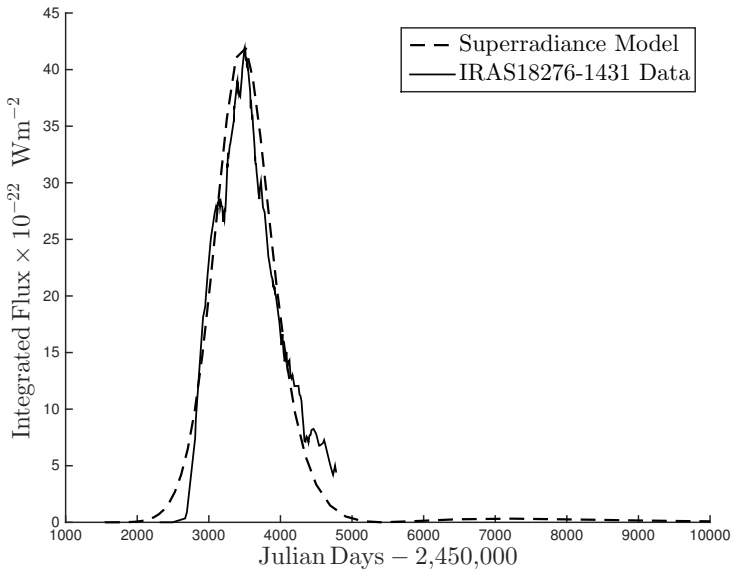

Figure 3.4: A superradiance intensity model (broken curve) with $T_{\rm R} = 42$ days, $T' = 61\,T_{\rm R}$, and $\theta_0 = 2.8 \times 10^{-4}$ rad superposed on data from Wolak et al. [2014] (solid curve) obtained during the 2002 to 2009 OH 1612 MHz maser flaring episode of IRAS18276-1431.

period the blue-shifted part of the spectrum only displayed a monotonic decay.

We show in Figure 3.4 the results of calculations using our superradiance model (broken curve) superposed to the data from Wolak et al. [2014] (solid curve) for the aforementioned flaring episode of the OH 1612 MHz line. Although the duration of the data does not allow us to determine if the burst of radiation taking place between approximately Day 2800 and Day 5000 is a single occurrence or part of a series of bursts, the longer duration of the flare (~ 2000 days) in comparison to case of U Ori and the expected limitation on the dephasing time T' seem to imply a single flare. Accordingly, our superradiance model yields $T_{\rm R} = 42$ days, $T' = 61\,T_{\rm R}$, and $\theta_0 = 2/\sqrt{N} = 2.8 \times 10^{-4}$ rad ($\tau_{\rm D} \simeq 25\,T_{\rm R}$), and provides a rewardingly nice match to the data.

As for U Ori, we note that the superradiance cylinder length $L = 5.2 \times 10^3$ cm is orders of magnitude shorter than those expected for masers, implying that a large number of superradiant large-samples are behind the measured intensity variation, while the required dephasing time $T' \simeq 7$ years ($\sim 10^8$ sec and $\simeq 2.4\,\tau_{\rm D}$) is markedly longer than the mean

collision times previously calculated for 10^4 cm^{-3} $\leq n_{\mathrm{H_2}} \leq 10^6$ cm^{-3} at $T = 100$ K, as expected. And, once again, because of the small size of a superradiant sample ($L = 5.2 \times 10^3$ cm) relative to typical values for the Sobolev length in the CSE of evolved stars, less constraining dephasing effects are anticipated.

3.4.3 Transition Between Maser and Superradiance Modes

The data sets from Jewell et al. [1981] and Wolak et al. [2014] both indicate transitions between periods of (quasi) steady state maser radiation and flaring episodes. Here we propose a scenario where such transitions could take place within the context of the superradiance model.

We know from our discussion in Section 3.2 that superradiance requires a dephasing time such that $T' > \tau_{\mathrm{D}}$. We therefore surmise, because of the relationship between τ_{D} and T_{R} given in Equation (3.17), the existence of a critical value $T_{\mathrm{R,crit}}$ for the characteristic time-scale of superradiance, which cannot be exceeded for superradiance to take place. That is, superradiance requires $T_{\mathrm{R}} \lesssim T_{\mathrm{R,crit}}$ with

$$T_{\mathrm{R,crit}} = \frac{4T'}{\left|\ln\left(\frac{\theta_0}{2\pi}\right)\right|^2}, \tag{3.21}$$

which in turn can be manipulated to yield, using Equation (3.12), a corresponding critical value for the product of the inverted population density n and the large-sample length L. In other words, superradiance also implies a column density of inverted molecules $nL \gtrsim (nL)_{\mathrm{crit}}$ with

$$(nL)_{\mathrm{crit}} = \frac{2\pi}{3\lambda^2}\frac{\tau_{\mathrm{sp}}}{T'}\left|\ln\left(\frac{\theta_0}{2\pi}\right)\right|^2. \tag{3.22}$$

In the AGB phase, the mass-loss rate can change significantly during thermal pulsation periods, when the evolved star blows away its mass in the form of super winds, or when the circumstellar envelope starts detaching from the star. These variations happen over relatively short time-scales (i.e., on the order of a few years) and can result in correspondingly important changes in L and n in an OH large-sample. However, variation in nL do not

necessarily require abrupt disruptions in the CSE and could happen more gradually over time or even because of local variations on smaller spatial scales.

Whatever the case may be, we can therefore imagine a situation where a region harboring an OH maser could experience a change in nL that would push it above the critical value given in Equation (3.22). At that point, the region over which $nL > (nL)_{\rm crit}$ would erupt into a superradiance mode that would overtake the maser process, since superradiance is a lot more efficient at radiating the energy stored in the sample (i.e., the superradiance radiation intensity scales with N^2). The initial maser radiation field itself could serve as a trigger for the superradiant event. Interestingly, our superradiance models for U Ori and IRAS18276-1431 show that nL (or $T_{\rm R}$ and $\tau_{\rm D}$) is only a factor of a few (at most an order of magnitude for U Ori) higher than the critical value.

The time-scales of the flaring events for U Ori and IRAS18276-1431 indicate, however, that the whole maser region cannot at once act as a single coherent radiating system. Presumably some other factor does not allow this to take place. For example, this could be because the level of velocity coherence is not high enough over the whole masing region to ensure that the corresponding dephasing time is sufficiently long to allow the entire region to act as a single superradiance system. On the other hand, velocity coherence is likely to be sufficient locally (i.e., on scales on the order of 10^3 cm to 10^4 cm for the examples considered here) to allow for the corresponding region within the maser to break-up into a large number of smaller superradiance large-samples. Our calculations presented in Figures 3.3 and 3.4, and their level of agreement with the corresponding data, provide credible evidence for such a scenario.

It is interesting to note that from an observational standpoint a single superradiant volume over which $nL > (nL)_{\rm crit}$ is unlikely to be resolvable in view of its spot size on the sky. This would be unusual for masers, which are often resolvable through high-resolution interferometry observations. This could also imply, based on the model discussed here, that an unresolvable source in a masing region exhibiting characteristics associated with superradiance (e.g., the ringing effect in the intensity variations) could be associated to a system composed of a single or a few superradiant sources operating within that region. However, as is implied by the discussion above, the converse is not necessarily true. That is,

the fact that a source is spatially resolved does not imply that it cannot consist of a group composed of a large number of superradiant systems.

Finally, within the context of the model presented here, since a given region can make transitions between maser and superradiance modes we would expect that similar proper motion properties apply to both types of sources.

3.5 Conclusion

We have applied the concept of superradiance introduced by Dicke [1954] to the OH molecule 1612 MHz spectral line often used for the detection of masers in CSEs of evolved stars. As the detection of 1612 MHz OH masers in the outer shells of envelopes of these stars implies the existence of a population inversion and a high level of velocity coherence, and that these are two necessary requirements for superradiance, we investigated whether superradiance can also take place in these regions. Our analysis suggests that superradiance provides a valid explanation for previous observations of intensity flares detected in that spectral line for the U Orionis Mira star [Jewell et al., 1981] and the IRAS18276-1431 pre-planetary nebula [Wolak et al., 2014]. The confirmation of superradiance in these sources would not only reveal a new range of unexplored physical conditions in the ISM but, on a more fundamental level, also reveal the existence of coherent quantum mechanical systems and corresponding entangled states over length scales reaching a few times 10^4 cm.

Bibliography

W. A. Baan, P. A. D. Wood, and A. D. Haschick. Broad hydroxyl emission in IC 4553. *The Astrophysical Journal*, 260:L49–L52, 1982.

M. G. Benedict, A. M. Ermolaev, V. A. Malyshev, I. V. Sokolov, and E. D. Trifonov. *Superradiance Multiatomic Coherent Emission*. Bristol: IOP Publishing Ltd, 1996.

M. Bertolotti. *Masers and lasers: an historical approach*. Boca Raton, FL: CRC Press, 2015.

P. F. Bowers. A large-scale OH sky survey at 1612 MHz. part I. the observations. *Astronomy and Astrophysics Supplement Series*, 31:127–145, 1978.

M. Cimerman. The flare in the U Orionis OH maser. *The Astrophysical Journal*, 228: L79–L82, 1979.

J. Darling and R. Giovanelli. A search for OH megamasers at z> 0.1. III. the complete survey. *The Astronomical Journal*, 124(1):100, 2002.

R. H. Dicke. Coherence in spontaneous radiation processes. *Physical Review*, 93(1):99, 1954.

B. T. Draine. *Physics of the interstellar and intergalactic medium*. Princeton University Press, 2011.

M. Elitzur. *Astronomical masers*, volume 170 of *Astrophysics and Space Science Library*. Dordrecht: Kluwer, 1992.

M. Elitzur, P. Goldreich, and N. Scoville. OH-IR stars. II. a model for the 1612 MHz masers. *The Astrophysical Journal*, 205:384–396, 1976.

J. D. Fix. Outbursts in the main line OH emission from U Orionis. *The Astrophysical Journal*, 232:L39–L42, 1979.

P. Goldreich and N. Scoville. OH-IR stars. I-physical properties of circumstellar envelopes. *The Astrophysical Journal*, 205:144–154, 1976.

M. Gray. Astrophysical masers. *Philosophical Transactions of the Royal Society of London A: Mathematical, Physical and Engineering Sciences*, 357(1763):3277–3298, 1999.

M. Gray. *Maser Sources in Astrophysics*. New York: Cambridge Univ. Press, 2012.

M. D. Gray, D. A. Howe, and B. M. Lewis. Evolution of 1612-MHz maser emission in expanding circumstellar shells. *Monthly Notices of the Royal Astronomical Society*, 364 (3):783–795, 2005.

M. Gross and S. Haroche. Superradiance: An essay on the theory of collective spontaneous emission. *Physics Reports*, 93:301–396, December 1982.

P. M. Harvey, K. P. Bechis, W. J. Wilson, and J. A. Ball. Time variations in the OH microwave and infrared emission from late-type stars. *The Astrophysical Journal Supplement Series*, 27:331–357, 1974.

J. H. He. The OH 1612 MHz maser pump rates of stellar, interstellar and post-AGB OH masers. *New Astronomy*, 10(4):283–299, 2005.

J. A. Irwin. *Decoding the Cosmos*. Chichester: Wiley, 2007.

P. R. Jewell, J. C. Webber, L. E. Snyder, and M. Elitzur. Monitoring of OH maser emission from late-type stars. *The Astrophysical Journal Supplement Series*, 41:191–207, 1979.

P. R. Jewell, J. C. Webber, and L. E. Snyder. Evolution of the OH maser emission from U Orionis. *The Astrophysical Journal*, 249:118–123, October 1981.

H. Karttunen, P. Kröger, H. Oja, M. Poutanen, and K. J. Donner. *Fundamental astronomy*. Springer Science & Business Media, 2007.

N. D. Kylafis and C. A. Norman. Collisional pumping of OH masers in the 2pi(1/2) ladder. *The Astrophysical Journal*, 350:209–215, 1990.

H. J. Lamers and J. P. Cassinelli. *Introduction to stellar winds*. Cambridge University Press, 1999.

C. Laury-Micoulaut, A. Winnberg, G. V. Schultz, et al. OH maser luminosity and expansion velocity gradient in Mira envelopes. *Astronomy and Astrophysics*, 75:351–364, 1979.

M. M. Litvak. Infrared pumping of interstellar OH. *The Astrophysical Journal*, 156:471, 1969.

P. Lockett and M. Elitzur. The effect of 53 m IR radiation on 18 cm OH megamaser emission. *The Astrophysical Journal*, 677(2):985, 2008.

J. McBride, C. Heiles, and M. Elitzur. Constraints on OH megamaser excitation from a survey of OH satellite lines. *The Astrophysical Journal*, 774(1):35, 2013.

R. X. McGee, B. J. Robinson, F. F. Gardner, and J. G. Bolton. Anomalous intensity ratios of the interstellar lines of OH in absorption and emission. *Nature*, 208:1193, 1965.

A. R. Offer, M. C. van Hemert, and E. F. van Dishoeck. Rotationally inelastic and hyperfine resolved cross sections for OH–H2 collisions. calculations using a new abinitio potential surface. *The Journal of Chemical Physics*, 100(1):362–378, 1994.

L. Pataki and J. Kolena. A change in the nature of the OH emission from U Orionis. In *Bulletin of the American Astronomical Society*, volume 6, page 340, 1974.

Fereshteh Rajabi and Martin Houde. Dickes superradiance in astrophysics.I. the 21 cm Line. *The Astrophysical Journal*, 826(2):216, 2016.

M. J. Reid, D. O. Muhleman, J. M. Moran, K. J. Johnston, and P. R. Schwartz. The structure of stellar hydroxyl masers. *The Astrophysical Journal*, 214:60–77, 1977.

P. C. Souers. *Hydrogen properties for fusion energy*. University of California Press, 1986.

S. W. Stahler and F. Palla. *The formation of stars*. John Wiley & Sons, 2008.

B. E. Turner. Anomalous emission from interstellar hydroxyl and water (concluded). *Journal of the Royal Astronomical Society of Canada*, 64:282, 1970.

H. Weaver, D. R. W. Williams, N. H. Dieter, and W. T. Lum. Observations of a strong unidentified microwave line and of emission from the OH molecule. *Nature*, 208:29–31, 1965.

S. Weinreb, A. H. Barrett, M. L. Meeks, and J. C. Henry. Radio observations of OH in the interstellar medium. *Nature*, 200(4909):829–831, 1963.

J. P. Wittke and R. H. Dicke. Redetermination of the hyperfine splitting in the ground state of atomic hydrogen. *Physical Review*, 103(3):620, 1956.

P. Wolak, M. Szymczak, A. Bartkiewicz, and E. Gerard. Violent maser events in the cirumstellar envelope of the pre-planetary nebula IRAS18276-1431. In *Proceedings of the 12th European VLBI Network Symposium and Users Meeting (EVN 2014). 7-10 October 2014. Cagliari, Italy*, volume 1, page 116, 2014.

Chapter 4

Dicke's Superradiance in Astrophysics. III – The 6.7-GHz Methanol and 22-GHz Water Maser Lines[1]

4.1 Introduction

Since their first detection in the OH 18 cm lines [Weaver et al., 1965], a large number of masers from several molecules were discovered in both galactic and extragalactic environments. The main characteristics of masers include very high brightness temperatures, corresponding to very high emission intensities over small spatial scales, narrow line-widths, and occasionally high levels of polarization across the spectral lines [Elitzur, 1992, Gray, 2012]. These attributes of the maser action result from the stimulated emission process in a medium where a population inversion is established and maintained, leading to large amplifications along optical paths exhibiting good velocity coherence for the spectral line under consideration.

In addition, observations show that some maser sources exhibit significant intensity vari-

[1]A modified version of this chapter has been submitted to Science Advances (F. Rajabi and M. Houde 2016, Explaining Recurring Maser Flares in the ISM Through Large-scale Entangled Quantum Mechanical States, Science Advances, submitted.)

ability on time-scales ranging from days to several years. The 22-GHz water masers in Orion KL, for example, exhibited drastic flux density variations over a six-year period between 1979 to 1985 [Matveenko et al., 1988, Garay et al., 1989]. This phase of activity was followed by a twelve-year quiescent period that ended in 1997, when subsequent burst activity was detected in this source [Omodaka et al., 1999]. Although the majority of flaring sources display abrupt changes of flux density through isolated impulsive phases [Mattila et al., 1985], interestingly, intensity variations in some sources are sometimes found to be periodic, where the corresponding maser transition regularly alternates between phases of high activity and quiescence [Goedhart et al., 2003, Szymczak et al., 2015]. Although a number of models are proposed to explain such time-variations, the underlying mechanism for most of these observations still remains obscure [van der Walt et al., 2009, Parfenov and Sobolev, 2014].

Some of the aforementioned requirements for the maser action, i.e., population inversion and velocity coherence, are also necessary for superradiance; a fundamentally different radiation enhancement process. Superradiance, introduced by Dicke in 1954, is a coherent and cooperative quantum mechanical phenomenon by which a group of N inverted atoms/molecules emit a radiation pulse (burst) of intensity proportional to N^2. Although virtually unknown to astrophysicists, superradiance has become a very intense research field within the physics community since its introduction by Dicke [1954, 1964] and its initial laboratory confirmation by Skribanowitz et al. [1973] (see also Gross and Haroche 1982, Benedict et al. 1996). As superradiant pulses can exhibit a temporal behavior resembling that of flares discovered for some masers in the circumstellar envelope (CSE) of evolved stars or elsewhere in the interstellar medium (ISM), we recently started investigating the possibility of superradiance within the context of astrophysics and concluded it could, in principle, take place in some regions when the necessary conditions are met (i.e., population inversion, velocity coherence, and long dephasing time-scales compared to those characterizing superradiance; see Rajabi and Houde 2016a,b). More precisely, the results of our analyses suggest that superradiant bursts are possible over a wide range of time-scales in regions spanning relatively small astronomical length-scales. As will be discussed in Section 4.3, we also recently provided some observational evidence for the OH 1612 MHz maser line using data taken from the existing literature [Rajabi and Houde, 2016b].

In this paper, we extend our analysis to the methanol 6.7-GHz and water 22-GHz maser transitions using the one-dimensional formalism presented in Rajabi and Houde [2016a,b]. We start with a brief summary of the important parameters used in our numerical analyses of Section 4.2. The superradiance model is then in turn applied to the methanol 6.7-GHz data from the G33.64-0.21 star-forming region in Section 4.3.1 [Fujisawa et al., 2012, 2014] and the water 22-GHz data from Cep A in Section 4.3.2 [Mattila et al., 1985], while in Section 4.3.3 the results of our analyses for these two lines are used to explain the recent observation of periodic and seemingly alternating flares of methanol and water masers in G107.298+5.639 [Szymczak et al., 2016]. Finally, we end with a brief conclusion in Section 4.4.

4.2 Superradiance Model

In this section we apply the one-dimensional superradiant model presented in Rajabi and Houde [2016b] for electric dipole transitions to existing observations of the methanol 6.7-GHz and water 22-GHz maser lines. Our goal is to explain the peculiar intensity variations (bursts) previously detected in the G33.64-0.21 (methanol 6.7-GHz; Fujisawa et al. 2012, 2014), Cep A (water 22-GHz; Mattila et al. 1985), and G107.298+5.639 (both lines; Szymczak et al. 2016) star-forming regions. As will be discussed below, all of these sources exhibited intensity variation behaviors that are typical of superradiant systems. More precisely, the first two sources showed a type of "damped oscillator" response in their intensity curves while the last displayed series of single-bursts.

As was recently discussed in Rajabi and Houde [2016a,b], a rapid and significant increase (sometimes followed by oscillations) in radiation intensity is a behavior typical of a (large-sample) superradiant system. In particular, the analyses of Rajabi and Houde [2016b] established that superradiance provides a viable explanation for the observed OH 1612-MHz intensity bursts detected in the Mira star U Orionis [Jewell et al., 1981] and the pre-planetary nebula IRAS18276-1431 [Wolak et al., 2014]. The response of a superradiant system is characterized by a few parameters, the most important being the characteristic time-scale of

superradiance $T_{\rm R}$, which is given by

$$T_{\rm R} = \tau_{\rm sp} \frac{8\pi}{3nL\lambda^2}, \tag{4.1}$$

where $\tau_{\rm sp}$ is the spontaneous decay time-scale of a single molecule (i.e., the inverse of the Einstein spontaneous emission coefficient), n the density of inverted molecules taking part in the superradiant process, L the length of the (cylindrical) large-sample (nL is thus the column density of inverted molecules), and λ the wavelength of the radiation interacting with the molecules in the superradiance system. For a given transition, λ and $\tau_{\rm sp}$ are fixed and $T_{\rm R}$ thus only depends on the column density of molecules partaking in superradiance.

When a superradiant system is inverted through some pumping mechanism and a critical threshold for the inverted column density is met or exceeded (see Eq. [4.3] below), the energy stored in the system is released after the so-called delay time $\tau_{\rm D}$ given by

$$\tau_{\rm D} \simeq \frac{T_{\rm R}}{4} \left| \ln\left(\frac{\theta_0}{2\pi}\right) \right|^2, \tag{4.2}$$

with the initial Bloch angle $\theta_0 = 2/\sqrt{N}$, where N is the number of inverted molecules in the sample [Gross and Haroche, 1982, Benedict et al., 1996]. While the delay time $\tau_{\rm D}$ gives an estimate of the time when the first superradiance burst takes place, the characteristic time $T_{\rm R}$ sets the duration of each burst. In a superradiance large-sample, the energy can be radiated away through a series of bursts, through a phenomenon known as the ringing effect. The number of ringing oscillations varies as a function of T', the time-scale of the most important dephasing effect (e.g., collisions) that will tend to work against the superradiance phenomenon.

In a more general sense, superradiance can be only observed if $\tau_{\rm D} < T'$ (see Rajabi and Houde 2016a,b for more details), and this implies the existence of the aforementioned threshold in inverted-population column density

$$(nL)_{\rm crit} \approx \frac{2\pi}{3\lambda^2} \frac{\tau_{\rm sp}}{T'} \left| \ln\left(\frac{\theta_0}{2\pi}\right) \right|^2 \tag{4.3}$$

that must be met for the initiation of superradiance. More precisely, for column densities below this critical value the dephasing effects prevent coherent interactions and the system operates in a maser regime. As soon as $nL \gtrsim (nL)_{\rm crit}$ the system switches to a superradiance

mode and the masing region breaks into a large number of superradiance large-samples for which this condition is met [Rajabi and Houde, 2016b]. It is also important to note that whether $(nL)_{\rm crit}$ is crossed through a slow increase in pumping of the column density or a fast population-inverting pulse is irrelevant. That is, it only matters that the condition $nL \gtrsim (nL)_{\rm crit}$ is somehow reached.

Given the parameters $T_{\rm R}$ (or nL) and T', which fully characterize a superradiance intensity curve, we have tested our superradiance model on data from the three aforementioned star-forming regions, as will be presented below. In order to do so, we have chosen $T_{\rm R}$ and T' as free parameters in the fitting process and tried to reproduce the intensity curves given by the data. It must however be noted that, as was observed in Rajabi and Houde [2016b] for the OH 1612 MHz line superradiance bursts observed in U Orionis and IRAS18276-1431, the volume occupied by a single superradiant large-sample is several orders of magnitude smaller than a typical maser region. A similar statement applies to the cases studied in this paper. It follows that the superradiance intensity curves must result from the contributions of a very large number of separate but simultaneously triggered superradiant samples. We have therefore augmented our one-dimensional superradiance model to account for this by averaging over several realizations of superradiance samples for which a common T' is used. These realizations result from a Gaussian-distributed ensemble of $T_{\rm R}$ values of mean $\langle T_{\rm R} \rangle$ and standard deviation $\sigma_{T_{\rm R}}$. The results of our analyses are discussed in details in the following sections.

4.3 Results and Discussion

4.3.1 The High-mass Star-forming Region G33.64-0.21

G33.64-0.21 is a high-mass star-forming region located at a kinematic distance of 4.0 kpc with an estimated infrared luminosity of $1.2 \times 10^4 L_\odot$ [Fujisawa et al., 2014]. The spectra of the 6.7 GHz methanol masers in G33.64-0.21 were monitored daily with the Yamaguchi 32-m Radio Telescope over several time intervals from 2009 to 2015 by Fujisawa et al. [2012]. The corresponding observations identified five narrow maser spectral features (Components

I to V, defined with increasing line-of-sight velocity; see Fig. 1 of Fujisawa et al. 2012) with line widths of approximately $0.3\,\mathrm{km\,s^{-1}}$. Two bursts of radiation, lasting on the order of ten days, were observed in Component II ($v_{\mathrm{lsr}} = 59.6\,\mathrm{km\,s^{-1}}$) in July and August 2009, while all other velocity components did not exhibit any significant change in their flux densities over similar timescales or longer (see Fig. 2 of Fujisawa et al. 2012). During both events, the flux densities increased approximately sevenfold within 24 hours and then returned to their original value while exhibiting a damped oscillator behavior. Subsequent observations with the Japanese VLBI Network revealed that Component II, responsible for the two bursts, emanates from the southwestern edge of G33.64-0.21 within a region measured to be much smaller than 70 AU. Different scenarios were proposed to explain these observations, but none were so far able to adequately describe an energy release mechanism responsible for such bursting behavior.

Given the damped oscillator character of the intensity curve during the bursts, we investigate the possibility of superradiance in the 6.7 GHz methanol line in an attempt to explain the energy relaxation mechanism at play for G33.64-0.21. Here, we focus on the second burst appearing in August 2009 in Figure 2 of Fujisawa et al. [2012]. The results of our analyses show that a group of methanol superradiance large-samples of mean inverted column density $\langle nL\rangle \sim 7\times10^{4}\,\mathrm{cm^{-2}}$ (e.g., of density $n \sim 0.1\,\mathrm{cm^{-3}}$ and length $L \sim 10^{6}\,\mathrm{cm}$) can reproduce similar intensity variations as that of the 6.7 GHz line detected in G33.64-0.21. In Figure 4.1 we show the average intensity (scaled to the data) obtained with 1000 such superradiance large-samples (the shape of the intensity curve converges after a few hundred realizations) calculated using our one-dimensional model (solid blue curve) superposed on the data from Fujisawa et al. [2012] (black dots). The superradiance sample realizations are generated using $\langle T_{\mathrm{R}}\rangle = 1.1\,\mathrm{hr}$, $\sigma_{T_{\mathrm{R}}} = 0.07\,\langle T_{\mathrm{R}}\rangle$ and $T' = 600\,\langle T_{\mathrm{R}}\rangle$. As seen in the figure, our superradiance model agrees well with the data and is successful in reproducing the main characteristics of the observed intensity curve.

The observations of Fujisawa et al. [2012] were initially carried out daily (from Day 5039 to Day 5043 in Fig. 4.1) followed by alternate day monitoring of the source. As a result, the data are sparse considering the rapid intensity variations exhibited by the superradiance curve. This also implies that the peak flux density detected by Fujisawa et al. [2012] may

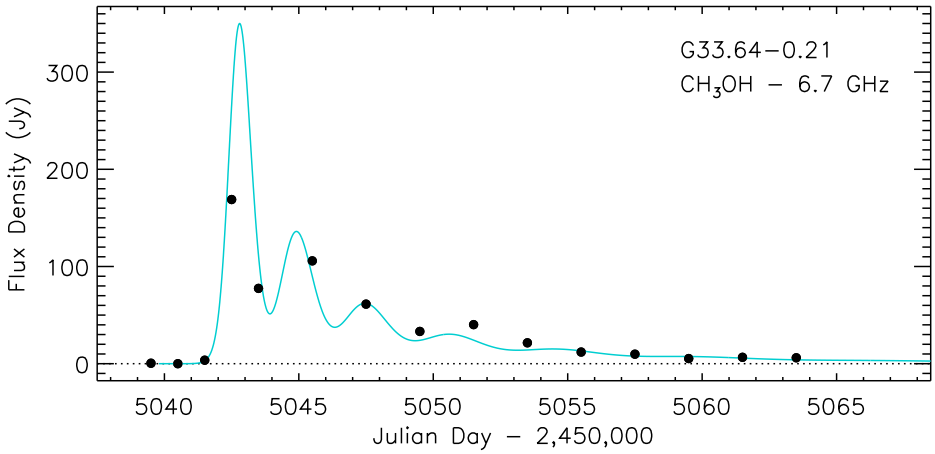

Figure 4.1: A superradiance large-sample intensity model (solid blue curve) superposed on the data from Fujisawa et al. [2012] (black dots) obtained in July and August 2009 for the second methanol 6.7-GHz burst in G33.64-0.21. The superradiance intensity is averaged over 1000 large-samples taken from a Gaussian-distributed ensemble of $T_{\rm R}$ values of mean and standard deviation of $\langle T_{\rm R}\rangle = 1.1\,{\rm hr}$ and $\sigma_{T_{\rm R}} = 0.07\,\langle T_{\rm R}\rangle$, respectively, and scaled to the data. The dephasing time scale was set to $T' = 600\,\langle T_{\rm R}\rangle$ for all samples, and the superradiance pulses were initiated from internal fluctuations characterized by an initial Bloch angle $\langle\theta_0\rangle \sim 10^{-6}\,{\rm rad}$.

not represent the actual maximum experienced by the source; our model indicates a peak flux density of 350 Jy late on Day 5042.

As previously mentioned, our calculations suggest that superradiance will develop in samples of significantly smaller sizes than that of a typical methanol maser. A very large number of superradiance large-samples, contained within the region harboring the maser, must therefore be responsible for the detected radiation intensity. Finally, the dephasing time-scale T' used to produce the solid curve is on the order of a month, which is reasonable within the expected gas densities $10^4\,{\rm cm}^{-3} < n_{\rm H_2} < 10^9\,{\rm cm}^{-3}$ and temperature $T < 300$ K in G33.64-0.21 [Cragg et al., 2005].

4.3.2 The High-mass Star-forming Region Cepheus A

Cepheus A (Cep A) with 14 compact HII regions is a high-mass star-forming site located at a distance of ~ 0.7 kpc [Mattila et al., 1985]. In 1978, the 22-GHz water observations toward this source revealed high time-variability to be followed by a strong burst at $V_{\rm lsr} = -8\,{\rm km\,s^{-1}}$ between April and December 1980. In October 1980, when this burst was in its decay phase Mattila et al. [1985] started a three-year monitoring program of Cep A using the 14-m radio telescope of the Metsähovi Radio Research Station. This source was monitored through monthly observations until October 1983, except for a few time-spans where observations were repeated daily or every few days. In April 1983, the flux-density of the water 22-GHz line at $V_{\rm lsr} = -11.2\,{\rm km\,s^{-1}}$ increased sixfold over 10 days reaching its maximum value of 1700 Jy on April 18. Later on, over the following 40 days, the flux density decayed to a background value while exhibiting a "damped oscillator" behavior. During this phase, a few secondary maxima were detected every 15 days or so. Different models were used to reproduce the observed light curve for this burst, but they were either unsuccessful in replicating the time-scale of the event or did not capture the secondary maxima.

In an attempt to explain the aforementioned observations during the 1983 burst in Cep A, we have applied our superradiance model to the water 22-GHz line. In Figure 4.2 we show the superradiance intensity curve (scaled to the data) calculated using an ensemble of 1000 superradiance large-samples (solid blue curve) superposed on data from Figure 4c of Mattila et al. [1985] (black dots). The superradiance realizations are produced using $\langle T_{\rm R}\rangle = 8.2\,{\rm hr}$, $\sigma_{T_{\rm R}} = 0.1\,\langle T_{\rm R}\rangle$ and $T' = 700\,\langle T_{\rm R}\rangle$. As seen in the figure the superradiance curve (solid curve) occurs over similar time-scale as that for the data and analogously exhibits a peak followed by secondary maxima as it damps. The relative intensities of the secondary maxima match that of the data reasonably well while the main peak exceeds the data. Given the simplicity of our superradiance model we can conclude that the overall behavior of the burst is well-captured by this model.

It must be noted that the water rotational energy levels ($J_{\rm K_aK_c} = 6_{16}$ and 5_{23}) corresponding to the 22-GHz line are degenerate and, in principle, superradiance can simultaneously operate in more than one of the corresponding hyperfine components. This can complicate

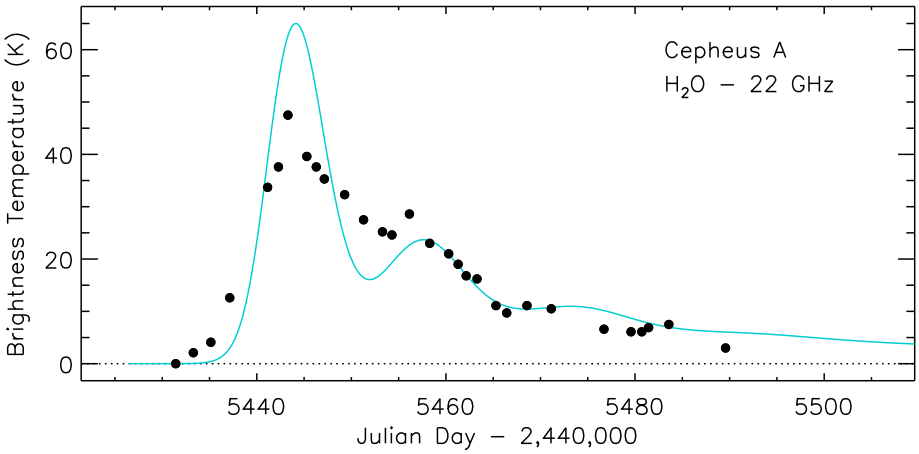

Figure 4.2: A superradiance large-sample intensity model (solid blue curve) superposed on data from Mattila et al. [1985] (black dots) obtained in April and May 1983 for the water 22-GHz burst at $V_{\rm lsr} = -11.2\,{\rm km\,s^{-1}}$ in Cep A. The superradiance intensity is generated using 1000 superradiance realizations with $\langle T_{\rm R}\rangle = 8.2\,{\rm hr}$, $\sigma_{T_{\rm R}} = 0.1\,\langle T_{\rm R}\rangle$ and a constant dephasing time-scale $T' = 700\,\langle T_{\rm R}\rangle$.

the line flux-density analysis due to the variation of the relative intensity of the degenerate transitions and their time of occurrence, which our superradiance model does not account for since it employs a two-level system approximation. This may be partly responsible for the disagreement between the model peak intensity and the data. Another factor that may have an impact is the large half-power beam width ($\approx 4'$) of the telescope used for these observations, which were inevitably sensitive to an extended region and perhaps suffer contamination from a number of sources.

Once again, the results of our analysis suggests that a large group of water superradiance samples of mean inverted column density $\langle nL\rangle \sim 6\times10^4\,{\rm cm^{-2}}$ (e.g., $n \sim 1\,{\rm cm^{-3}}$ and $L \sim 10^5\,{\rm cm}$) must be responsible for the observed radiation intensity. We also note that the dephasing time-scale $T' = 700\,\langle T_{\rm R}\rangle$ or 238 days resulting from our calculations is less restrictive than the estimated collision time-scales for a given molecular hydrogen density $n_{\rm H_2} = 10^8\,{\rm cm^{-3}}$ at $T \sim 100\,{\rm K}$ to $\sim 200\,{\rm K}$ consistent with the pumping model of water masers [Elitzur et al., 1989, Szymczak et al., 2016].

4.3.3 The Methanol 6.7-GHz and Water 22-GHz flares in G107.298+5.639

G107.298+5.639 is an intermediate-mass young stellar object deeply embedded in the molecular cloud L1204/S140 [Szymczak et al., 2016] at a distance of $\sim$ 0.9 kpc [Crampton and Fisher, 1974]. For the periods of July to December 2014 and similarly in 2015, Szymczak et al. [2016] monitored methanol 6.7-GHz and water 22-GHz masers in this source with the Torun 32-m Radio Telescope. During high activity intervals, the methanol observation rate was increased to eight times a day whereas in quiescent periods they were conducted only once a week. The water observations were, however, repeated daily with eight gaps of 4 to 5 days of no observations.

The observations of the methanol 6.7-GHz masers indicated four features, among which the $v_{\rm lsr} = -7.4$ km s^{-1}, -8.6 km s^{-1}, and -9.2 km s^{-1} components exhibited a 34.4-day cyclic behavior. Faint emission was also detected in a few spectral features in the velocity range of $v_{\rm lsr} = -17.2$ km s^{-1} to -13.6 km s^{-1}, although these components did not show the same periodicity. The cyclic methanol components showed strong flux variations in the form of a repeating (lone) burst taking place over time-scales of four to twelve days.

The 22 GHz water maser emission was also detected in six features at velocities ranging from $v_{\rm lsr} = -18.3$ km s^{-1} to -1.1 km s^{-1}. Importantly, some features (e.g., those near $v_{\rm lsr} = -16.5$ km s^{-1} and -8 km s^{-1}) peaked in intensity with the same periodicity as, but delayed relative to, methanol flares at velocities located within ± 1.1 km s^{-1} of those of the water masers themselves. A similar behavior was detected at a velocity near $v_{\rm lsr} = -11.0$ km s^{-1} where methanol and water flares were also observed in alternation. Based on high angular resolution data sets collected with the European VLBI Network (EVN) and VLBI Exploration of Radio Astrometry (VERA) [Hirota et al., 2008], Szymczak et al. [2016] concluded that some of the periodically alternating methanol and water flares originate from the same volume of molecular gas of 30 to 80 AU in size.

In order to find a viable explanation for these observations a number of scenarios were examined, but none were able to adequately reproduce the observations. The observed alternation of the water and methanol maser bursts is the main feature to be explained. However,

this is very difficult to achieve within the context of maser theory, even with the assumptions that the two types of masers happen in the same region and are being periodically enhanced by some pulsating pumping source. For example, it is hard to conceive how the water and methanol maser features would then occur in alternation while also showing different time durations for their flares. We now show how this kind of behavior naturally arises, and should be expected, when studied within the context of Dicke's superradiance.

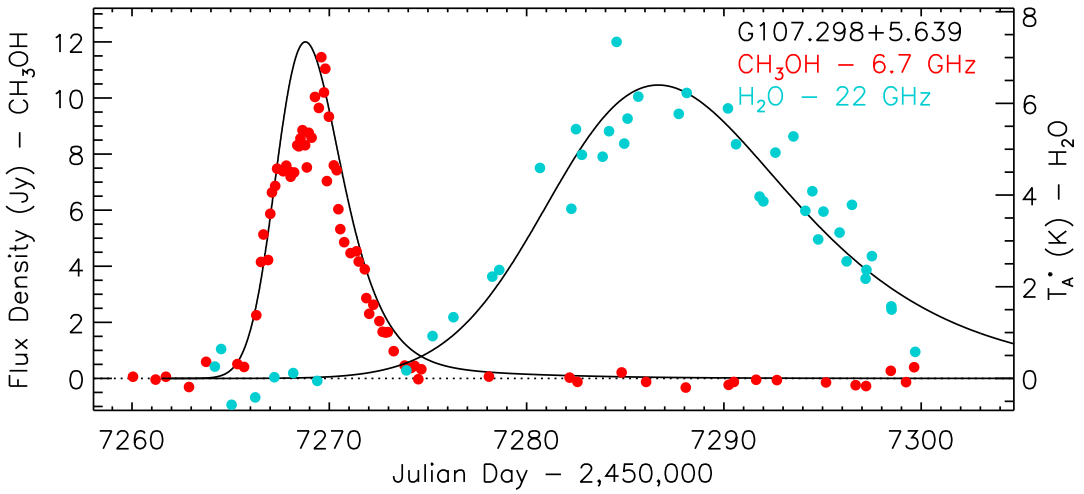

Figure 4.3: Superradiance models (solid curves) for the G107.298+5.639 flaring event occurring between MJD 57,260 to 57,300 in Figure 3 of Szymczak et al. [2016] (i.e., Day 7260 to 7300 in our figure) for the $v_{\rm lsr} = -8.57\,{\rm km\,s^{-1}}$ 6.7-GHz methanol (red dots) and $v_{\rm lsr} = -7.86\,{\rm km\,s^{-1}}$ 22-GHz water (blue dots) spectral features. Such flares repeated on an approximately 34.4-day period [Szymczak et al., 2016]. The methanol and water data/models use the vertical axes on the left- and right-hand sides, respectively. For methanol the model parameters are $\langle T_{\rm R}\rangle_{\rm CH_3OH} = 2.1{\rm hr}$, $\sigma_{\rm T_R,CH_3OH} = 0.07\,\langle T_{\rm R}\rangle_{\rm CH_3OH}$ and $T'_{\rm CH_3OH} = 90\,\langle T_{\rm R}\rangle_{\rm CH_3OH}$, yielding a mean inverted column density of $\langle nL\rangle_{\rm CH_3OH} \approx 3.5\times10^4\,{\rm cm^{-2}}$, while for water we have $\langle T_{\rm R}\rangle_{\rm H_2O} = 7.7\,{\rm hr}$, $\sigma_{\rm T_R,H_2O} = 0.04\,\langle T_{\rm R}\rangle_{\rm H_2O}$, $T'_{\rm H_2O} = 70\,\langle T_{\rm R}\rangle_{\rm H_2O}$, and $\langle nL\rangle_{\rm H_2O} \approx 8.4\times10^4\,{\rm cm^{-2}}$. Despite the apparent time ordering between the methanol and water flares, both superradiance models were initiated at the same time, on Day 7261.5.

We assume that we are in the presence of a periodically changing pumping source that

simultaneously acts on the population levels of both the 22 GHz water and 6.7 GHz methanol transitions. Although we are not aware of any other observations (beside the periodic maser flares discussed here) that could provide evidence for such a scenario in G107.298+5.639, we know of at least one other young protostellar system where strong, cyclic variations in infrared luminosity have been observed with a period comparable to that seen in G107.298+5.639 (i.e., 25.34 day for LRLL 54361; see Muzerolle et al. 2013). Such infrared intensity variations could, in principle, directly affect the pumping level of the maser transitions. Given this assumption, we can apply our superradiance model to understand the behavior of the water and methanol maser emission observed in G107.298+5.639.

It is important to note that for a given inverted column density the value of $T_{\rm R}$, and therefore the durations of superradiant bursts for different spectral lines scale as $\tau_{\rm sp}/\lambda^2$ (see Eq. [4.1]). It follows that, under similar conditions (i.e., assuming for the moment that $(nL)_{\rm CH_3OH} \approx (nL)_{\rm H_2O}$), we should expect a superradiance time-scale ratio of approximately $1 : 8.7$ between the methanol 6.7 GHz and water 22 GHz lines, respectively. In fact, this expected relationship between $T_{\rm R,CH_3OH}$ and $T_{\rm R,H_2O}$ provides us with the needed element to explain the observations of Szymczak et al. [2016]. That is, since $T_{\rm R}$ sets both the duration of the superradiant burst and the time delay $\tau_{\rm D}$ before its emergence (see Eq. [4.2]) it is to be expected that the methanol flares will be narrower and appear earlier than those for water. Evidently, it is unlikely that the inverted column densities for methanol at 6.7 GHz and water at 22 GHz will be the same, and we thus relax this approximation in what follows. But the above scenario should still hold for cases where their difference is not too pronounced.

Given the observed duration of flares for the methanol 6.7-GHz and water 22-GHz masers, we adjusted the values of $T_{\rm R}$ for these transitions to reproduce superradiant bursts of similar time-scales (i.e., approximately 10 days for methanol and 30 days for water). The result of our analysis is shown in Figure 4.3. The superradiance intensity models (solid curves) were calculated using ensembles of 1000 superradiance large-samples tailored to the flaring event occurring between MJD 57,260 to 57,300 in Figure 3 of Szymczak et al. [2016] (i.e., Day 7260 to 7300 in our Figure 4.3) for the $v_{\rm lsr} = -8.57\,{\rm km\,s^{-1}}$ 6.7-GHz methanol (red dots) and $v_{\rm lsr} = -7.86\,{\rm km\,s^{-1}}$ 22-GHz water (blue dots) spectral features. As mentioned earlier, such flares repeated on an approximately 34.4-day period [Szymczak et al., 2016]. For methanol

the model parameters are $\langle T_{\rm R}\rangle_{\rm CH_3OH} = 2.1\,{\rm hr}$, $\sigma_{\rm T_R,CH_3OH} = 0.07\,\langle T_{\rm R}\rangle_{\rm CH_3OH}$ and $T'_{\rm CH_3OH} = 90\,\langle T_{\rm R}\rangle_{\rm CH_3OH}$, yielding a mean inverted column density of $\langle nL\rangle_{\rm CH_3OH} \approx 3.5\times10^4\,{\rm cm^{-2}}$, while for water we have $\langle T_{\rm R}\rangle_{\rm H_2O} = 7.7\,{\rm hr}$, $\sigma_{\rm T_R,H_2O} = 0.04\,\langle T_{\rm R}\rangle_{\rm H_2O}$, $T'_{\rm H_2O} = 70\,\langle T_{\rm R}\rangle_{\rm H_2O}$, and $\langle nL\rangle_{\rm H_2O} \approx 8.4\times10^4\,{\rm cm^{-2}}$. In both cases, the models were scaled in intensity to the data. As seen in the figure the methanol superradiance curve provides a very good fit to the corresponding data, especially in the wings, while although there is a fair amount of scatter in the data, the water superradiance intensity curve captures well the overall behavior of the water flare. It is important to note that, *despite the apparent time ordering in the emergence of the methanol and water flares, both superradiance models were initiated at the same time*, on Day 7261.5. The alternation between the methanol and water bursts observed in Figure 3 of Szymczak et al. [2016] is thus readily, and simply, explained by the fact that $\langle T_{\rm R}\rangle_{\rm H_2O} \approx 3.7\,\langle T_{\rm R}\rangle_{\rm CH_3OH}$, which delays the appearance of the water flare (from Eq. [4.2]) and broadens it relative to methanol. The two inverted-population column densities have comparable mean values (i.e., $\langle nL\rangle_{\rm H_2O} \approx 2.4\,\langle nL\rangle_{\rm CH_3OH}$) and correspond to large-samples lengths of $\langle L\rangle_{\rm CH_3OH} \approx 3.5\times10^5\,{\rm cm}$ and $\langle L\rangle_{\rm H_2O} \approx 8.4\times10^4\,{\rm cm}$ when $\langle n\rangle_{\rm CH_3OH} = 0.1\,{\rm cm^{-3}}$ and $\langle n\rangle_{\rm H_2O} = 1\,{\rm cm^{-3}}$. These length scales are, as was the case for the earlier examples, markedly smaller than those typical of masers, implying the presence of large number of superradiance samples.

Finally, it remains to be explained how the longer water intensity flares stay synchronized to the overall 34.4-day period between successive events, as shown in Figure 3 of Szymczak et al. [2016]. That is, the methanol bursts are short and end well before the appearance of the subsequent flaring event, but our water superradiance model in Figure 4.3 seems to indicate that the tail of the corresponding curve extends beyond the start of the next eruption cycle. The observed synchronization probably results from the fact that the arrival of the new pumping event responsible for the next flares resets the large-samples by re-establishing the inverted populations, which in effect terminates the water superradiance cascade and associated flare (i.e., truncates our superradiance model curve). The associated intensity then tends to zero but superradiance is once more triggered, resulting in the appearance of the next burst in intensity. This regenerative pumping phenomenon has previously been observed in laboratory superradiance experiments [Gross et al., 1976, Paradis et al., 2008].

4.4 Conclusion

We applied Dicke's theory of superradiance introduced in 1954 to the methanol 6.7 GHz and water 22 GHz spectral lines, often detected in molecular clouds as signposts for the early stages of the star formation process. Superradiance is characterized by burst-like features taking place over a wide range of time-scales, and provides a viable explanation for flaring observations of the 6.7-GHz methanol and 22-GHz water masers detected, respectively, in the G33.64-0.21 and Cep A star-forming regions. Furthermore, our superradiance model also provides a natural explanation for the recent observations of periodic and seemingly "alternating" methanol and water maser flares in G107.298+5.639. We showed how these flares are the result of simultaneously initiated 6.7-GHz methanol and 22-GHz water superradiant bursts operating on different time-scales, providing a natural mechanism for their observed durations and time-ordering.

When combined with the recent evidence reported in the environments of evolved stars [Rajabi and Houde, 2016b], the discovery of superradiance in star-forming regions broadens the applicability of our model and further establishes the existence of a previously unsuspected physical phenomenon in the ISM. The occurrence of superradiance in astrophysical objects implies the presence of entangled quantum mechanical systems, involving a very large number of molecules, over distances up to a few kilometers in the ISM, which can also be of interest to quantum information research.

Bibliography

M. G. Benedict, A. M. Ermolaev, V. A. Malyshev, I. V. Sokolov, and E. D. Trifonov. *Superradiance Multiatomic Coherent Emission*. Bristol: IOP Publishing Ltd, 1996.

D. M. Cragg, A. M. Sobolev, and P. D. Godfrey. Models of class II methanol masers based on improved molecular data. *Monthly Notices of the Royal Astronomical Society*, 360: 533–545, June 2005.

D. Crampton and W. A. Fisher. Spectroscopic observations of stars in H II regions. *Publications of the Dominion Astrophysical Observatory Victoria*, 14:283–304, 1974.

R. H. Dicke. Coherence in Spontaneous Radiation Processes. *Physical Review*, 93:99–110, January 1954.

R. H. Dicke. The Coherence Brightened Laser. In I. Agarbiceanu, A. Agafitei, L. Blanaru, N. Ionescu-Pallas, I. M. Popescu, V. Vasiliu, and V. G. Velculescu, editors, *Quantum Electronics*, page 35, 1964.

M. Elitzur. *Astronomical masers*, volume 170 of *Astrophysics and Space Science Library*. Dordrecht: Kluwer, 1992.

M. Elitzur, D. J. Hollenbach, and C. F. McKee. H2O masers in star-forming regions. *The Astrophysical Journal*, 346:983–990, November 1989.

K. Fujisawa, K. Sugiyama, N. Aoki, T. Hirota, N. Mochizuki, A. Doi, M. Honma, H. Kobayashi, N. Kawaguchi, H. Ogawa, T. Omodaka, and Y. Yonekura. Bursting Activity in a High-Mass Star-Forming Region G33.64-0.21 Observed with the 6.7GHz Methanol Maser. *Publications of the Astronomical Society of Japan*, 64, February 2012.

K. Fujisawa, G. Takase, S. Kimura, N. Aoki, Y. Nagadomi, T. Shimomura, K. Sugiyama, K. Motogi, K. Niinuma, T. Hirota, and Y. Yonekura. Periodic flare of the 6.7-GHz methanol maser in IRAS 22198+6336. *Publications of the Astronomical Society of Japan*, 66:78, July 2014.

G. Garay, J. M. Moran, and A. D. Haschick. The Orion-KL super water maser. *The Astrophysical Journal*, 338:244–261, March 1989.

S. Goedhart, M. J. Gaylard, and D. J. van der Walt. Periodic flares in the methanol maser source G9.62+0.20E. *Monthly Notices of the Royal Astronomical Society*, 339:L33–L36, March 2003.

M. Gray. *Maser Sources in Astrophysics*. New York: Cambridge Univ. Press, 2012.

M. Gross and S. Haroche. Superradiance: An essay on the theory of collective spontaneous emission. *Physics Reports*, 93:301–396, December 1982.

M. Gross, C. Fabre, P. Pillet, and S. Haroche. Observation of Near-Infrared Dicke Superradiance on Cascading Transitions in Atomic Sodium. *Physical Review Letters*, 36:1035–1038, April 1976.

T. Hirota, K. Ando, T. Bushimata, Y. K. Choi, M. Honma, H. Imai, K. Iwadate, T. Jike, S. Kameno, O. Kameya, R. Kamohara, Y. Kan-Ya, N. Kawaguchi, M. Kijima, M. K. Kim, H. Kobayashi, S. Kuji, T. Kurayama, S. Manabe, M. Matsui, N. Matsumoto, T. Miyaji, A. Miyazaki, T. Nagayama, A. Nakagawa, D. Namikawa, D. Nyu, C. S. Oh, T. Omodaka, T. Oyama, S. Sakai, T. Sasao, K. Sato, M. Sato, K. M. Shibata, Y. Tamura, K. Ueda, and K. Yamashita. Astrometry of H_2O Masers in Nearby Star-Forming Regions with VERA III. IRAS 22198+6336 in Lynds1204G. *Publications of the Astronomical Society of Japan*, 60:961–974, October 2008.

P. R. Jewell, J. C. Webber, and L. E. Snyder. Evolution of the OH maser emission from U Orionis. *The Astrophysical Journal*, 249:118–123, October 1981.

K. Mattila, N. Holsti, M. Toriseva, R. Anttila, and L. Malkamaki. Rapid outbursts in the water maser Cepheus A. *Astronomy & Astrophysics*, 145:192–200, April 1985.

L. I. Matveenko, D. A. Graham, and P. J. Diamond. The H2O Maser Flare Region in the Orion-Kleinmann / Orion-Kl / Nebula. *Soviet Astronomy Letters*, 14:468, December 1988.

J. Muzerolle, E. Furlan, K. Flaherty, Z. Balog, and R. Gutermuth. Pulsed accretion in a variable protostar. *Nature*, 493:378–380, January 2013.

T. Omodaka, T. Maeda, M. Miyoshi, A. Okudaira, M. Nishio, T. Miyaji, N. Motiduki, M. Morimoto, H. Kobayashi, and T. Sasao. The Enormous Outburst of the 7.9 km s^{-1} Water-Maser Feature in Orion KL. *Publications of the Astronomical Society of Japan*, 51: 333–336, June 1999.

E. Paradis, B. Barrett, A. Kumarakrishnan, R. Zhang, and G. Raithel. Observation of superfluorescent emissions from laser-cooled atoms. *Physical Review A*, 77(4):043419, April 2008.

S. Y. Parfenov and A. M. Sobolev. On the Class II methanol maser periodic variability due to the rotating spiral shocks in the gaps of discs around young binary stars. *Monthly Notices of the Royal Astronomical Society*, 444:620–628, October 2014.

Fereshteh Rajabi and Martin Houde. Dickes superradiance in astrophysics.I. the 21 cm Line. *The Astrophysical Journal*, 826(2):216, 2016a.

Fereshteh Rajabi and Martin Houde. Dickes superradiance in astrophysics. II. the OH 1612 MHz line. *The Astrophysical Journal*, 828(1):57, 2016b.

N. Skribanowitz, I. P. Herman, J. C. MacGillivray, and M. S. Feld. Observation of Dicke Superradiance in Optically Pumped HF Gas. *Physical Review Letters*, 30:309–312, February 1973.

M. Szymczak, P. Wolak, and A. Bartkiewicz. Discovery of four periodic methanol masers and updated light curve for a further one. *Monthly Notices of the Royal Astronomical Society*, 448:2284–2293, April 2015.

M. Szymczak, M. Olech, P. Wolak, A. Bartkiewicz, and M. Gawroński. Discovery of periodic and alternating flares of the methanol and water masers in G107.298+5.639. *Monthly Notices of the Royal Astronomical Society*, 459:L56–L60, June 2016.

D. J. van der Walt, S. Goedhart, and M. J. Gaylard. Periodic class II methanol masers in G9.62+0.20E. *Monthly Notices of the Royal Astronomical Society*, 398:961–970, September 2009.

H. Weaver, D. R. W. Williams, N. H. Dieter, and W. T. Lum. Observations of a Strong Unidentified Microwave Line and of Emission from the OH Molecule. *Nature*, 208:29–31, October 1965.

P. Wolak, M. Szymczak, A. Bartkiewicz, and E. Gerard. Violent maser events in the cirumstellar envelope of the pre-planetary nebula IRAS18276-1431. In *Proceedings of the 12th European VLBI Network Symposium and Users Meeting (EVN 2014). 7-10 October 2014. Cagliari, Italy*, page 116, 2014.

Conclusion and Future Plans

In this thesis the general assumption of independently interacting ensembles of atoms/molecules with the radiation field in the ISM was revisited. It was shown that coherent interactions between matter and the radiation field, i.e., superradiance, can take place in regions where the necessary conditions are met. These requirements were summarized as close atomic/molecular spacing, strong velocity coherence, population inversion, and long dephasing time-scales compared to those related to coherent behavior. We found superradiance to be characterized by strong intensity variability over periods ranging from hours to years.

The potential for superradiance was specifically investigated for neutral hydrogen clouds and the 21 cm line (Chapter 2), circumstellar envelopes and the 1612 MHz OH line (Chapter 3), and finally methanol and water samples in star-forming regions for, respectively, the 6.7 GHz and 22 GHz lines (Chapter 4). In Chapter 2, through our analysis of the 21 cm line the formalism of superradiance was extended to magnetic dipole interactions while also considering circularly polarized radiation. The results of our analysis suggested that, in principle, only relatively low levels of population inversion over short astronomical length-scales (e.g., 10^{14} cm in length) are needed for the realization of 21 cm superradiance in the ISM.

In Chapter 3 we took advantage of the detection of 1612 MHz OH masers in the CSE of evolved stars, confirming the existence of population inversions and strong velocity coherence for this line in these sources, to further investigate whether superradiance can also take place

in masing regions. Our analysis indicated that superradiance provides a valid explanation for previous observations of long lasting (i.e., several years) intensity flares detected in the 1612 MHz line for the U Orionis Mira star and the IRAS18276-1431 pre-planetary nebula.

In Chapter 4 we showed that our superradiance model explains flaring observations of the 6.7-GHz methanol and 22-GHz water masers detected, respectively, in the G33.64-0.21 and Cep A star-forming regions. Furthermore, we used superradiance to understand the recent observations of periodic and seemingly "alternating" methanol and water maser flares in G107.298+5.639. It was shown that these flares are the result of simultaneously initiated 6.7-GHz methanol and 22-GHz water superradiant bursts operating on different time-scales. These observations cannot otherwise be understood within the context of the maser theory.

The confirmation of superradiance in the environments of evolved stars in Chapter 3 and star-forming regions in Chapter 4 reveal new insight into physical conditions in the ISM. These discoveries further indicate the existence of entangled quantum mechanical states, consisting of a very large number of molecules, over distances up to a few kilometers in the ISM.

Since superradiance provides a natural mechanism for bursts lasting over a variety of time-scales, which could be as short as a fraction of a second, applying the concept of superradiance to Fast Radio Bursts (FRBs) might provide new insights for this phenomenon as well. FRBs are energetic eruptions at radio wavelengths with durations on the order of milliseconds. Such signals are occasionally detected while their origin still remains unexplained.

The superradiance model we have described in this thesis successfully explains the general behaviour of the types of systems we examined; however, a more advance model including effects such as pumping, diffraction losses, and different dephasing and relaxation time-scales is of interest to allow a more detailed understanding of the phenomenon. Such models can be, for example, used to characterize the shapes of superradiant spectral lines and their polarization properties.

VITA

Fereshteh Rajabi

Department of Physics & Astronomy, University of Western Ontario

London, Ontario, Canada, N6A 5B7

Education

2004-2008	University of Tehran, Tehran, Tehran, Iran, Atomic Physics, B.Sc.
2009-2010	Wesleyan University, Middletown, CT, USA, Atomic Physics, M.A.
2011-2012	University of Western Ontario, London, Ontario, Canada, Astronomy, M.Sc.
2012-2016	University of Western Ontario, London, Ontario, Canada, Physics, Ph.D.